

NEW DEVELOPMENTS IN SOLAR ENERGY CONVERSION:
FROM FUNDAMENTAL TWO-DIMENSIONAL MATERIALS TO
ADVANCED CONCENTRATING PHOTOVOLTAIC MODULES

A DISSERTATION

SUBMITTED ON THE FOURTH DAY OF DECEMBER 2020

TO THE DEPARTMENT OF PHYSICS

IN PARTIAL FULFILLMENT OF THE REQUIREMENTS

OF THE SCHOOL OF SCIENCE AND ENGINEERING

OF TULANE UNIVERSITY

FOR THE DEGREE

OF

DOCTOR OF PHILOSOPHY

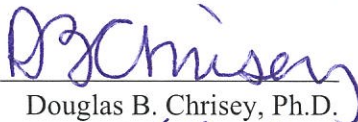
BY

Kazi M. Islam

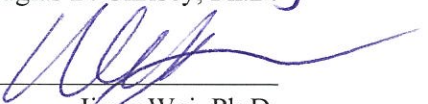
APPROVED:



Matthew D. Escarra, Ph.D.
Director



Douglas B. Chrisey, Ph.D.



Jiang Wei, Ph.D.



Jianwei Sun, Ph.D.

© Copyright by Kazi Mohitul Islam, 2020

All Rights Reserved

NEW DEVELOPMENTS IN SOLAR ENERGY CONVERSION:
FROM FUNDAMENTAL TWO-DIMENSIONAL MATERIALS TO
ADVANCED CONCENTRATING PHOTOVOLTAIC MODULES

AN ABSTRACT

SUBMITTED ON THE FOURTH DAY OF DECEMBER 2020

TO THE DEPARTMENT OF PHYSICS

IN PARTIAL FULFILLMENT OF THE REQUIREMENTS

OF THE SCHOOL OF SCIENCE AND ENGINEERING

OF TULANE UNIVERSITY

FOR THE DEGREE

OF

DOCTOR OF PHILOSOPHY

BY

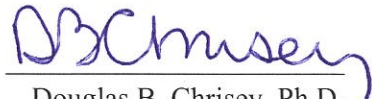
Kazi M. Islam

APPROVED:



Matthew D. Escarra, Ph.D.

Director



Douglas B. Chrisey, Ph.D.



Jiang Wei, Ph.D.



Jianwei Sun, Ph.D.

ABSTRACT

The importance of renewable energy technologies is more critical than ever now in 2020. Among the different types of renewable energy sources, solar energy is especially promising because of its abundance. This Ph.D. dissertation focuses on harnessing solar energy on two different scales. At the atomic scale, nanometer-thick two-dimensional (2D) transition metal dichalcogenides (TMDCs) are used for making ultra-thin photovoltaic (PV) cells along with other optoelectronic devices such as transistors and photodetectors. The optical properties of these nanomaterials are investigated via spectroscopic ellipsometry, showing birefringence and other new features. Schottky-junction photovoltaic devices are designed, fabricated, and characterized with 2D MoS₂ and carrier-selective asymmetric contacts such as Ti and Pt for electron and hole collection, respectively. 2D TMDCs have direct bandgaps compared to their bulk counterparts, enabling strong light-matter interactions in these materials. Because of their atomically-thin nature and excellent optoelectronic properties, these materials are good candidates for solar cells with record-high specific power density, i.e., power/mass (W/kg) and power/volume (W/m³). Going from the nanoscale to the micron- and centimeter-scale, transmissive microfluidic channels are developed for actively cooling concentrating photovoltaics (CPV) in a hybrid energy conversion system. The hybrid solar receiver consists of an optically transmissive CPV module on the front and a thermal receiver at the

back, coupled together by the transmissive microfluidic CPV active cooling. While the CPV module absorbs the high energy photons and converts them directly into electricity, the thermal receiver receives the low energy photons and converts them into high-temperature process heat. The transmissive cooling channels ensure that the unabsorbed photons in the CPV module can make their way to the thermal receiver while preventing the solar cells from overheating. On top of that, the heat energy absorbed by the cooling water in the microchannels can be extracted and used as low-temperature process heat, thus providing a third energy stream. With these two unique approaches, this dissertation aims to contribute to the ever-expanding field of solar energy conversion and point towards a greener future.

ACKNOWLEDGMENT

I dedicate this dissertation to my family- my son, Abram, who was born at the beginning of my PhD and has been through it all with me; my wife, who went through so much in supporting me day in and day out that she could have got her own PhD and some more during this time; my parents who had been there since day one and did everything in their capacity and never asked for anything in return except for my success; and my younger brother who held it all together back home while I am living ~10000 miles away.

I want to thank my advisor, Prof. Matthew Escarra, for his guidance and supervision. I have learned a lot from him, but I want to mention two things in particular. Matt taught me how to raise the bar for anything and everything and always keep pushing for that last inch. Matt also implanted the rainbow plots in me, and now I can't get rid of them! Thank you, Matt.

I want to thank my research supervisory committee members, Prof. Doug Chrisey, Prof. Jiang Wei, and Prof. Jianwei Sun, for their mentorship and invaluable advice throughout my graduate studies. Thank you all for your valuable time.

I also want to thank my friends, labmates, and colleagues— too many names to name, but y'all know who you are, and I can't thank you enough for being there for me.

TABLE OF CONTENTS

Acknowledgment	ii
List of Figures	vii
List of Tables	xiii
1 Introduction.....	1
1.1 2D Materials.....	2
1.1.1 Transition Metal Dichalcogenides	3
1.2 Hybrid Solar Converter	6
1.2.1 Transmissive Active Cooling for CPV	9
1.3 Thesis Overview.....	11
2 Synthesis & Optical Properties of 2D MoS ₂	14
2.1 MoS ₂ Synthesis	17
2.2 Physical Properties of MoS ₂	19

2.3	Ellipsometric Characterization of MoS ₂	21
2.3.1	Analysis of Thin-Film MoS ₂	25
2.3.2	Analysis of Few-Layer MoS ₂	27
2.3.3	Analysis of Monolayer MoS ₂	28
2.4	UV-Vis-NIR Spectroscopy	29
2.5	Optical Modeling.....	30
2.6	Conclusions and Future Work.....	38
3	Optoelectronic Applications of 2D MoS ₂	42
3.1	Transistors	43
3.2	Photodetectors	45
3.3	Optoelectronic Device Performance	47
3.4	Chemical Treatments for Enhanced Performance.....	52
3.5	Conclusions and Future Work.....	56
4	Large-Area, Monolayer MoS ₂ -based Schottky-junction Photovoltaics.....	60
4.1	Device Structure and Fabrication.....	61
4.2	Photovoltaic Performance	66

4.3	Optoelectronic Device Model	73
4.4	Conclusion.....	77
4.5	Future Work	77
5	Transmissive Active Cooling in a Hybrid Solar Converter	80
5.1	System Overview	82
5.2	Modeling	84
5.2.1	Optical Model	84
5.2.2	Thermal Model.....	87
5.2.3	Microfluidic Model.....	92
5.2.4	Analytical Model for Flowrate vs. Pressure drop	94
5.3	Fabrication of Microchannels.....	96
5.4	Results and Discussion.....	100
5.4.1	Flow Characteristics.....	101
5.4.2	Optical Transmission	103
5.4.3	CPV Cooling Performance	107
5.5	Conclusions and Future Work.....	110

6	Conclusion	112
6.1	2D Materials-based Optoelectronic Devices.....	112
6.2	2D Materials Outlook.....	115
6.3	Transmissive Active Cooling in a Hybrid Solar Converter	116
6.4	Transmissive Microchannels Outlook.....	117
6.5	Final Thoughts.....	118
	Appendix A: Optoelectronic Device Fabrication	119
	Appendix B: Publications, Patents, and Presentations Related to this Thesis	133
	Bibliography	136

LIST OF FIGURES

- Figure 1.1 Crystal structure of 2D MoS₂ showing strong in-plane covalent bonding and weak out-of-plane van der Waals bonding. The brown circles represent Mo atoms, while the yellow circles represent the S atoms. 4
- Figure 1.2 The ASTGM173-03 reference spectra derived from SMARTS v.2.9.2. The infrared transparent CPV module acts as a spectrum splitter dividing solar radiation into two parts. Here, we refer to them as in-band light and out-of-band light. In-band is absorbed in the CPV cell and most efficiently converted to electrical energy and out-of-band is transmitted through the cell efficiently converted to thermal energy. 8
- Figure 1.3 Spectrum division and energy flows in the hybrid transmissive CPV/T receiver. Electricity converted from UV/visible light flows from CPV cells, while IR light transmits through to a conical cavity thermal receiver. 9
- Figure 2.1 Schematic of the two synthesis methods used in this study: chemical vapor deposition (CVD) and thermal vapor transport (TVS). A standard two-zone furnace is modified to have a third zone for low-temperature sulfur (S) evaporation and to increase the distance between the S source and the growth substrate. 19
- Figure 2.2 (a) Raman characterization of the CVD and TVS grown MoS₂ samples on SiO₂-on-Si substrates using a 532 nm laser source. (b) Photoluminescence (PL) spectra of a monolayer MoS₂- sample with an emission peak near 670 nm, using a 405 nm excitation source. AFM images showing step height and topography of the (a) monolayer, (b) few-layer, and (c) thin-film MoS₂ samples. 20
- Figure 2.3 Transmission spectra of monolayer MoS₂ as-grown on sapphire measured at five different locations (four corners and center of a 1cm x 1cm sample) showing uniform optical properties across a cm-scale sample. 21
- Figure 2.4 (a) Schematic of the spectroscopic ellipsometry measurements showing the optical model of the MoS₂-SiO₂-Si samples. Measured and modeled (b) Ψ and (c) Δ spectra of monolayer MoS₂ versus wavelength. The solid colored lines are measured data at various angles of incidence, and the dashed black lines are modeled fit values with good agreement obtained over the full spectral range. 22
- Figure 2.5 Optical constants n & k for thin-film MoS₂ analyzed using a birefringent model. The in-plane index was fitted using B-Spline model (solid lines) or a combination of

Gaussian and Sellmeier functions (dotted lines) with nearly identical results. The out-of-plane component was fit to a single Sellmeier function and plotted above to 1.3 eV. 27

Figure 2.6 In-plane optical constants, n and k , for monolayer, few-layer, and thin-film MoS₂. The refractive index, n , is shown at the top, while the extinction coefficient, k , is shown at the bottom. 29

Figure 2.7 (a) Measured transmittance of monolayer, few-layer, and thin-film MoS₂ samples grown directly on sapphire. Modeled transmittance of (b) monolayer, (c) few-layer, and (d) thin-film MoS₂ samples overlaid with experimentally measured transmittance. The models use the complex refractive index data measured by spectroscopic ellipsometry. 32

Figure 2.8 (a) Modeled absorption of monolayer, few-layer, and thin-film MoS₂ using the complex refractive index measured by spectroscopic ellipsometry as shown in Figure 2.6. (b) Absorption per unit thickness is plotted vs. wavelength. 34

Figure 2.9 Calculated absorption (%) in (a) monolayer and (b) few-layer MoS₂ vs. wavelength for a range of TiO₂ thickness on top. The optical stacks here are modeled as air-TiO₂-MoS₂-air and only the absorption (%) in the active MoS₂ layers is plotted. (c) Calculated absorption (%) in thin-film MoS₂ for a range of ITO thickness as an ARC. (d) Various ARCs are studied to enhance the broadband absorption in thin-film MoS₂. 36

Figure 2.10 Modeled absorption (%) and J_{sc} of a thin-film MoS₂ photovoltaic device with 100% IQE. (a) Absorption (%) in 250 nm thin-film MoS₂ with and without 60 nm ITO on top as an ARC; (b) J_{sc} vs. thin-film MoS₂ thickness (5 nm - 500 nm) with and without 60 nm ITO. 37

Figure 3.1 Schematic of a back-gated field-effect transistor (FET) with 2D MoS₂. The back-gate is scratched through the 300 nm SiO₂ layer and uses the highly-doped n-type silicon substrate underneath. (figure not to scale) 44

Figure 3.2 Schematic of a transistor-type photodetector with 2D MoS₂. A transistor shown in Figure 3.1 can be used as a photodetector if the carrier transport in the channel is modulated by light instead of a gate-bias. (figure not to scale) 45

Figure 3.3 Optical micrograph of an array of devices with variable channel length and 100 μ m channel width. 5 nm Ti capped with 45 nm Au is used as contacts on monolayer MoS₂ for transistor and photodetector applications. Gate contact is not shown in the image. 48

Figure 3.4 Output characteristics of a MoS₂-based FET. The source-drain voltage is swept between -5 V to 5 V for five gate biases, $V_G = -20$ V, -10 V, 0 V, 10 V, and 20 V. The red and yellow lines overlap each other. 49

Figure 3.5 Transfer characteristics of a MoS₂-based FET. I_{DS} is plotted in linear (left) and logarithmic (right) scales. V_G is swept from -80V to 80V under $V_{ds} = 2, 4, 6, \text{ and } 8$ V. . 50

Figure 3.6 Wavelength dependent photocurrent for a monolayer MoS₂-based transistor-type photodetector. Measurements are taken between 400 and 800 nm monochromatic illumination for three different source-drain voltages, V_{DS}= 0 V, 1 V, and 5 V. 51

Figure 3.7 External Quantum Efficiency (EQE) of a monolayer MoS₂-based transistor-type photodetector. The measurements were performed between 400 and 800 nm with a source-drain bias of 5V..... 52

Figure 3.8 Photocurrent of a photodetector before and after DCE treatment. The photocurrents were measured at regular time intervals post DCE treatment to study the time-dependent decay. Measurements were performed under 5V source-drain bias. 53

Figure 3.9 Enhancement in photocurrent followed by DCE treatment. The enhancement factor is calculated by dividing the post-treatment photocurrents by the pre-treatment reference photocurrent at each wavelength..... 54

Figure 3.10 Spectral photocurrent measured at regular time intervals post-DCE treatment at monochromatic wavelengths of 420, 620, and 660 nm; these wavelengths roughly correspond to the excitonic A, B, and C peaks of monolayer MoS₂. All measurements were performed under a 5V source-drain bias..... 55

Figure 4.1 Schematic of a Schottky-junction photovoltaic device with asymmetric contacts on 2D MoS₂. Note the difference in color for source and drain, indicating metals of different work functions..... 62

Figure 4.2 An all-in-one optoelectronic device architecture. By contacting the left two symmetric contact pads, the device can be operated as a transistor (with an external gate contact) or photodetector; the right two asymmetric contact pads can be probed to use this as a photovoltaic device. 63

Figure 4.3 Band structure schematic for monolayer MoS₂, showing metal work function requirements for carrier (electron and hole) separation. Possible low and high work function metals are listed on the right and left, respectively. 64

Figure 4.4 fabricated asymmetric contact Schottky-junction solar cells with Ti and Pt contacts. The top row shows the all-in-one symmetric and anti-symmetric device architecture, while the bottom row shows more traditional finger-busbar type solar cells. 65

Figure 4.5 An illuminated asymmetric contact Schottky-junction solar cell with 2D MoS₂. The laser excitation wavelength is 660 nm..... 66

Figure 4.6 J-V plot of a Schottky-junction MoS₂ solar cell with 660 nm laser excitation, as shown in Figure 4.5. The laser flux was varied with a maximum of 15.97 15.97 W/cm² flux. 67

Figure 4.7 J-V plot of a finger-busbar type Schottky-junction MoS ₂ solar cell with monochromatic 660 nm laser excitation and 1-sun equivalent AM1.5G illumination.....	68
Figure 4.8 Absorption, EQE, and IQE of the finger-busbar type Schottky-junction MoS ₂ -based solar cell.....	69
Figure 4.9 A TLM grid pattern on monolayer MoS ₂ with variable channel lengths from 1 μm to 150 μm. These structures are used to extract the contact resistivity at the metal-semiconductor interface and the sheet resistivity of the semiconducting material.....	70
Figure 4.10 TLM plots for Ti-MoS ₂ and Pt-MoS ₂ devices. The resistances are plotted for various channel lengths. Contact resistance is extracted from the y-axis intercept of the linear fit (divided by 2) and the sheet resistance is calculated by taking the slope of the linear fit line and dividing it by the channel width.	71
Figure 4.11 Spatial photocurrent map of a Schottky-junction MoS ₂ -based solar cell, showing photogeneration and collection mostly near the Pt contacts.	72
Figure 4.12 Schematic of a MoS ₂ -based solar cell with 10 μm channel in between asymmetric Ti and Pt contacts, generated in the COMSOL Multiphysics software.	73
Figure 4.13 Band structure of a Ti-MoS ₂ -Pt Schottky-junction solar cell showing the asymmetric band bending at the metal-semiconductor interfaces. The larger bend on the right side between MoS ₂ and Pt indicates a large Schottky barrier.	75
Figure 4.14 Simulated I-V curve of a monolayer MoS ₂ -based solar cell with asymmetric Ti-Pt contacts under AM1.5G solar irradiance.	76
Figure 5.1 CAD drawing of the transmissive CPV module; the transmissive active cooling microchannels are highlighted.	82
Figure 5.2 Cross-sectional schematic of the CPV module (layers not to scale).....	84
Figure 5.3 Energy weighted module transmission for different microchannels thickness assuming water as the coolant fluid.....	85
Figure 5.4 Effect of PDMS base layer thickness on the solar-spectrum-energy-weighted transmission of the CPV module.	86
Figure 5.5 Schematic of thermal model geometry with primary heat flow path illustrated.	88
Figure 5.6 Schematic of the equivalent thermal resistance network.	88
Figure 5.7 Temperature map of CPV module with (left) active microfluidic cooling and (right) passive cooling from top window convection only. The non-uniformity in the cell	

temperatures is a result of non-uniform flux pattern which was obtained from the concentrating mirror at the outdoor test site. Maps share same color palette.....	91
Figure 5.8 A rectangular microchannel to demonstrate the hydraulic diameter.....	92
Figure 5.9 Plot of maximum cell temperature and pressure drop across the microchannels as a function of channel depth, with 550 suns irradiance.	94
Figure 5.10 Modeled and experimental pressure drop vs. flowrate in the microchannels. Red line represents a linear fit to the experimental data.	95
Figure 5.11 Complete process flow of the microchannels fabrication process.	96
Figure 5.12 Optical profilometer showing step height of the stamp (left) and the microchannels (right).	98
Figure 5.13 Contact angle measurement on glass, aluminum and silicon substrates with a droplet of water, with OTS and Fluoroform release layers and no release layer as reference.	99
Figure 5.14 Photograph of the stamp (top) and the fabricated channels on the channel plate (bottom).....	100
Figure 5.15 Fluid flow loop showing the test setup. The accumulator expansion tank was pre-charged to 40 psi on the air bladder side.	101
Figure 5.16 Photograph showing different components of the fluid-flow test setup.....	102
Figure 5.17 Pressure drop vs. flowrate in the microchannels. The red line shows a fit to the expected Darcy-Weisbach linear relationship for laminar flow.	103
Figure 5.18 Transmission measurements and models for the optical stack without microchannels (a) cell region and (b) bypass region. (c) Transmission measurement and model for the microchannels only. (d) Energy weighted transmission at the three different regions of the CPV module with microchannels attached, i.e., cell region, bypass region with channels with 100 μm water, and bypass region without channels.....	104
Figure 5.19 (a) Map showing distribution of solar energy flux on the CPV module. Black dots represent three locations where thermocouples were placed to monitor real-time temperatures. The scale bar represents number of suns. (b) Measured DNI for the ~8-hour period of testing shown here, in San Diego, Ca. Only 35% of the mirror area was exposed during CPV operation (c) Typical cell temperature vs DNI plot demonstrating linear relation, plotted only for “on-sun” data. (d) Temperature measurements for the three thermocouple locations shown in (a), water inlet, and water outlet.	107

Figure 6.1 SEM image of anoantenna array patterned from monolayer MoS₂ by electron-beam lithography followed by MoS₂ etching. The exciting applications of such photonic structures are yet to be fully explored..... 118

LIST OF TABLES

Table 4.1 Figures-of-merit for the finger-busbar type asymmetric contact Schottky-junction MoS ₂ -based solar cell under 1-sun AM1.5G illumination	68
Table 5.1 Thermal properties of each component of the CPV ⁷⁸ . The top, bottom and lateral regions are shown in Figure 5.5.....	87
Table 5.2 Modeled and experimental energy-weighted transmission in all three regions of the CPV module, with corresponding power flow.....	106
Table 5.3 Modeled and measured maximum temperatures and thermal resistance for the average concentration and at three different thermocouple (TC) locations (as shown in Figure 5.19a) marked as TC1, TC2, and TC3.....	109

1 INTRODUCTION

Solar energy is the most abundant form of energy on Earth's surface, and it is up to us how we harness it in a way that can eventually lead us to a renewable energy-based future. The amount of energy that strikes the Earth from the sun in one hour is more than enough to meet the entire global demand for a year. Two of the central ways in which solar energy can be converted into usable energy are: first, converting the photons from sunlight into electricity directly and second, converting the solar energy into usable thermal energy. In this thesis, both approaches have been investigated, and as such, the dissertation is divided into two broad parts. First, we discuss the application of two-dimensional (2D) materials for photovoltaics (PV) and other optoelectronics devices. In the second part, we discuss developing a novel hybrid solar converter that converts sunlight into electricity and heat simultaneously using concentrator photovoltaic (CPV) cells and a thermal receiver. This thesis mainly focuses on the active cooling of the CPV cells that also acts as a coupling between the CPV cells and the thermal receiver and yields a separate energy stream into the mix.

1.1 2D Materials

In 1959, Feynman gave a talk titled ‘there’s plenty of room at the bottom,’ and such has never been truer than now. Since the discovery of extraordinary mechanical and electronic properties of graphene back in 2004 by Geim and Novoselov¹, a whole new branch of physics has emerged as ‘2D materials’, which is one of the most studied groups of materials at the moment. In essence, these materials are planar sheets of atoms with angstrom-scale thicknesses in the vertical direction. The layered nature of such materials is known for a while. For example, back in 1966, Frindt demonstrated molybdenum disulfide's (MoS_2) layered structure even though he suspected these materials might not be stable at their atomic thicknesses². It is not until 2004 that the interest in such layered materials was rejuvenated, and before long, there were families of materials that were added to the list of 2D materials that include metals, semi-metals, semiconductors, and insulators with a wide range of physical properties³. Here, we briefly discuss the 2D materials families and focus on a particular material of interest, MoS_2 , that belongs to a distinct family of 2D materials.

Graphene is layered carbon material with a honeycomb crystal structure. It has superior electronic and mechanical properties such as high carrier mobility and high electrical and thermal conductivity. However, because graphene is a semi-metal with no electronic bandgap, it cannot be effectively used for semiconductor device applications such as transistors, etc. without engineering its electronic band structure.

While research has been directed towards creating a bandgap in graphene through doping, functionalization, quantum confinement, etc., several other materials have also been discovered in their 2d form that show interesting properties, unlike their bulk counterparts.

Among these, the mostly semiconducting transition metal dichalcogenide (TMDC) family of 2D materials, including MoS₂, WS₂, MoSe₂, WSe₂, etc. and an insulator, hexagonal boron nitride (h-BN), have received the most interest. This thesis focuses on the semiconducting 2H-phase of 2D MoS₂ for its unique optoelectronic properties that will be discussed in detail in the following sections.

1.1.1 Transition Metal Dichalcogenides

Transition metal dichalcogenides (TMDCs) are a family of materials with a general chemical formula of 'MX₂', where 'M' is a transition metal, and 'X' is a chalcogenide element. These layered materials are composed of stacked sheets where each sheet is composed of three atoms- a metal atom sandwiched between two chalcogen atoms. Such sheets are commonly referred to as a monolayer. Within a monolayer, all intralayer metal-chalcogen bondings are predominantly covalent. In contrast, the interlayer bonds are usually weak van der Waals forces, facilitating easy layer separations. Figure 1.1 shows the crystal structure of 2D MoS₂. The chalcogen atoms do not have any dangling bonds, enabling chemical stability even in their monolayer form.

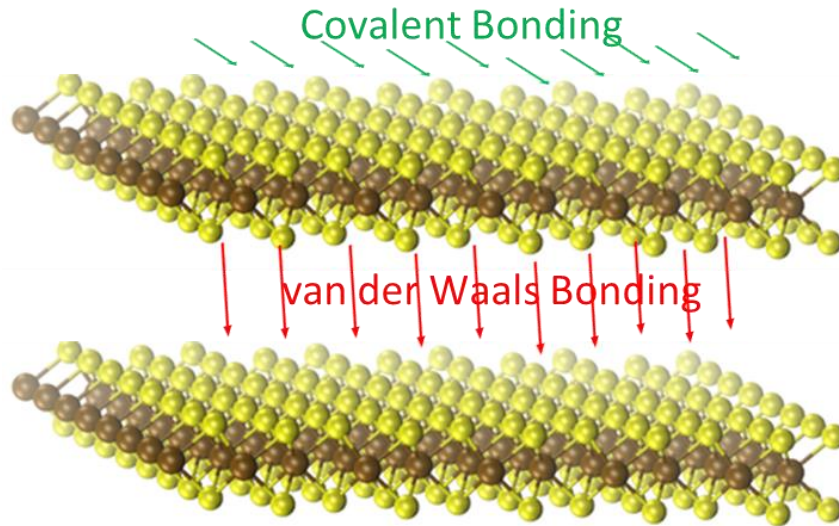


Figure 1.1 Crystal structure of 2D MoS₂ showing strong in-plane covalent bonding and weak out-of-plane van der Waals bonding. The brown circles represent Mo atoms, while the yellow circles represent the S atoms.

Most TMDCs are inherently semiconducting, i.e., they have an electronic bandgap that makes them suitable for electronic applications such as transistors, unlike graphene. Thus, since the experimental discovery of 2D MoS₂ back in 2010^{5,6}, six years after that of graphene, MoS₂ has become very popular in the 2D world along with some other TMDCs. The electronic bandgaps of TMDC materials range from 2.03 eV (WS₂) to 1.02 eV (MoTe₂), a wide spectral range that is very suitable for photovoltaic collection of the solar spectrum^{7,8}. As for MoS₂, in its bulk form it has an indirect bandgap of 1.3 eV, while in its monolayer form, it transitions to a direct bandgap of 1.85 eV, as shown by Splendiani et al.⁶. It is an atomically thin material- a single layer of MoS₂ is only 0.6 nm thick. It offers ultra-high absorption efficiency and efficient conversion of light to electricity and vice versa.

MoS₂ is a very promising candidate for future optoelectronics due to its strong light-matter interactions and stability at atomic thicknesses. In the 2D form, due to its direct bandgap and high absorption coefficient, it exhibits high quantum efficiency. It has been tested for several exciting applications, including transistors, photodetectors, photo-emitters, photovoltaics, etc⁹. Most of the work done with these materials comes from mechanical exfoliation from the bulk materials, which is excellent for proof-of-concept but severely limits scalability and is not viable for commercial applications. Thus it is essential to focus on large-area scalable synthesis of high-quality 2D MoS₂.

Exfoliated MoS₂ has been used to demonstrate many of the device applications with excellent performance. Radisavljevic et al.¹⁰ demonstrated a transistor using monolayer MoS₂ with mobility of 200 cm²V⁻¹s⁻¹ at room temperature and an on-off ratio of 10⁸. By encapsulating with h-BN and using graphene as contact¹¹, a MoS₂-based transistor was shown to achieve a Hall mobility of up to 34000 cm²V⁻¹s⁻¹. Also, a photodetector fabricated with MoS₂ showed a photoresponsivity of 880 A/W that is roughly two orders of magnitude higher than commercial Si-based photodiodes¹².

These excellent electronic transport and optical absorption properties are both of high value in a photovoltaic device design, and by the same virtues mentioned earlier, MoS₂ is also poised to be a great candidate for nanoscale photovoltaic devices. In fact, in 2013 Bernardi et al. determined that monolayer TMDC materials absorb 5-10% of the incident sunlight in a sub-nm thickness that is one order of magnitude higher absorption per unit thickness than GaAs and Si, the state-of-the-art materials used for photovoltaics¹³. They also showed that photovoltaic devices made with these TMDC materials could obtain a specific power density of 450 – 1800 kW/kg, two orders of magnitude higher than the 54 kW/kg of the

current best state-of-the-art GaAs-based photovoltaics. There have been several advances in the field since then, which will be discussed in detail later in chapter 4. This serves as a key motivation behind this dissertation: that nanometer-thin photovoltaic devices made with 2D materials such as MoS₂ could revolutionize the world of photovoltaics where ultra-high power density (kW/kg and/or kW/m³) is required, such as in space.

With that, we now move into introducing the next part of this dissertation- the hybrid solar energy converter.

1.2 Hybrid Solar Converter

Concentrator photovoltaic (CPV) solar energy conversion is a promising technology for cost-effective power generation by replacing high-cost photovoltaic (PV) cells with lower cost concentrating optics¹⁴. CPV systems generally utilize high-efficiency III-V photovoltaics that operate efficiently for ultraviolet (UV) and visible light but cannot absorb infrared (IR) light and therefore waste a large portion of spectral IR energy as heat¹⁵. This poor IR collection both inefficiently utilizes the entire solar spectrum and adversely affects CPV performance due to elevated cell temperatures. In contrast, concentrated solar power (CSP) systems use solar thermal energy to generate heat, which can be used as process heat, stored for later use, or passed through an engine to produce electricity^{16,17}. Hybrid concentrator photovoltaic/thermal (CPV/T) systems mitigate the PV thermal losses by collecting heat and turning it into a usable power stream, thereby more efficiently utilizing the entire solar spectrum¹⁸.

Let us take a step back and explain the photovoltaic operation to explain the motivation behind this approach better. A solar cell operates in two broad steps- first, photons from

the sunlight are absorbed in the active material and the absorbed light generates electron-hole pairs, and second, these electrons and holes are collected through contacts external to the device.

There are losses in each of these steps, but the first loss comes from the fact that the active material used to absorb light can only absorb photons with equal or higher energy than the bandgap of the material. In other words, any photon transmitting through the material that has lower energy than the bandgap of the active material is lost right away and dissipated as heat, which further deteriorates the photovoltaic power conversion efficiency. A hybrid system is designed to capture the lost photons and convert them into a usable energy form. As such, there have been efforts to develop a system that can better utilize the broad solar spectrum and increase overall system power conversion efficiency.

We developed a hybrid system that is comprised of a transmissive CPV module and a thermal receiver. The CPV module absorbs the high-energy photons converting them directly into electricity, and the low-energy photons are fed to the thermal receiver for process heat generation. Figure 1.2 shows the solar spectrum and how the solar energy is divided between the CPV module and the thermal receiver¹⁹.

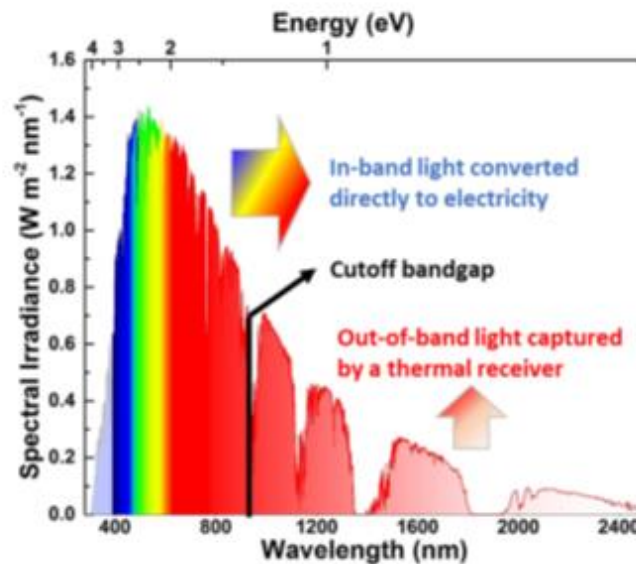


Figure 1.2 The ASTGM173-03 reference spectra derived from SMARTS v.2.9.2. The infrared transparent CPV module acts as a spectrum splitter dividing solar radiation into two parts. Here, we refer to them as in-band light and out-of-band light. In-band is absorbed in the CPV cell and most efficiently converted to electrical energy and out-of-band is transmitted through the cell efficiently converted to thermal energy.

Figure 1.3 shows a schematic of the system, broken down into subcomponents²⁰. The CPV cells are made with III-V semiconductors with GaAs bottom cells that only absorb up to 873 nm of the spectrum. The IR part of the spectrum is channeled to the thermal receiver through an optical coupling. At high solar concentration, the CPV cells heat up beyond their designed operating temperature, so it is imperative to cool them while still transferring the low-energy photons to the thermal receiver. This dissertation mainly focuses on the novel transmissive active cooling of the CPV cells in this hybrid solar collector.

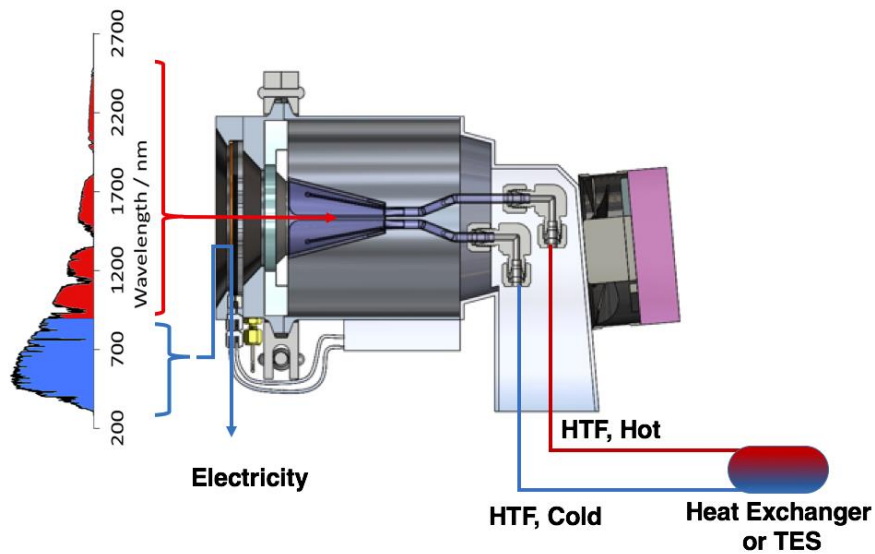


Figure 1.3 Spectrum division and energy flows in the hybrid transmissive CPV/T receiver. Electricity converted from UV/visible light flows from CPV cells, while IR light transmits through to a conical cavity thermal receiver.

1.2.1 Transmissive Active Cooling for CPV

The high concentration of sunlight in a CPV/T system typically results in very high cell temperature and requires some form of cooling. This increased temperature adversely affects the overall performance of the cells with regards to instantaneous output and operating lifetime. In the short-term, increased cell temperature decreases the cell efficiency and electrical output due to reduced open-circuit voltage (V_{oc}) caused by reduced bandgap energy²¹. Though the short circuit current density (J_{sc}) slightly increases as the temperature rises, the overall PV efficiency decreases²². Additionally, continual exposure to high temperatures significantly reduces the lifespan of PV systems^{23,24} from reverse saturation current in the cells²⁵. As such, higher temperatures and thermal gradients across

the cell area are major concerns in CPV systems and demand cooling systems for temperature control as shown by Shukla et al.²⁶ and Gilmore et al.²⁷.

For solar concentrations above 150 suns, the thermal resistance (R) of the cooling system needs to be lower than 10^{-4} K-m²/W, i.e., the convection coefficient (h_c) needs to be higher than 10^4 W/ K-m².²⁶ Both active and passive cooling have been investigated for CPV technology^{28,29}. Royne et al. did a comprehensive and critical review of CPV cooling, including models, parameters, and output characteristics of both passive and active cooling systems. Passive cooling works well at high concentration for point-focus concentrator based single cells but does not work effectively for a densely packed array of cells at high concentration³⁰.

Active cooling provides sufficient heat transfer coefficients to manage the large thermal load from a densely packed array. Microchannels and impinging jets-based active cooling are viable solutions at high concentrations as demonstrated by Di Capua H. et al.³¹. Microchannels are particularly suitable for integration in the CPV/T manufacturing process²⁸. However, conventional microfluidic cooling systems rely on metallic, opaque channels mounted to the cells' bottoms.

Gilmore et al. did an exhaustive review of existing microchannel-based active cooling systems, including single-layered, multi-layered, and jet-impingement designs²⁷. In particular, this review lists the state-of-the-art in microchannel cooling, showing that the dominant material used in single-phase microchannel fabrication is silicon, while copper is the material of choice in multi-phase microchannel cooling systems - both of which are opaque to the majority of solar illumination.

To enable active cooling of a transmissive CPV/T system, we present here the design, fabrication, characterization, and on-sun validation of 100 μm and 250 thick μm transmissive microchannels capable of maintaining the temperatures of a dense array of CPV cells below 110 $^{\circ}\text{C}$ for fluxes up to 300 suns.

1.3 Thesis Overview

Having introduced the two main concepts of this thesis, 2D materials and hybrid concentrator photovoltaics, we now provide an overview of the content of this thesis. This thesis can be divided into two main sections. Chapter 2-4 focuses on 2D materials- from synthesis to physical properties to various device applications. Chapter 5 discusses the hybrid concentrator photovoltaic module and system and focuses on the active cooling aspect in detail. Finally, Chapter 6 provides a comprehensive summary and future outlooks of this dissertation.

In chapter 2, we discuss in detail the synthesis of large-area 2D materials and their physical properties. We characterize the 2D MoS_2 films with various state-of-the-art tools such as AFM, Raman spectroscopy, UV-Vis-NIR spectroscopy, photoluminescence, etc. We focus on the optical properties of MoS_2 , measured via variable angle spectroscopic ellipsometry. Three different kinds of samples were studied- 2D monolayer MoS_2 , 2D few-layer MoS_2 , and thin-film MoS_2 . The complex refractive index of all three samples were measured and analyzed for both in-plane and out-of-plane optical properties. The work was done in collaboration with J. A. Woollam Inc.

In chapter 3, we describe optoelectronic device fabrication with large-area monolayer MoS₂. Nanofabrication processes are discussed with details of each step and two device applications are focused on this chapter- transistors and photodetectors. Transistors are important applications of 2D materials and here, we also extract carrier mobility of the underlying 2D MoS₂ from the gated transistor I-V sweeps. Mobility is an essential check of the material quality that governs its electronic transport. Transistor-type photodetectors are also demonstrated and characterized for their photoresponsivity. After discussing the results of as-fabricated device performance, we also present a simple chemical treatment method that improved the photocurrent by orders of magnitude.

After discussing the synthesis and some optoelectronic device applications of MoS₂ in chapter 2 and 3, we move on to the prized content of this thesis, 2D materials based photovoltaic devices, in chapter 4. Schottky-junction photovoltaics are fabricated with asymmetric contacts. Their fabrication process flow is described and device performances are discussed for 1-sun AM1.5G and monochromatic illumination. A thorough discussion is devoted to the relatively low J_{SC}, and ways to improve it are proposed. Lastly, an optoelectronic model of the 2D photovoltaic device is built using COMSOL multiphysics simulation tools to better understand the device performance and improve it further.

Chapter 5 will transition to hybrid concentrator photovoltaics- the system design, module fabrication and characterization, and finally focus on the active cooling aspect. Several models are discussed concerning each physical element of the hybrid system. As stated earlier, the microchannel based active cooling is the prime focus of this part of the thesis and as such, thermal and microfluidic models and indoor characterization will be

emphasized. Finally, outdoor on-sun test results at high solar concentration will be presented and discussed.

Finally, chapter 6 will summarize all the major findings of this thesis and draw conclusions from them. Particular focus will be given towards developing future optoelectronic devices based on 2D materials as well as the versatility of potential applications of microchannel-based active cooling.

2 SYNTHESIS & OPTICAL PROPERTIES OF 2D MoS₂

In this chapter, we first describe the chemical synthesis methods of MoS₂ and then present their physical properties, with a particular focus on their optical properties. Two different synthesis methods are utilized for growing monolayer vs. few-layer/thin-film MoS₂. Physical properties are first characterized by optical microscopy, SEM, AFM, etc. and then an extensive optical characterization is performed. Variable Angle Spectroscopic Ellipsometry (VASE) is used to measure the complex refractive index of three different thicknesses of MoS₂ films for a wide spectral range between 190 nm and 1700 nm. The measured data is then used to model transmission and absorption of such films to help design future optoelectronic devices based on these 2D materials.

Most studies on 2D materials have been done on exfoliated layers that are limited by lateral dimension and are not scalable. After the initial proof-of-concept stage, research is now moving towards synthesized 2D MoS₂ that is scalable, with precise thickness control and uniform coverage. The properties of 2D layers are not always consistent between exfoliated single crystal materials and large-area synthesized films, which calls for further study on these synthesized materials³².

Several synthesis methods have been reported, including chemical vapor deposition (CVD) of monolayer MoS₂ using MoO₃ and S precursors^{33,34}. While this method produces uniform and high-quality monolayer and bilayer films, precise thickness control for few-layers or even thin films of MoS₂ is challenging with this. On the other hand, thermal vapor sulfurization (TVS) that utilizes sulfurization of a precursor Mo film on the substrate has great control over thickness. In this method, the final MoS₂ film thickness directly depends on the precursor Mo film thickness³⁵. To its disadvantage, this method is not preferred to grow monolayer films as it suffers from small grain sizes and poor transport properties, i.e., low electron/hole mobility. However, despite the advances in these and other growth methods, the fundamental electronic and optical properties of these films still require better understanding. Since these 2D materials have been proposed and demonstrated to have superior characteristics in optoelectronic device applications such as transistors, photodetectors, photoemitters, and photovoltaics, understanding how these materials interact with different bandwidths of light at various thicknesses is crucial. While monolayer films exhibit the maximum photoluminescence, they only absorb on the order of 10% of the visible spectrum³⁶. Hence, a few-layer film or even a thicker thin-film (>~3 nm thick that shows bulk-like properties³⁷) of MoS₂ is possibly a better candidate for some optoelectronic applications, e.g., photovoltaics.

The complex refractive index is the most fundamental material property that describes the light-matter interaction in these 2D MoS₂ layers. Several previous reports have shed light on the complex refractive index (or the complex dielectric function, where one can be calculated from the other) of monolayer and few-layer MoS₂³⁸. Many of these reports have been indirect calculations of the n and k values, while some direct measurements are

performed only for a small bandwidth of the spectrum. Li et al. reported the complex dielectric function of exfoliated monolayer TMDC materials, including MoS₂, from reflection spectra using the Kramers-Kronig analysis³⁶. Since reflection spectroscopy depends on light intensity, and thus all reflected light needs to be collected from the samples, these measurements are difficult to do accurately. Also, intensity based techniques are generally dependant on interference effects which are not present for very thin films and are thus less sensitive to low-dimensional materials with small thicknesses. Shen et al. and Liu et al. reported the complex refractive index of 2D MoS₂ using spectroscopic ellipsometry for only monolayer materials^{39,40}. On the other hand, Yim et al. reported n and k data for few-layer MoS₂ samples grown by the TVS method between 380 and 900 nm using ellipsometry at a single angle of incidence⁴¹. Li et al. and Park et al. also reported the complex refractive index of few-layer MoS₂ films grown by TVS and CVD methods, respectively, using spectroscopic ellipsometry up to 1240 nm^{42,43}. Lastly, a recent report by Ermolaev et al. shows the complex refractive index of monolayer and bulk MoS₂ in the 290-3300 nm spectral range but does not include interesting data in the UV region below 290 nm⁴⁴.

Here we report variable angle spectroscopic ellipsometry (VASE) measurement and subsequent extraction of the complex refractive index of monolayer, few-layer, and thicker thin-film MoS₂. The reported data ranges from 190 nm to 1700 nm covering a wide range of incident angles and wavelengths. Acquisition of spectroscopic data allows the determination of the optical properties (n and k) in transparent and absorbing regions over the widest possible spectral range. Data acquisition at multiple angles is desirable, as each angle presents a different path length through the film stack, and all angles can be analyzed

simultaneously for film thicknesses. The VASE measurements and models shown below were performed by our collaborator Ron Synowicki at J.A. Woollam Inc.

VASE is a non-destructive characterization method that has great potential for studying 2D films because of its higher sensitivity to small thickness changes, resulting primarily from the measurement of the polarization state instead of intensity, including the phase difference between the p- and s-polarized components⁴⁵⁻⁴⁷. For example, ellipsometry is commonly used to determine the thickness of native oxide films on semiconductor wafers and is effective for extremely thin films down to the monolayer level, such as those studied in this work.

The monolayer sample studied here was grown by the CVD method, while the few-layer and thin-film samples were grown by the TVS method. The films were also characterized by Raman spectroscopy, photoluminescence (PL), atomic force microscopy (AFM), and UV-Vis-NIR spectroscopy for quality and thickness validation. The complex refractive index was used to model reflectance, transmittance, and absorption using the transfer matrix method and matched with experimentally measured data. Finally, an optical model was built to study the effect of utilizing various optical coatings to confine absorption in a narrow bandwidth or to enhance broadband absorption in monolayer, few-layer, and thin-film MoS₂ for various optoelectronic applications, such as photodetectors, sensors, and photovoltaics.

2.1 MoS₂ Synthesis

Monolayer MoS₂ films were grown using the CVD method, as it provides good film quality in this thickness regime, while the TVS method was used to grow few-layer and thin-film

MoS₂ for its better thickness control. Figure 2.1 shows a schematic of the three-zone furnace used for both the CVD and TVS growth. For the monolayer films, MoO₃ and S powders were placed inside a 1” tube. The tube is initially pumped down to 15 mTorr base pressure, and then Ar is flowed as a carrier gas at 2.5 sccm flow rate. C-plane sapphire substrates were placed growth-face-down on a ceramic crucible that contains the MoO₃ powder and is set in the second zone of the furnace at 750 °C, as shown in Fig. 1 (top). Sulfur powder is kept in a crucible in the first zone at 120 °C. The spacing between two crucibles is optimized to be around 30 cm. The ramp time to 750 °C is 30 mins, and the deposition is carried on for 10 mins. The tube pressure is maintained at 2.4 Torr during deposition. After the deposition, the monolayer MoS₂ films are transferred to a SiO₂-on-Si substrate for characterization⁴⁸. For the TVS method, a Mo precursor film was grown on sapphire or SiO₂-on-Si substrates using electron-beam evaporation, where the thickness of the precursor Mo film determines the final MoS₂ thickness³⁵. The substrate is then placed on the third zone for growth on the top side, and S powder is loaded on a crucible in the first zone of the furnace, as shown in Figure 2.1 (bottom). The spacing between the two crucibles in this case is optimized to be around 50 cm. The tube is then pumped down to a 15 mTorr base pressure, and Ar carrier gas flows at 100 sccm flow rate. The temperature in the third zone is set at 900 °C with a 90 min ramp time, and the first zone is set at 120 °C. The deposition is carried out for 10 mins while the pressure in the tube is maintained at 1.2 Torr.

An alternative growth method tried for few-layer and thin-film MoS₂ synthesis utilizes solution processing and rapid thermal annealing for high throughput and described in detail by Robertson et al.⁴⁹.

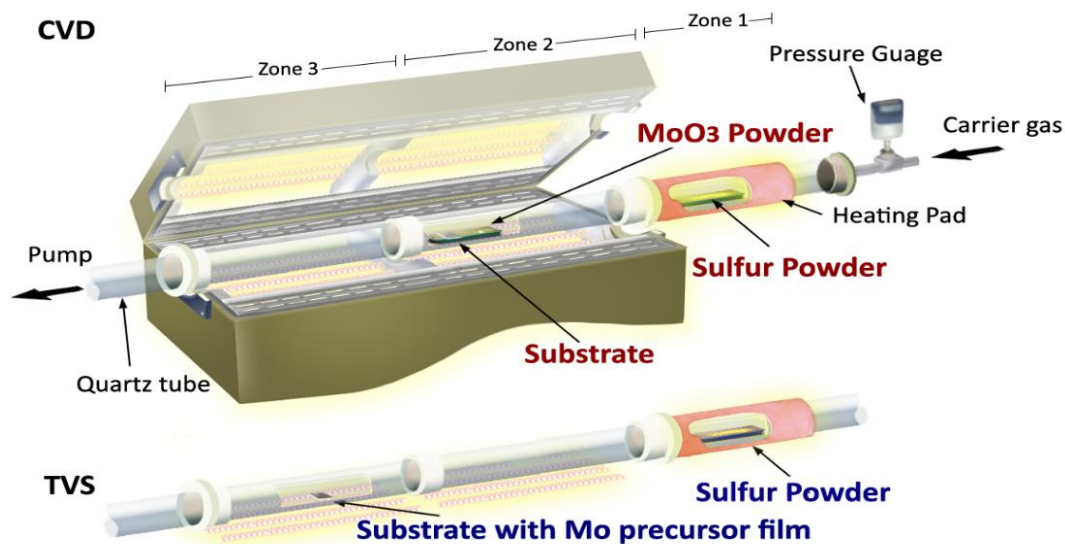


Figure 2.1 Schematic of the two synthesis methods used in this study: chemical vapor deposition (CVD) and thermal vapor transport (TVS). A standard two-zone furnace is modified to have a third zone for low-temperature sulfur (S) evaporation and to increase the distance between the S source and the growth substrate.

2.2 Physical Properties of MoS₂

The samples were characterized for quality and precise thickness control using Raman spectroscopy, PL, AFM, VASE, and UV-Vis-NIR spectroscopy. Figure 2.2a shows Raman scattering plots of monolayer, few-layer, and thin-film MoS₂ samples. The E¹_{2G} and A_{1G} peaks are located at 386.5 & 406 cm⁻¹, respectively, for monolayer MoS₂, at 386 & 408.5 cm⁻¹, respectively, for few-layer MoS₂, and at 385.5 & 411 cm⁻¹, respectively, for thin-film MoS₂. The 19.5 cm⁻¹, 22.5 cm⁻¹, and 25.5 cm⁻¹ spacings between the E¹_{2G} and A_{1G} peaks are consistent with previous reports³⁷, confirming their respective thicknesses. Figure 2.2b shows normalized PL intensity of as-grown monolayer MoS₂ on a sapphire substrate, showing the excitonic A-peak at ~670 nm. The PL peak has 20.2 nm full-width at half

maximum (FWHM), confirming good optical quality. This PL is a signature characteristic of monolayer TMDC films.

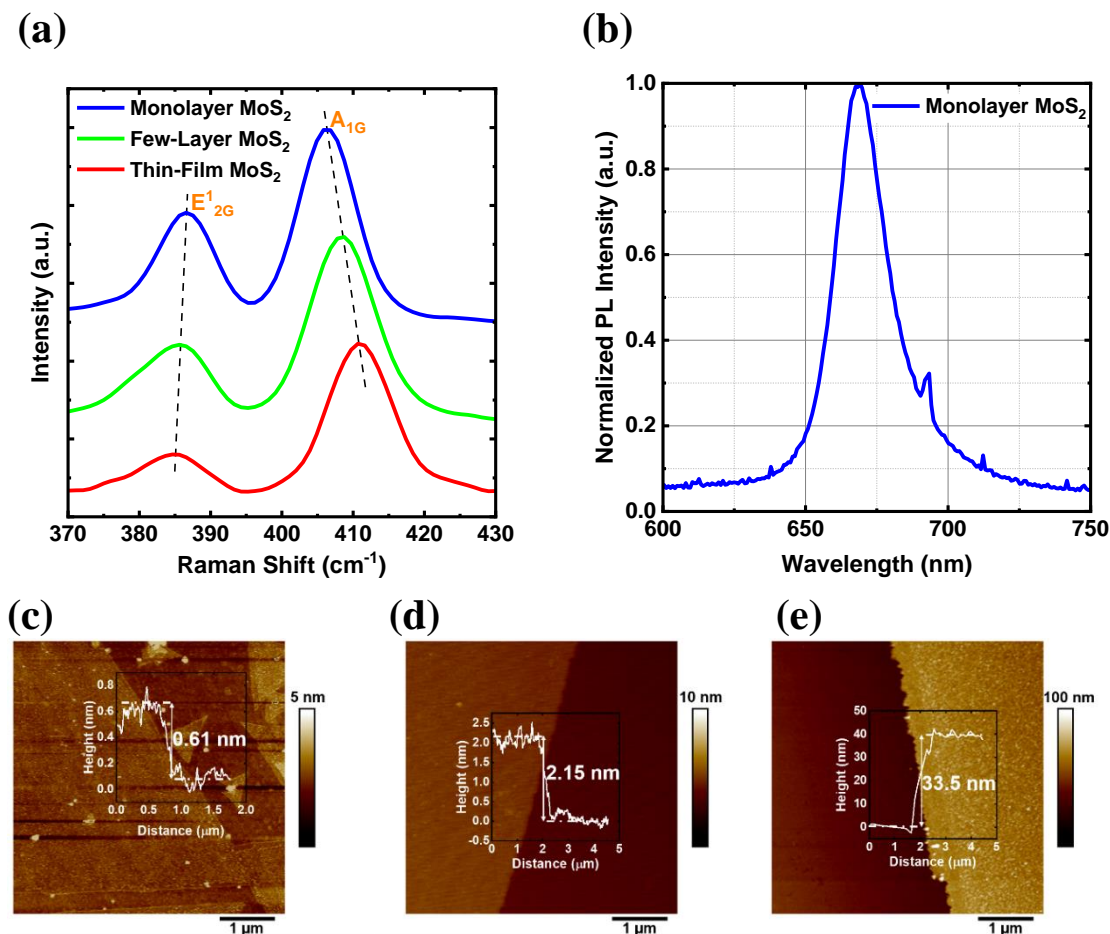


Figure 2.2 (a) Raman characterization of the CVD and TVS grown MoS₂ samples on SiO₂-on-Si substrates using a 532 nm laser source. (b) Photoluminescence (PL) spectra of a monolayer MoS₂- sample with an emission peak near 670 nm, using a 405 nm excitation source. AFM images showing step height and topography of the (a) monolayer, (b) few-layer, and (c) thin-film MoS₂ samples.

Figure 2.2 c, d, and e show AFM topography of the three samples. The average step height is measured as 0.61 nm, 2.15 nm, and 33.5 nm for the ‘monolayer’, ‘few-layer’, and ‘thin-film’ samples, respectively. The samples were measured for step heights at three different

locations within a cm^2 area, and the film thickness variation is within $\pm 10\%$, showing good uniformity. UV-Vis-NIR spectroscopy was also used to measure transmittance across a cm-scale sample to confirm uniformity of optical properties as shown in Figure 2.3.

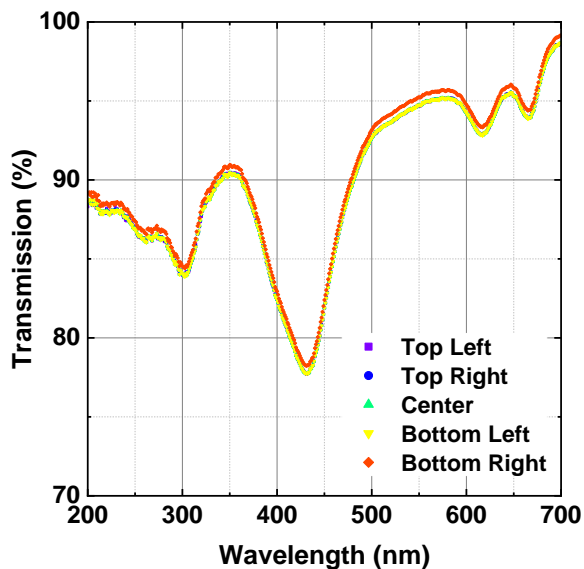


Figure 2.3 Transmission spectra of monolayer MoS_2 as-grown on sapphire measured at five different locations (four corners and center of a $1\text{cm} \times 1\text{cm}$ sample) showing uniform optical properties across a cm-scale sample.

2.3 Ellipsometric Characterization of MoS_2

Ellipsometry measures the change in polarization state of light reflected from or transmitted through a sample. The principle of reflection-mode ellipsometry is shown in Figure 2.4a where the change in polarization caused by the sample is recorded as two experimentally measured values Ψ and Δ . This process is repeated for a plurality of angles and wavelengths using the VASE technique. Data were acquired at five angles of incidence from 55 to 75 degrees in steps of 5 degrees and over the spectral range from 190 nm to 1700 nm. All angles and wavelengths were fit simultaneously in the data analysis.

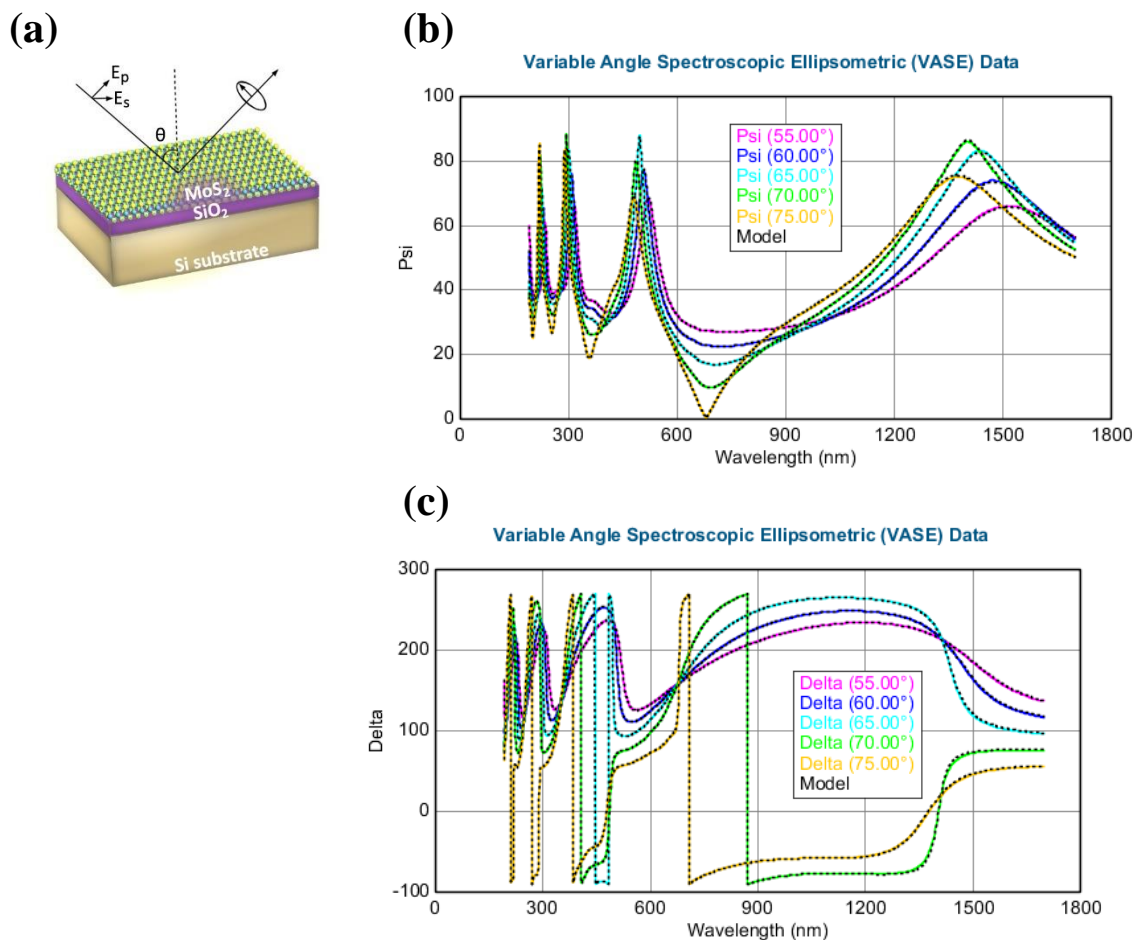


Figure 2.4 (a) Schematic of the spectroscopic ellipsometry measurements showing the optical model of the $\text{MoS}_2\text{-SiO}_2\text{-Si}$ samples. Measured and modeled (b) Ψ and (c) Δ spectra of monolayer MoS_2 versus wavelength. The solid colored lines are measured data at various angles of incidence, and the dashed black lines are modeled fit values with good agreement obtained over the full spectral range.

Figures 2.4 b and c show the experimentally measured Ψ and Δ data as solid curves along with the model fitted data as dotted curves generated by the data analysis for the monolayer MoS_2 film. To extract properties of interest about a sample, such as film thickness and optical constants n and k , ellipsometry data analysis requires constructing an optical model to match the experimentally measured Ψ and Δ values. The optical model contains the optical constants n and k of the substrate, as well as the thickness and optical constants n

and k of each layer in the stack. The data analysis software allows for fixing some properties of the model while allowing some parameters to be defined as adjustable variables. The analysis software adjusts the variable parameters to find the best match to fit the experimental Ψ and Δ curves⁴⁵⁻⁴⁷. In this work, the optical constants of the silicon substrate, thermal SiO_2 layer, and 1 nm interface layer were taken from published values and not allowed to vary⁵⁰ and are not expected to change noticeably after film deposition and thermal processing.

Determining the optical constants n and k of thin films via ellipsometry is generally more accurate for thicker films due to longer path length in the film. In this work we first analyzed the thickest ‘thin-film’ MoS_2 for film thickness and optical constants, then attempted to apply these optical constants to the very thin monolayer and few-layer MoS_2 films by keeping the optical constants fixed from the thicker film and fitting only the film thickness. It was found that the monolayer and few-layer samples did not analyze well using optical constants from the thickest sample, demonstrating the sensitivity of the optical constants to film thickness.

A further complication is the few-layer and thin-film MoS_2 films tended to show some level of nonzero absorption over the entire measured spectral range. To maximize sensitivity to the optical constants of such thin absorbing films, we applied the techniques of multiple angles of incidence, optical constant parameterization, and interference enhancement discussed by McGahan et.al^{51,52} and Hilfiker et.al⁵³. For interference enhancement, the thin absorbing film is deposited over a much thicker transparent film, such as 300 nm thermal SiO_2 in this work. This places the thin absorbing MoS_2 film between the transparent ambient above and the transparent SiO_2 film underneath, which

allows absorption in the MoS₂ film to affect the amplitude of interference features in the Ψ and Δ spectra caused by the thick transparent SiO₂ film underneath.

Since the MoS₂ films are so thin, parameterizing the optical constants via a dispersion model for the optical constants works well, particularly when the model enforces Kramers-Kronig consistency on the shape of the n and k curves. A dispersion model also allows the data to be fit using a minimum number of adjustable parameters. Earlier published works investigated combinations of Lorentz^{39,40,42,43}, single Tauc-Lorentz⁴¹, and multiple Tauc-Lorentz dispersion models with separate band gaps for each Tauc-Lorentz term⁴⁴. Additionally, all the models to analyze MoS₂ in these previous works were isotropic and did not investigate birefringence in the MoS₂.

In this work, a variety of dispersion models enforcing Kramers-Kronig consistency were investigated, including Lorentz, Tauc-Lorentz, Sellmeier, Gaussian, and combinations of these^{54,55}. We also used a Kramers-Kronig consistent B-Spline model for MoS₂ optical constants⁵⁵. Advantages of the B-Spline model include maximum flexibility to the lineshape of the dielectric function, including the exciton peaks of MoS₂, without assuming the lineshapes of Lorentz, Gaussian, or other function for each oscillator. The B-Spline node spacing is also adjustable throughout the fitted spectral range, allowing for extra resolution to be defined through regions of interest such as the exciton peaks. Furthermore, the B-Spline analysis of MoS₂ in this work did not require additional parameters such as offsets to the real part of the dielectric function or Sellmeier Pole functions to fit the data, whereas analysis with Gaussian, Lorentz, or Tauc-Lorentz functions did require these extra

adjustments. The B-Spline fits also showed a slightly better goodness of fit, resulting primarily from the extra flexibility of the B-Spline lineshape.

Each sample was fit first to an isotropic model with no birefringence in the MoS₂ index, similar to previous works mentioned. Adding birefringence to allow different optical properties in-plane (ordinary index) and out-of-plane (extraordinary index) improved the fit significantly for the thickest thin-film sample, likely due to the longer path length through this thicker film with more layers in the layered structure. The in-plane optical constants describe the refractive index and absorption features over the full spectral range. In contrast, the out-of-plane refractive index was described using a single Sellmeier dispersion function, similar to the method presented by Hong et al. for analyzing birefringent plastic substrates⁵⁵. As mentioned by Ermolaev et. al. sensitivity to the out-of-plane refractive index is greatly reduced as light entering the sample propagates near normal to the surface due to the high index of MoS₂ and is thus much more sensitive to the in-plane index component, justifying a simple transparent Sellmeier for the out-of-plane index component⁴⁴. Thus, the birefringence effect was only seen in the thickest thin-film MoS₂ sample and only for wavelengths with relative low absorption. It is likely that the monolayer and few-layer MoS₂ also exhibit anisotropy, though the optical response of the out-of-plane component was not strong enough to definitively conclude that here.

Analysis of each MoS₂ film is described below.

2.3.1 Analysis of Thin-Film MoS₂

Analysis of the ellipsometric data started with the thickest film, the “thin-film” MoS₂ sample. Isotropic models using B-Spline functions or combinations of Sellmeier and

Gaussian functions were fit, followed by testing for birefringence by converting to an anisotropic, birefringent model. The birefringent model showed significant improvement to the psi and delta curves and improved the goodness of fit by over 50%, justifying the addition of uniaxial birefringence to the model. Fitting a surface roughness/oxide layer 8.1 nm thick also significantly improved the fit.

Figure 2.5 shows the birefringent refractive index n and k for the thin-film MoS_2 fitted with Gaussians (dotted lines) and B-Spline dispersion functions (solid lines) with nearly identical results. For the Gaussian model, the in-plane refractive index was fitted to 17 Gaussian and 1 Sellmeier dispersion functions. For the B-Spline fit, the node spacing was set to 0.05 eV over the full range. For both models, the out-of-plane index was fit to a single Sellmeier model. Note in Fig. 4, the out-of-plane index (Sellmeier model) is plotted only to 1.3 eV (arbitrarily chosen to match the bandgap of bulk MoS_2) as the material becomes highly absorbing at higher photon energies above the bandgap. As the absorption increases, the sensitivity to the out-of-plane response disappears. The in-plane optical response dominates due to the high index causing the strongly refracted light to propagate almost entirely in-plane in the material. The transverse electric field senses the in-plane optical response much more than the out-of-plane component. Therefore, the ellipsometric measurement is sensitive to the in-plane optical response at all wavelengths. However, only in the transparent region below the bandgap is the measurement is sensitive to the birefringence and thus sensitive to both the ordinary and extraordinary components of the refractive index.

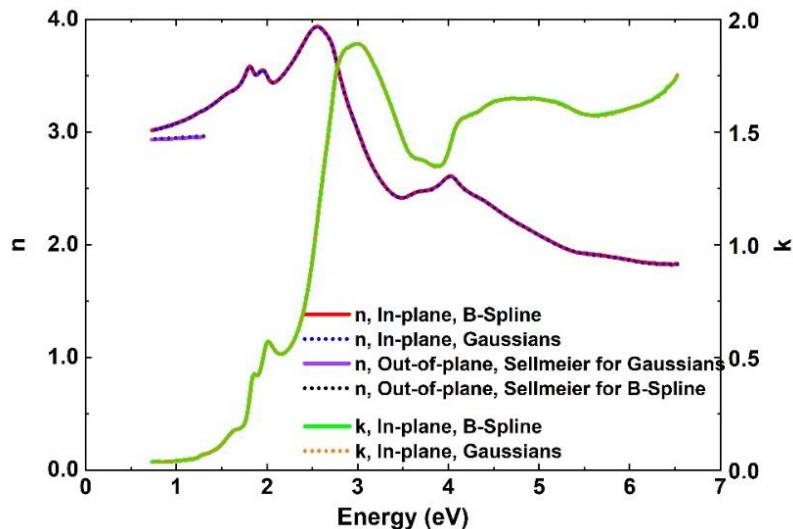


Figure 2.5 Optical constants n & k for thin-film MoS_2 analyzed using a birefringent model. The in-plane index was fitted using B-Spline model (solid lines) or a combination of Gaussian and Sellmeier functions (dotted lines) with nearly identical results. The out-of-plane component was fit to a single Sellmeier function and plotted above to 1.3 eV.

In Figure 2.5, the k -values show the expected A and B exciton peaks at 1.8 and 2.0 eV, similar to results reported for a 12-layer MoS_2 film by Park et al.⁴³ Note an additional peak at 1.6 eV and defect absorption tail extending below, possibly from incomplete sulfurization of the precursor molybdenum film and/or inhomogeneous crystallization. Strong absorption is seen near 3 eV, consistent with Liu et al.⁴⁰ and Park et al.⁴³ An additional peak is seen at 3.7 eV, and much smaller peaks occur near 4.3 and 5.8 eV mentioned by Li et al.⁴² and Park et al.⁴³

2.3.2 Analysis of Few-Layer MoS_2

The few-layer MoS_2 sample was also fit to an isotropic model using a Gaussian and Sellmeier dispersion model, where 2 Sellmeier and 6 Gaussian functions were used for the Gaussian model fit.. The A and B exciton doublet peaks appear blended into a single peak

near 1.9 eV. Similar to the thin-film sample, a defect absorption tail is present down to 0.7 eV, again possibly due to incomplete sulfurization of the precursor molybdenum film in the TVS process. The peak near 3 eV is more asymmetric, with a shoulder peak near 3.4 eV.

2.3.3 Analysis of Monolayer MoS₂

The monolayer MoS₂ film was analyzed with an isotropic model using a Gaussian plus Sellmeier model. 2 Sellmeier and 6 Gaussian functions were used for the Gaussian model fit. The positions of the A and B excitons at 1.91 and 2.05 eV, respectively, are blue-shifted compared to the thin-film sample analyzed above and similar to the values of 1.88 and 2.03 eV reported by Shen et al.³⁹ The large absorption near 3 eV is prominent, along with additional smaller absorptions more prominent than observed in the thin-film sample.

For comparison, Figure 2.6 shows the in-plane refractive index (a) and extinction coefficient (b) for all three MoS₂ films above plotted versus wavelength.

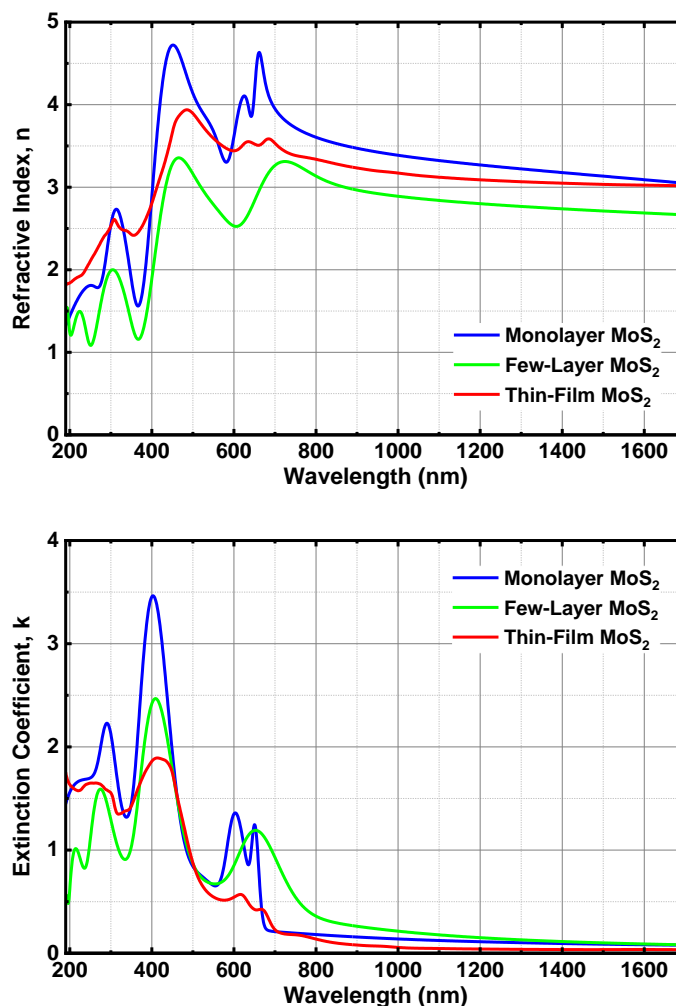


Figure 2.6 In-plane optical constants, n and k , for monolayer, few-layer, and thin-film MoS₂. The refractive index, n , is shown at the top, while the extinction coefficient, k , is shown at the bottom.

2.4 UV-Vis-NIR Spectroscopy

UV-Vis-NIR spectroscopy is used to measure the transmittance of the monolayer, few-layer, and thin-film MoS₂ samples. These samples were all grown on sapphire substrates, and transmittance through the bare substrate is used as a baseline correction. The measurements are done on relatively large areas of the samples (mm-wide) with an integrating sphere, essentially giving a good average that accounts for spatial

inhomogeneity. Figure 2.7a shows the transmittance vs. wavelength for the samples between 190 nm and 1700 nm, the same spectral range for which the spectroscopic ellipsometry measurements are done. For the monolayer MoS₂ sample, the excitonic A, B, and C troughs are evident at around 670 nm, 620 nm, and 425 nm, respectively^{36,58}. The few-layer sample also shows a trough at around 425 nm, while it is blue-shifted for the thin-film sample. The thin-film sample shows two small troughs at around 670 nm and 620 nm as well³⁶. For the monolayer and few-layer films, we see an additional trough in the UV at around 300 nm that is also consistent with our measured n and k values and previously published results^{42,43}.

2.5 Optical Modeling

An optical model is built to calculate transmittance through the bare monolayer, few-layer, and thin-film MoS₂ using the complex refractive index extracted from spectroscopic ellipsometry measurements and matched with the experimentally measured transmittance data. A good match between the two data sets assures confidence in the measurements and the derived material optical property data.

The model uses the transfer-matrix method (TMM) to calculate the transmittance, reflectance, and absorption in the MoS₂ active layer^{59,60}. Figure 2.7 b, c, and d shows modeled transmittance for different thicknesses of the stand-alone monolayer, few-layer, and thin-film MoS₂ overlaid with the measured transmittance of the same films. These figures are plotted between 200 nm and 1000 nm to highlight the troughs and peaks clearly. In each calculation, the n and k data of the corresponding MoS₂ is used, i.e., for Figure 2.7b the n and k data from monolayer MoS₂ is used, and so on. As shown in Figure 2.7b, the

measured transmittance of the monolayer sample lies in between the calculated transmittance for 0.50 nm and 0.80 nm of MoS₂, confirming the monolayer thickness and validity of the complex refractive index data. The locations of the troughs for the modeled plots are slightly blue-shifted compared to the experimental plot for the monolayer sample. This is because while experimental transmittance is measured for as-grown MoS₂ samples on sapphire, the n and k data used in the models come from VASE measurements of transferred MoS₂ samples on SiO₂-on-Si substrates.

In Figure 2.7c, the models are calculated for 1.85 nm and 2.45 nm, the thickness for 3-layers and 4-layers of MoS₂, respectively. The transmittance matches better with the 1.85 nm MoS₂ sample, implying that the few-layer sample is trilayer for the most part. For the thin-film MoS₂ sample, the transmittance matches closely with 30 nm of MoS₂ for the short wavelengths while it has a better fit with 20 nm of MoS₂ in the longer wavelengths.

Given the complex nature of the refractive index of each material in the layer, the amount of light absorbed in the active layer can be determined as well from the TMM^{61,62}. The absorption coefficient can be expressed in terms of the imaginary part of the refractive index known as the extinction coefficient, k, and the free space wavelength, λ .

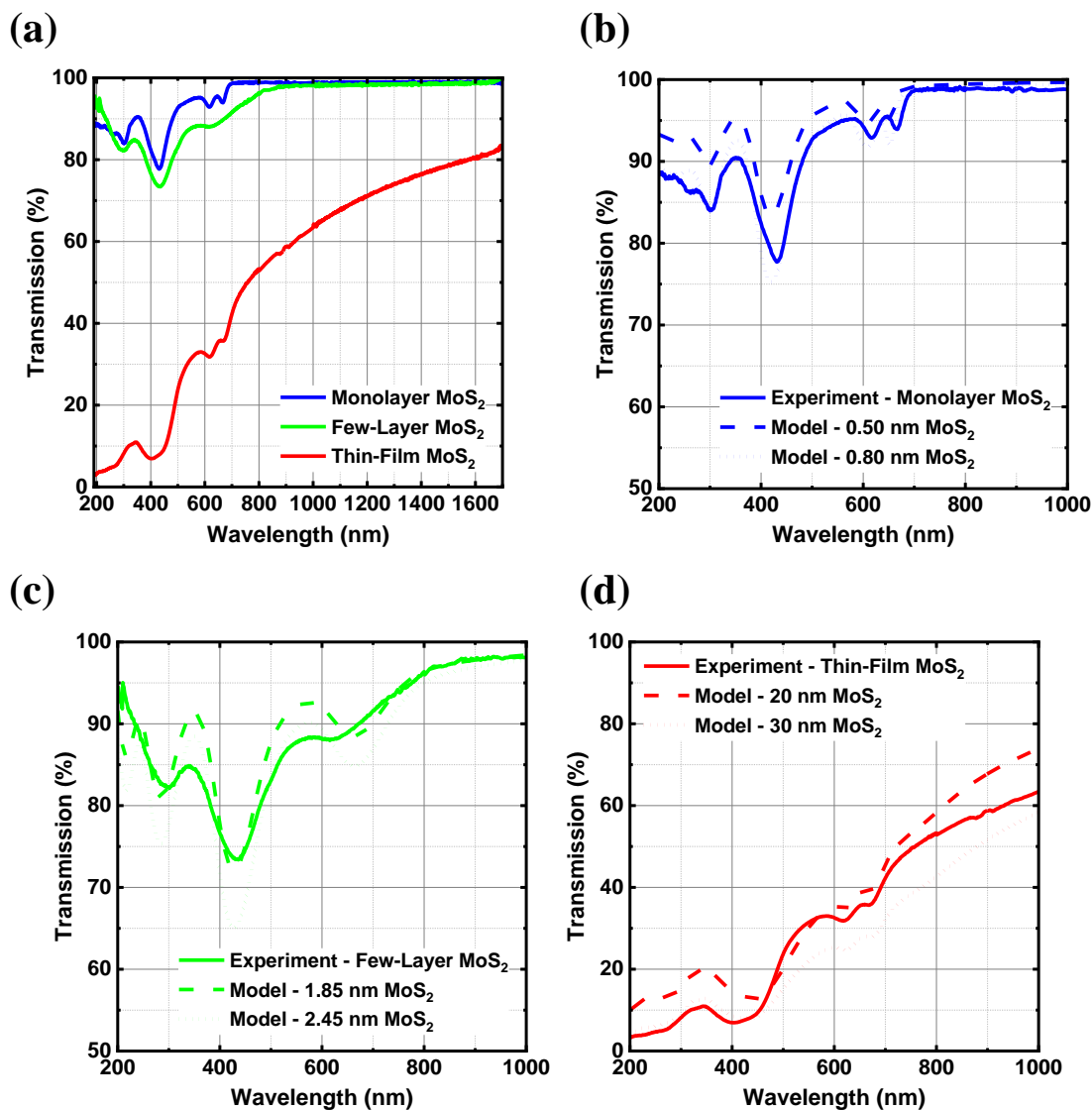


Figure 2.7 (a) Measured transmittance of monolayer, few-layer, and thin-film MoS₂ samples grown directly on sapphire. Modeled transmittance of (b) monolayer, (c) few-layer, and (d) thin-film MoS₂ samples overlaid with experimentally measured transmittance. The models use the complex refractive index data measured by spectroscopic ellipsometry.

The amount of light absorbed in each layer can be estimated using the optical density or transmittance through the film using Lambert's law:

$$\alpha = \frac{4\pi k}{\lambda}; \quad I(x) = I_0 e^{-\alpha x} \quad (3.1)$$

Where $I(x)$ is the transmitted intensity after the light has been absorbed in the lossy medium, x is the thickness of the lossy medium, I_0 is the incident intensity of light, and α is the absorption coefficient.

Figure 2.8a shows the calculated absorption (%) for monolayer, few-layer, and thin-film MoS₂ samples. The thickness used here for each sample is that from the AFM measurements, 0.61 nm, 2.15 nm, and 33.5 nm, respectively. The modeled results show that monolayer, few-layer, and thin-film MoS₂ absorb 7.4%, 12.6%, and 32.4% of the incident light, respectively, between 300 nm and 700 nm; again, they absorb 5.1%, 9.2%, and 26.1%, respectively, between 200 nm and 1000 nm.

When normalized to per unit-thickness absorption, between 300 nm and 700 nm, monolayer MoS₂ absorbs 12.1%/nm; in comparison, few-layer and thin-film MoS₂ absorbs 5.9%/nm and 1.1%/nm, respectively, clearly showing superior light-matter interaction in the monolayer and few-layer films. Figure 2.8b shows the absorption (%) per unit-thickness (nm) vs. wavelength for monolayer, few-layer, and thin-film MoS₂.

The plots are cropped between 200 nm and 800 nm to highlight the prominent excitonic absorption peaks in 2D MoS₂, i.e., monolayer and few-layer MoS₂, compared to the flat and low absorption profile of the thin-film MoS₂ sample.

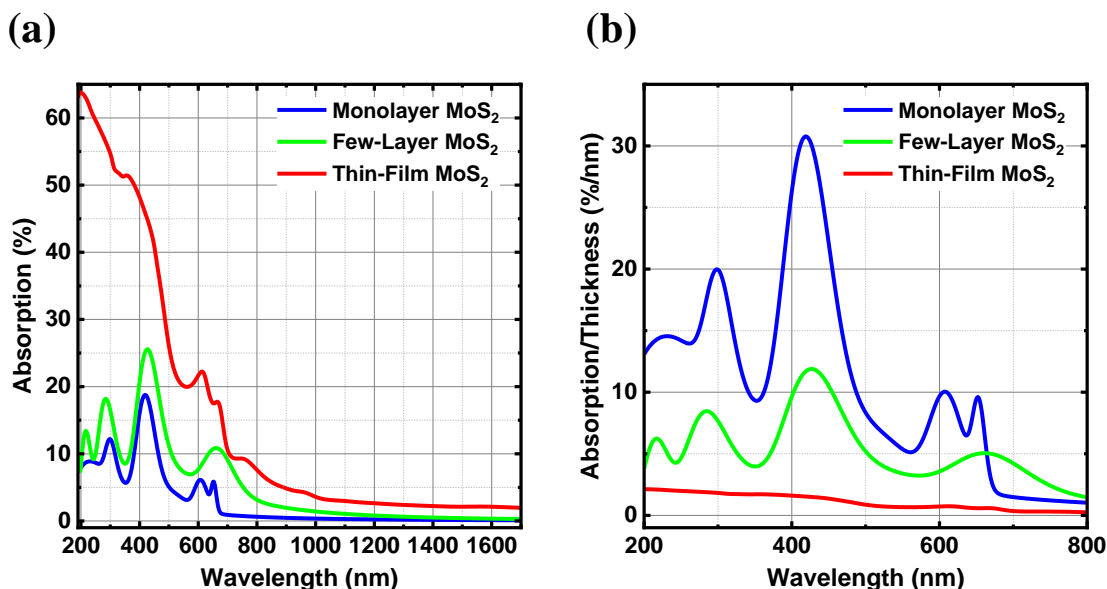


Figure 2.8 (a) Modeled absorption of monolayer, few-layer, and thin-film MoS₂ using the complex refractive index measured by spectroscopic ellipsometry as shown in Figure 2.6. (b) Absorption per unit thickness is plotted vs. wavelength.

As an example of the usefulness of this optical property data, the absorption models are further expanded to design optical coatings on top of the MoS₂ layers to either limit absorption within a specific spectral bandwidth or enhance broadband absorption in the MoS₂ active layers. The former is useful for designing photodetectors and sensors, while the latter is useful for designing photovoltaic solar cells using these 2D materials. This modeling again utilizes the TMM.

Figures 2.9 a and b show contour plots of absorption (%) in monolayer and few-layer MoS₂, respectively, between 200 nm and 800 nm for a range of TiO₂ thicknesses. The thickness of the monolayer and few-layer MoS₂ is set at 0.61 nm and 2.15 nm, respectively. While monolayer and few-layer MoS₂ absorb significantly in the UV as-is, a thin coating of TiO₂ on top can limit the absorption to the visible spectrum only. For example, monolayer MoS₂

absorbs 7.8% of 200 nm monochromatic incident light, whereas with a 75 nm TiO₂ coating on top the same absorption goes below 0.1%. The same is true for thin-film MoS₂; 100 nm of TiO₂ reduces few-layer MoS₂ absorption at 200 nm from 8.8% to ~0%.

Figure 2.9c shows the broadband absorption vs. wavelength in a thin-film MoS₂ layer for multiple thicknesses of ITO as an anti-reflection coating (ARC). While different ITO thickness enhances the absorption in the MoS₂ layer in different parts of the spectrum, the maximum broadband absorption is achieved with 40 nm of ITO on top of the MoS₂ thin-film, going from 29.1% without any ARC to 40.7%, for the 300 nm to 800 nm spectral range. In contrast, when the solar irradiance and spectrum is considered, 60 nm of ITO outperforms the other ITO thicknesses in terms of photocurrent generation in a photovoltaic device.

Furthermore, various common ARCs are studied for enhanced broadband absorption in thin-film MoS₂, as shown in Figure 2.9d. A range of thicknesses for each ARC is considered, and only the optimized thickness in terms of broadband absorption enhancement is shown in the figure. For example, 60 nm of SiN on top of the thin-film MoS₂ increases the broadband absorption between 300 nm and 800 nm by 44.1%, relatively, from 29.1% absorption without any ARC to 41.9% absorption with the addition of the SiN layer. The thickness of the thin-film MoS₂ layer is set to 35 nm for Figure 2.9 c and d.

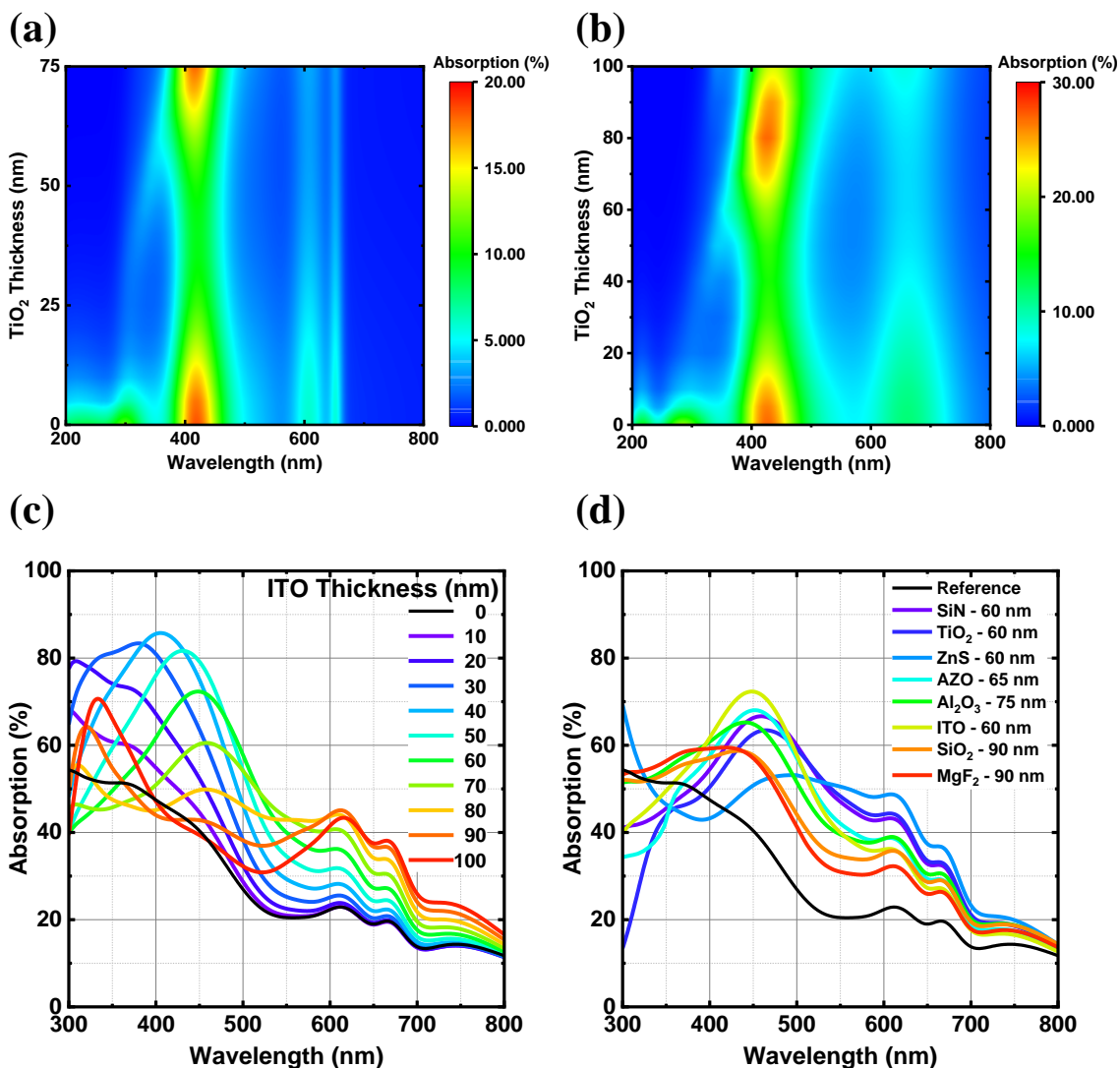


Figure 2.9 Calculated absorption (%) in (a) monolayer and (b) few-layer MoS₂ vs. wavelength for a range of TiO₂ thickness on top. The optical stacks here are modeled as air-TiO₂-MoS₂-air and only the absorption (%) in the active MoS₂ layers is plotted. (c) Calculated absorption (%) in thin-film MoS₂ for a range of ITO thickness as an ARC. (d) Various ARCs are studied to enhance the broadband absorption in thin-film MoS₂.

Finally, relatively thicker thin-film MoS₂ films are used in the model to maximize absorption for useful photovoltaic device application and maximum theoretical short-circuit current density (J_{sc}) is calculated assuming 100% internal quantum efficiency (IQE)

under AM1.5G illumination, as shown in Figure 2.10^{61,62}. This means that all the photons that are absorbed are converted to an electron-hole pair and are collected before they recombine.

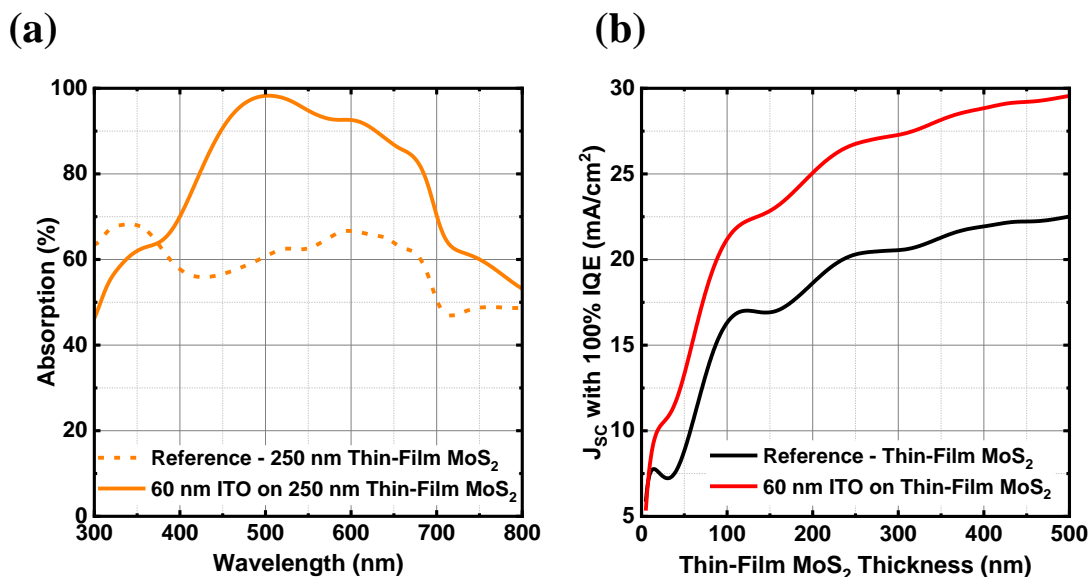


Figure 2.10 Modeled absorption (%) and J_{sc} of a thin-film MoS₂ photovoltaic device with 100% IQE. (a) Absorption (%) in 250 nm thin-film MoS₂ with and without 60 nm ITO on top as an ARC; (b) J_{sc} vs. thin-film MoS₂ thickness (5 nm - 500 nm) with and without 60 nm ITO

The models show that 100 nm of thin-film MoS₂ by itself absorbs 55.3% of the incident light between 300 nm and 800 nm whereas an addition of 60 nm of ITO on top increases that absorption to 68.8%, a relative increase of 24.4%. On the other hand, 250 nm of thin-film MoS₂ absorbs 77.9% and 59.4% with and without 60 nm of ITO on top in the same spectral range, respectively, showing a 31.1% relative increase. Lastly, the J_{sc} of a photovoltaic device made with 250 nm thin-film MoS₂ as an absorber layer can be enhanced from 20.3 mA/cm² to 26.8 mA/cm² with the addition of the 60 nm ITO coating, a 32% relative increase, assuming 100% IQE.

2.6 Conclusions and Future Work

In summary, monolayer, few-layer, and thin-film MoS₂ have been synthesized using CVD and TVS methods. The complex refractive index n and k of these samples has been extracted from VASE measurements for a broad spectral range between 190 nm to 1700 nm. The ellipsometry data showed sensitivity to optical birefringence in the thickest thin-film sample, and an analysis method was presented. The complex refractive index is then used to calculate reflectance, transmittance, and absorption of the MoS₂ films using TMM and matched with experimentally measured transmittance of the same samples.

One important way this study contributes to the broad scientific literature is by making the complex refractive index of 2D MoS₂ available for a large spectral range spanning the UV-Vis-NIR regions of the spectrum. This study also further guides how to design optoelectronic devices using simple optical coatings in conjunction with these 2D material properties.

Research is fast moving towards the realization of wearable, flexible, and transparent optoelectronic devices using 2D materials. Materials like ITO may be used as a transparent conductive oxide, serving as anti-reflection coatings to improve the broadband absorption of atomically-thin photovoltaics made with 2D MoS₂ while eliminating the need for an opaque metal contact. To that end, the optical properties and results shown here are promising and significant for designing next-generation optoelectronic devices with 2D materials.

As stated above, monolayer and few-layer MoS₂ are also very likely to exhibit anisotropic optical properties. Future work should include characterization of monolayer and few-layer

MoS₂ and other TMDCs for out-of-plane refractive index anisotropy and birefringence. Also, the study of substrate induced anisotropy in 2D TMDCs can provide useful information for designing 2D optoelectronic devices on various substrates, and as such this needs to be carefully studied.

Methods

Film Synthesis. The films are synthesized using an MTI OTF-1200X-II Dual Zone Split Tube Furnace that is modified to add a low-temperature third zone with a Grainger SLR series silicone heating blanket. The ACS reagent, $\geq 99.5\%$ molybdenum (VI) oxide (MoO_3), and the 99.98% trace metals basis sulfur (S) powder were bought from Sigma-Aldrich, while the molybdenum (Mo) pellets for electron-beam evaporation was purchased from Kurt J. Lesker Company.

Film Transfer. A surface-energy-assisted film transfer process developed by Gurarslan et al.⁴⁸ was used to transfer the MoS_2 films onto SiO_2 -on-Si substrate. 3 to 5 drops of 15 wt% solution of polystyrene (PS) in toluene is spin-coated on to the as-grown MoS_2 film on sapphire at 500 rpm for 15 seconds and subsequently at 3250 rpm for 45 seconds; then the PS coated MoS_2 on sapphire is baked for 30 minutes at 90°C . A water droplet is dropped on the sample followed by assisted penetration of the water between the PS/ MoS_2 film and the sapphire substrate. Lift-off of PS/ MoS_2 from the substrate is achieved by a slight needle insertion at the edge of the PS/ MoS_2 . The PS/ MoS_2 is then transferred onto the SiO_2 -on-Si substrate and baked at 90°C for 30 minutes to remove H_2O , then for 1 hour at 130°C to smooth out the transferred film. The PS is then rinsed off with toluene followed by a 24 hours soak in toluene for complete removal of any PS residue.

Characterization. PL characterization was done at 405 nm excitation wavelength using a Fianium (now NKT Photonics) super-continuum laser and Photon, Etc. laser line tunable filters. The laser spot size was $\sim 3 \mu\text{m}$ with 1 mW power. An Ocean Optics QEPro spectrometer is used for collecting PL signals with 1000 ms integration time and three-

sample averaging. Raman characterization was conducted using a Thermo Scientific DXR Raman Microscope at 532 nm laser excitation wavelength with 5.0 mW laser power, 50 μm aperture slit, laser spot size of $\sim 2 \mu\text{m}$, with an estimated resolution of $5.5 - 8.3 \text{ cm}^{-1}$ between 3500 to 67 cm^{-1} range. AFM measurements were performed using a Bruker Dimension FastScan system in ScanAsyst mode at 2 Hz frequency.

VASE data acquisition was performed using a J.A. Woollam RC2 spectroscopic ellipsometer running CompleteEASE software over the spectral range from 190 nm to 1700 nm. Data were acquired at five angles of incidence from 55 to 75 degrees in steps of 5 degrees. Ellipsometric Ψ and Δ data were acquired every 1 nm from 190 nm to 1000 nm, and every 2.5 nm from 1002.5 nm to 1700 nm.

Transmittance measurements were taken using a PerkinElmer LAMBDA 750S UV/Vis/NIR Spectrophotometer with a 60 mm integrating sphere between 190 and 1700 nm at 1 nm data interval and 1 second cycles. The PMT UV-Vis detector slit was fixed at 2 nm while the InGaAs NIR detector slit was set to servo mode. The gains for the PMT and the InGaAs detector were set to auto and 1, respectively, while both detectors had a 0.20 s response time.

All characterization was done in air and at room temperature.

3 OPTOELECTRONIC APPLICATIONS OF 2D MoS₂

2D TMDCs such as MoS₂ are very promising candidates for future optoelectronics due to their enhanced light-matter interactions and stability at atomic thicknesses. In the previous chapter, we introduced the large-area synthesis and optical characterization of 2D MoS₂ films. This chapter focuses on the initial electronic and optical devices made with the synthesized materials- transistors and photodetectors. Here, we detail the design, fabrication, and characterization of MoS₂-based transistors and photodetectors. This work is then extended in Chapter 4 in the discussion of 2D photovoltaics. Essentially, all optoelectronic devices' basic operation revolves around two things- absorption or generation of light and electronic transport, and as such, the design principles for different devices often follow the same path.

Transistors and photodetectors serve entirely different purposes. However, a transistor can often be used as a photodetector depending on the device structure and the active semiconductor material used in the device. Here we describe the basic operations of transistors and photodetectors and discuss the results from these optoelectronic devices that can be operated as either a transistor or a photodetector. The devices are then characterized for output characteristics, transfer characteristics, and photogenerated current. From these

measurements, field-effect mobility, external quantum efficiency, and photoresponsivity is calculated.

Furthermore, a non-destructive chemical treatment method is presented to improve the photogenerated current of a MoS₂-based photodetector by orders of magnitude.

3.1 Transistors

A transistor is generally a three-terminal device that is widely used for switching in the semiconductor industry. The three terminals are commonly referred to as gate, drain, and source. Typically, a voltage is applied between the gate and source to modulate the current flow between the drain and source. Figure 3.1 shows the schematic of a three-terminal back-gated transistor. 2D materials, especially MoS₂, have been studied for transistor applications very extensively. Radisavljevic et al. demonstrated one of the first monolayer MoS₂-based high-performance transistors back in 2011 with a mobility of 200 cm²V⁻¹s⁻¹ and an on/off ratio of 10⁸ with exfoliated material¹⁰.

2D materials are particularly interesting candidates for transistors because of the almost negligible leakage current. As all carriers are confined within an atomically thin channel in transistors made with 2D materials, the gate modulation is more effective with very little to no leakage current⁶⁴.

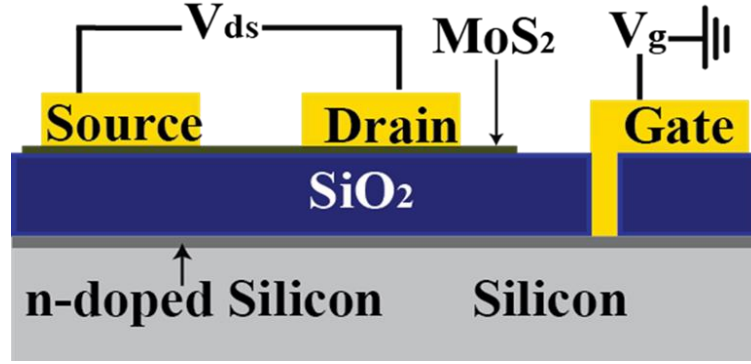


Figure 3.1 Schematic of a back-gated field-effect transistor (FET) with 2D MoS₂. The back-gate is scratched through the 300 nm SiO₂ layer and uses the highly-doped n-type silicon substrate underneath. (figure not to scale)

The field-effect mobility (μ_{EF}) is an essential metric for quantifying the electronic properties of semiconductor materials, especially of 2D TMDC materials. Typically, field-effect transistors (FETs) are fabricated to extract the mobility that gives insight into the material's electronic transport characteristics. The μ_{EF} can be calculated from the measured transfer characteristics, I_{DS} - V_{GS} sweeps for a given V_{DS} , using the FET model:

$$\mu_{EF} = \frac{dI_{DS}}{dV_{GS}} \frac{L}{WC_{ox}V_{DS}} \quad (3.1)$$

Where L and W are the length and width of the channel, respectively, and C_{ox} is the dielectric capacitance per unit area of the SiO₂ dielectric layer, given by $C_{ox} = \epsilon_0\epsilon_r/d_{ox}$, where ϵ_0 is the dielectric constant of vacuum, ϵ_r is the relative dielectric constant of 3.9 for SiO₂, and d_{ox} is the dielectric layer thickness of 300 nm. I_{DS} is the drain-source current, V_{DS} is the voltage between the drain and source terminals, and V_{GS} is the voltage between the gate and source terminals.

3.2 Photodetectors

Photodetectors are typically used as light-sensors. They absorb light or photons and convert that into electrons based on the photoelectric effect. Depending on the bandgap, different materials are used to detect different bands of the electromagnetic spectrum. 2D materials have been studied and investigated extensively for their applications in photodetectors for a wide range of bandgaps, from ultraviolet to visible to infrared^{65,66}. Photodetectors are generally two-terminal devices with a source and a drain. The basic difference between a photodetector and a transistor is that incident photons are used to excite electron-hole pairs for transport in photodetectors instead of having an electric field through gate-bias modulating the channel. Figure 3.2 shows the schematic of a transistor-type photodetector. The only difference it has with Figure 3.1 is that it doesn't have a gate terminal; instead, light is used for carrier modulation.

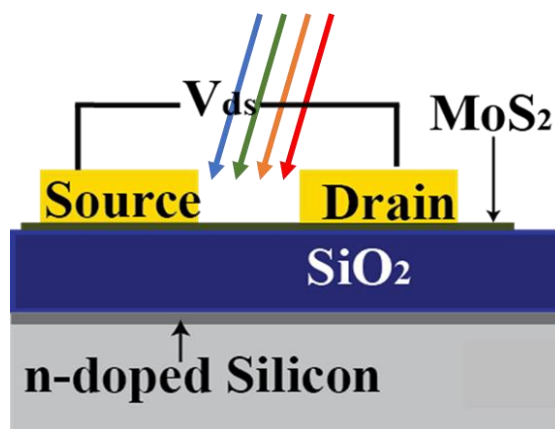


Figure 3.2 Schematic of a transistor-type photodetector with 2D MoS₂. A transistor shown in Figure 3.1 can be used as a photodetector if the carrier transport in the channel is modulated by light instead of a gate-bias. (figure not to scale)

Photoresponsivity and external quantum efficiency (EQE) is commonly used to quantify and compare photodetectors' performance.

Photoresponsivity (R) is defined as the ratio of the photogenerated current to the incident light power on the effective device area. It is expressed as $R = I_{ph}/P_{in}$, where I_{ph} is the photocurrent and P_{in} is the incident light power within the effective device area. The photogenerated source-drain current, I_{ph} , is measured at a given wavelength for a given source-drain bias, V_{DS} , and the laser incident power is also measured at that wavelength using a calibrated photodiode. The ratio between the two gives the photoresponsivity at that particular wavelength.

On the other hand, EQE is the ratio of the number of electrons generated by the device to the number of incoming photons. When we express that per unit time, the following equation is used to calculate the EQE:

$$EQE(\lambda) = \frac{\text{Electrons Out}}{\text{Photons In}} = \frac{I_{ph}(\lambda)}{q} \bigg/ \frac{P_{in}(\lambda)}{\frac{hc}{\lambda}} \quad (3.2)$$

Here, q is the charge of one electron, h is Planck's constant, c is the speed of light in vacuum, and λ is the incident wavelength in vacuum.

EQE is experimentally measured by sweeping the laser wavelength in a broad spectral range, typically between 400 and 800 nm for monolayer MoS₂-based photodetectors, accounting for their direct 1.8 eV bandgap in the monolayer form. The photogenerated source-drain current, I_{ph} , is measured at every wavelength for a given source-drain bias, V_{DS} , typically 5 V in our experiments. The laser incident power, P_{in} , is measured at each

wavelength using a calibrated photodiode. The effective power within the device channel is then calculated and plugged into the above equation to calculate EQE.

While traditional thin-film photodetectors fabricated with Si and InGaAs dominate the market, 2D materials based photodetectors have been demonstrated with excellent properties in recent years, including high EQE of 30% for graphene-WS₂-graphene⁶⁷, ultrahigh photoresponsivity up to $\sim 10^{10}$ AW⁻¹ for graphene-MoS₂⁶⁸, high photogain up to $\sim 10^8$ for graphene-MoS₂⁶⁹, and ultrahigh sensitivity of D* $\sim 10^{15}$ Jones. 2D materials are particularly attractive for photodetectors because of their extraordinary light-matter interactions and ability to absorb a much higher percentage of incoming light per unit thickness than traditional semiconductors, as discussed in Chapter 2.

3.3 Optoelectronic Device Performance

In this work, back-gated FET devices with several channel lengths and widths were fabricated, as shown in Figure 3.3. The results from the 10 μm channel length and 100 μm channel width are presented here. First, monolayer MoS₂ is grown on a sapphire substrate using CVD and then transferred on to SiO₂-on-Si substrate. The 300 nm SiO₂ layer on the Si substrate serves as the gate dielectric. Devices are then patterned using electron-beam lithography (EBL) to establish drain and source contact locations. A back-gate electrode is contacted by scratching through the oxide layer for applying a gate voltage. Finally, 5 nm of Ti followed by 45 nm of Au is deposited as source, drain, and gate contact metals using electron-beam evaporation. Details of the fabrication process is described in Appendix A.

The devices are then characterized for output characteristics, transfer characteristics, and photogenerated current.

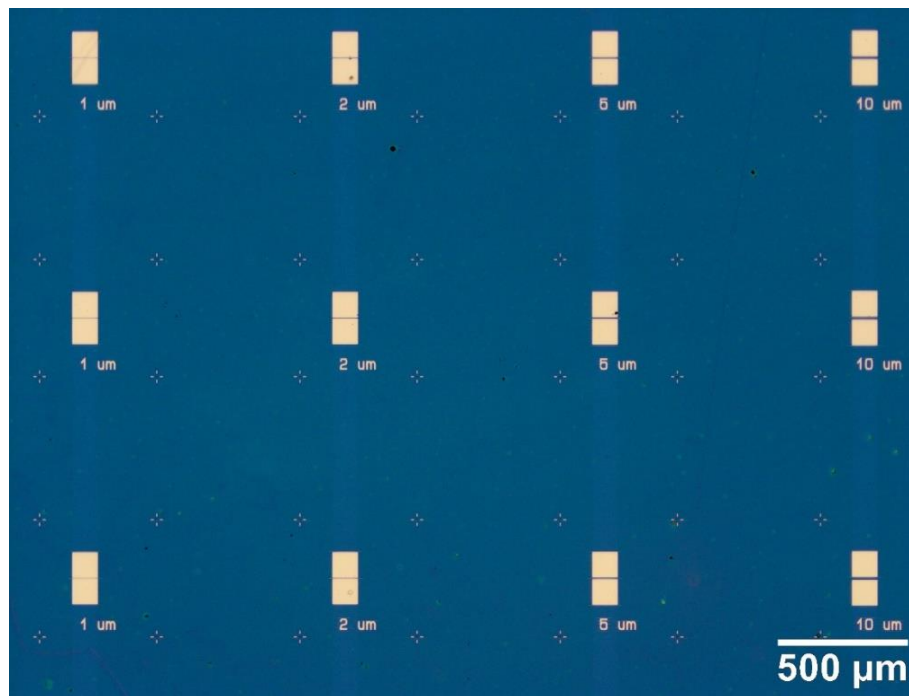


Figure 3.3 Optical micrograph of an array of devices with variable channel length and 100 μm channel width. 5 nm Ti capped with 45 nm Au is used as contacts on monolayer MoS_2 for transistor and photodetector applications. Gate contact is not shown in the image.

Figure 3.4 shows an output characteristic curve of a MoS_2 -based transistor. The source-drain voltage is swept between -5 V to 5 V for five gate biases, $V_G = -20$ V, -10 V, 0 V, 10 V, and 20 V. At negative gate biases, the channel is void of free carriers. The \sim linear $I_{\text{DS}} - V_{\text{DS}}$ behavior indicates ohmic contact between the MoS_2 and Ti/Au contacts.

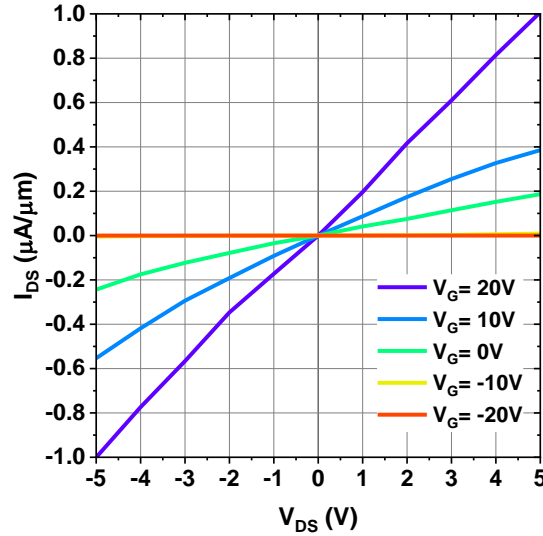


Figure 3.4 Output characteristics of a MoS₂-based FET. The source-drain voltage is swept between -5 V to 5 V for five gate biases, $V_G = -20$ V, -10 V, 0 V, 10 V, and 20 V. The red and yellow lines overlap each other.

Figure 3.5 shows a transfer characteristic curve. I_{DS} is plotted in linear (left) and logarithmic (right) scales. V_G is swept from -80V to 80V under $V_{ds} = 2, 4, 6,$ and 8 V. With positive gate voltages, the devices turn on, indicating an n-type transistor behavior. The I_{on}/I_{off} ratio of this device can reach $\sim 10^6$. From the transfer characteristic curves, the field-effect mobility is extracted as $3.3 \text{ cm}^2\text{V}^{-1}\text{s}^{-1}$, which is on par for large-area synthesized MoS₂-based transistors⁷⁰⁻⁷². The mobility could be further improved by improving the film quality during growth by introducing seed layers for larger domains and also by passivating S vacancies in the MoS₂ lattice. Previous studies have also pointed out that defect states and traps in the band structure affect the electronic transport and thus carrier mobility⁷³.

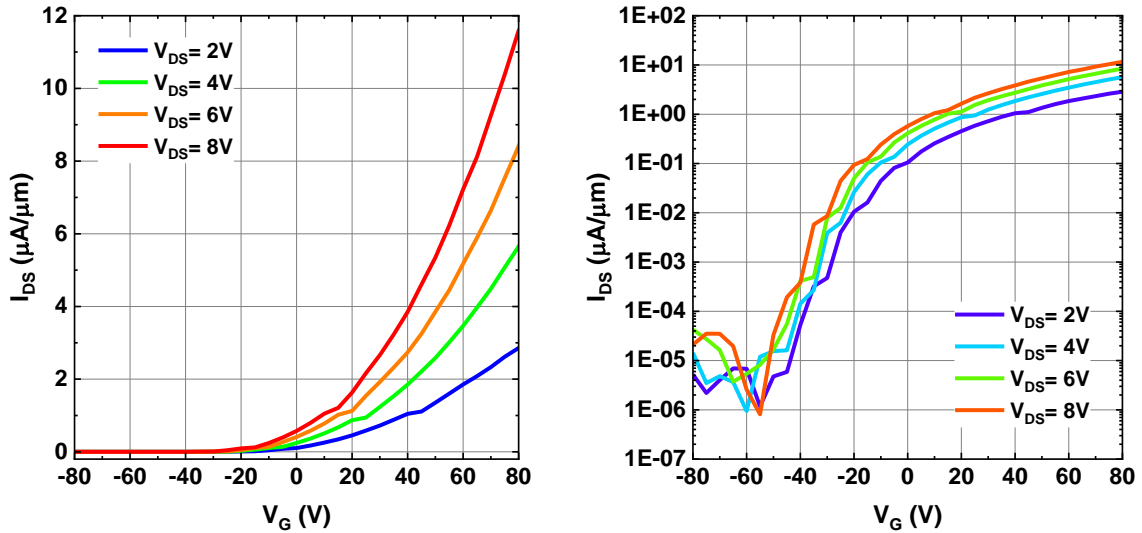


Figure 3.5 Transfer characteristics of a MoS₂-based FET. I_{DS} is plotted in linear (left) and logarithmic (right) scales. V_G is swept from -80V to 80V under $V_{ds} = 2, 4, 6,$ and 8 V .

Carrier mobility is one of the most important electronic properties of the synthesized MoS₂ films, as stated earlier. This helps compare with literature data and state-of-the-art performance and is required in electronic device design for modeling and simulations. For example, in designing the MoS₂-based photovoltaic devices discussed in Chapter 4, mobility is one of the most important inputs, and thus it is extremely important that mobility values are known from transistor operation. Transistors are as such the first building blocks in designing optoelectronic devices with these novel materials.

Figure 3.6 shows photogenerated current for a photodetector with a channel length of 10 μm and a channel width of 100 μm . 5 nm of Ti capped with 45 nm of Au is used as source/drain contacts. The incident wavelength is swept between 400 and 800 nm with an interval of 1 nm. The photocurrent is measured for 3 different source-drain voltages, $V_{DS} = 0\text{ V}, 1\text{ V},$ and 5 V . Spectral photocurrent was measured under illumination from a

supercontinuum light source using a laser line tunable filter to scan the wavelength. Dark current was subtracted from the illuminated current to show true photo-induced current.

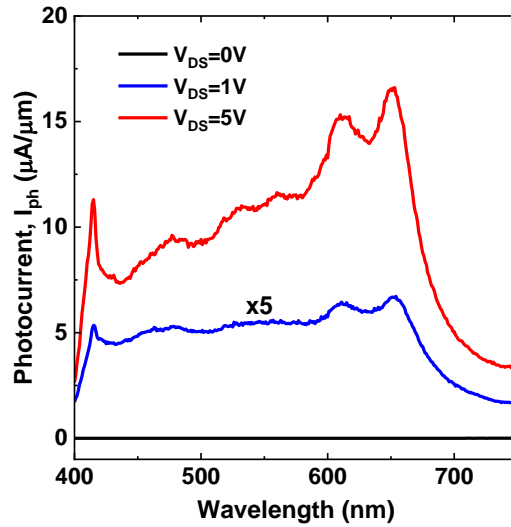


Figure 3.6 Wavelength dependent photocurrent for a monolayer MoS_2 -based transistor-type photodetector. Measurements are taken between 400 and 800 nm monochromatic illumination for three different source-drain voltages, $V_{DS}=0\text{ V}$, 1 V , and 5 V .

EQE and photoresponsivity are measured by measuring the incident photon-flux and effective power within the device area. EQE provides an important understanding of the device performance and thus material quality as it shows the response of the device at each individual wavelength vs. the cumulative response over the entire spectral range. Figure 3.7 plots the EQE of the transistor-type photodetector between 400 and 800 nm. It shows a 25% quantum efficiency at 420 nm incident wavelength, measured at a source-drain bias of 5V. Photoresponsivity of the same device is calculated to be 0.09 A/W also at 420 nm incidence for an input power of 0.1 mW.

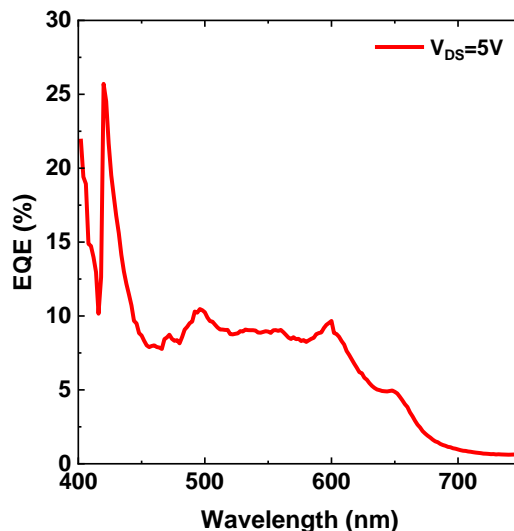


Figure 3.7 External Quantum Efficiency (EQE) of a monolayer MoS₂-based transistor-type photodetector. The measurements were performed between 400 and 800 nm with a source-drain bias of 5V.

The optoelectronic devices show relatively good performance for as-is synthesized MoS₂. We further treat these devices with a chemical called 1,2-Dichloroethane to enhance their optoelectronic performance, as discussed in the next section.

3.4 Chemical Treatments for Enhanced Performance

Chemical-based treatments are performed to improve the performance of as-fabricated devices. In particular, 1,2-dichloroethane (DCE) is used to treat the FET-type photodetectors, as previously demonstrated by Yang et al.⁷⁴. The monolayer MoS₂ devices were soaked in the DCE solution for 4 hours at 60 °C. Results show an increase in the photocurrent response of the devices. The advantages of this method are that it is non-destructive to the metal contacts (hence devices can be treated post-fabrication), it does not require transfer from the substrate, and also, it is applicable for CVD-grown wafer-scale MoS₂ devices.

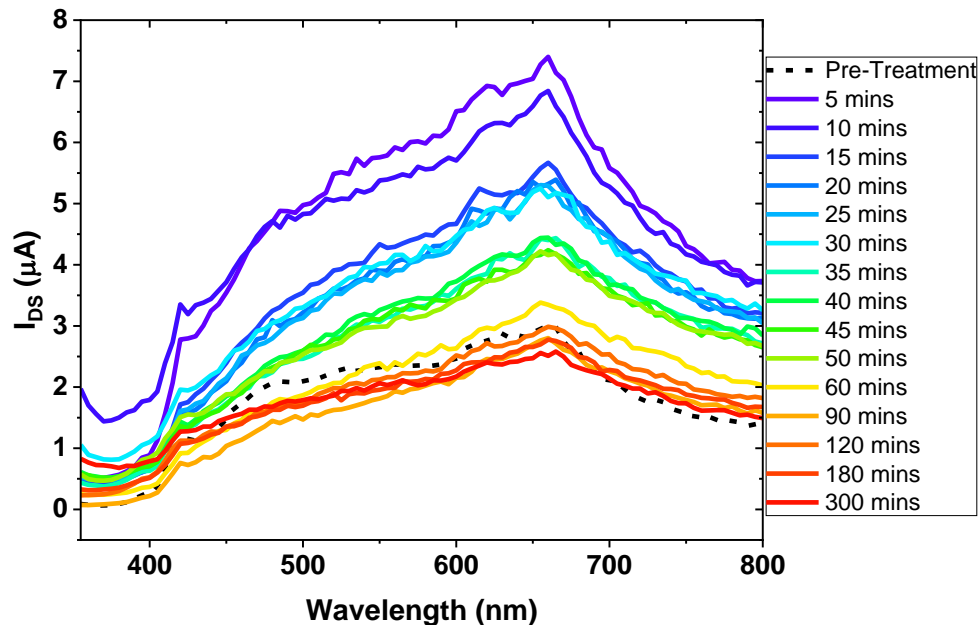


Figure 3.8 Photocurrent of a photodetector before and after DCE treatment. The photocurrents were measured at regular time intervals post DCE treatment to study the time-dependent decay. Measurements were performed under 5V source-drain bias.

Photocurrent was measured before and immediately after the DCE treatment, revealing a $\sim 25\times$ photocurrent increase at the 420nm C-peak and a $\sim 2.5\times$ enhancement throughout the rest of the visible spectrum, as can be seen in Figure 3.8 and 3.9. Dark current was subtracted from the photocurrent in each measurements to show the true photo-generated current. However, the enhancement degraded over time when exposed to ambient air, and subsequent measurements in a regular time interval show a gradual decrease in the photocurrent that follows an exponential decay, as shown in Figure 3.9. The enhanced photocurrent at shorter wavelengths is retained even after 2 hours of exposure to the ambient environment, while at longer wavelengths, the enhancement decays to \sim pre-treatment levels within ~ 1 hour of exposure.

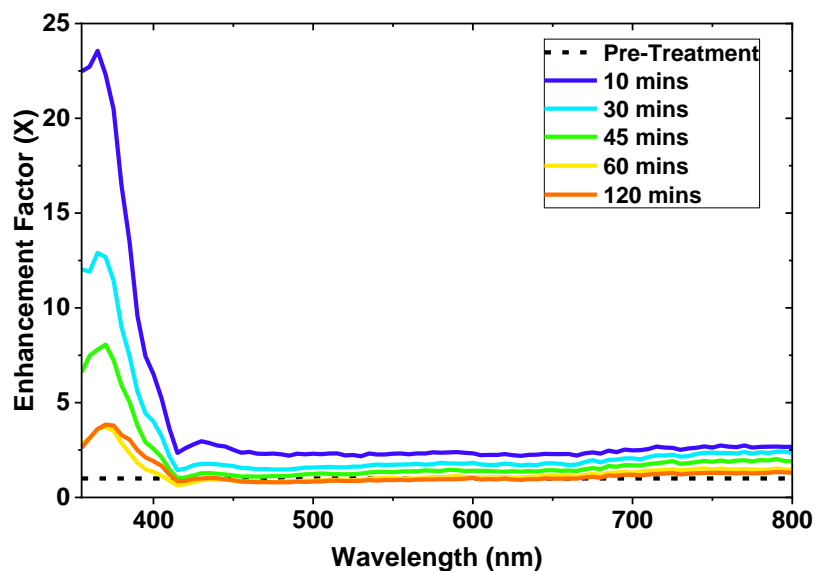


Figure 3.9 Enhancement in photocurrent followed by DCE treatment. The enhancement factor is calculated by dividing the post-treatment photocurrents by the pre-treatment reference photocurrent at each wavelength.

The improvement in the performance is attributed to chlorine atoms from the DCE solution substituting for sulfur vacancies in the MoS₂, thus reducing defects in the material. We hypothesize that the enhanced photocurrent is caused by a combination of reduced contact resistance between the metal contacts and the semiconductor, improved n-dopant concentration in the MoS₂ layer, and the passivation of dangling bonds to reduce Shockley-Reed-Hall (SRH) recombination. The interplay of these three components will inform the implementation of this treatment in optoelectronic device applications. The better enhancement at shorter wavelengths could possibly be coming from reduced surface recombination velocity where the higher energy photons are absorbed. It may also be possible to attribute this short wavelength enhancement to changes in the band structure of MoS₂ due to the introduction of the chlorine atoms.

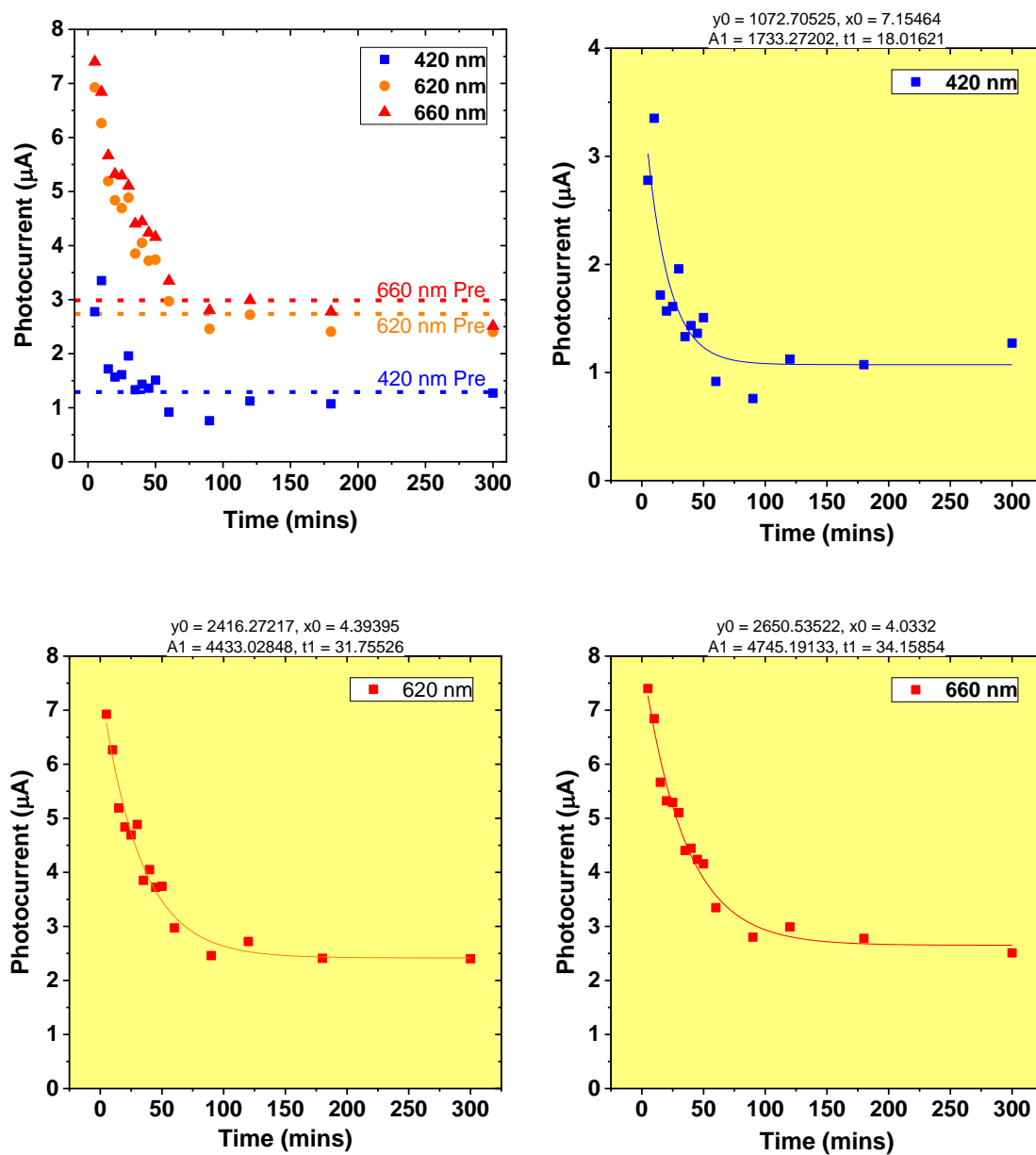


Figure 3.10 Spectral photocurrent measured at regular time intervals post-DCE treatment at monochromatic wavelengths of 420, 620, and 660 nm; these wavelengths roughly correspond to the excitonic A, B, and C peaks of monolayer MoS_2 . All measurements were performed under a 5V source-drain bias.

Figure 3.9 shows the spectral photocurrent measured at regular time intervals post-DCE treatment at monochromatic wavelengths of 420, 620, and 660 nm; these wavelengths roughly corresponds to the excitonic A, B, and C peaks of monolayer MoS₂. All measurements were performed under a 5V source-drain bias and dark current was subtracted from the illuminated current to only account for photogenerated transport.

The measurements show that the photocurrents exponentially decay with time to the ~pre-treatment level within the 1st hour of exposure to the ambient air for all three wavelengths. The exponential decay rate most likely indicates fast evaporation of chlorine in the air when exposed. This study should be particularly helpful in designing experiments for the retention of these enhancements.

3.5 Conclusions and Future Work

In this chapter, we discussed the development and analysis of basic electronic and optoelectronic devices, such as transistors and photodetectors, fabricated with 2D MoS₂ and symmetric of Ti/Au contacts for both source and drain. The eventual goal of this project is to make atomically thin photovoltaic devices with 2D materials. To that end, the work presented in this chapter essentially lays the groundwork.

There are several fundamental questions that this chapter answers to help reach that point. For example, we extract mobility here to understand the electronic transport quality of the synthesized MoS₂ films. Furthermore, the EQE measurements combine the optical and the electronic transport efficiencies at each wavelength by taking into account the absorption, electron-hole pair generation, and collection of the carriers in the external circuit. For a photodetector, this is calculated by taking the ratio of electrons out over photons in, and

the same is applicable for photovoltaic devices, even though their operation and applications are different. The first part of this chapter presents figure-of-merits for the overall material quality and device designs and acts as a guide for the photovoltaic devices discussed in the next chapter. The same approach very well can be taken for designing 2D MoS₂-based photoemitters.

The second part of this chapter focuses on the improvement of the optoelectronic performance of photodetectors via chemical treatment. DCE is shown to be effective in enhancing the photocurrent of a photodetector; however, when exposed to the ambient air, the enhancement quickly decays back to ~pre-treatment levels. There's much room for future work on this end. An effective encapsulation of the devices right after the chemical treatment will be significant.

Future work on the DCE treatment includes but not limited to the following steps to better understand and lock-in the impact of the treatment: measuring contact resistance before and after treatment using the transfer-length matrix (TLM) method; measuring doping concentration before and after treatments; measuring carrier lifetime & defect density in the material; optimizing the DCE soaking duration and soaking temperature; studying degradation over time; and most importantly, coming up with an effective encapsulant to retain the enhancement.

To that end, some preliminary work has been performed. Fabricated photodetectors with extended contacts have been chemically treated with DCE inside a glovebox and then encapsulated with PDMS. The PDMS is cured inside the glove box before exposing it to air. Initial device characterization shows promising results, although PDMS doesn't bond

well with MoS₂ and as such peels off of the MoS₂ surface with minimal contact. This is not surprising, as these 2D materials have very weak out-of-plane bonds to their substrate, and so further studies are needed for finding an effective encapsulation to retain these optoelectronic enhancements.

Methods

Device Fabrication. Device patterns were created using a RAITH Voyager 100 electron beam lithography system. Metal contacts were deposited in an Angstrom Engineering Nexdep electron-beam evaporator tool.

Characterization. Electronic transport measurements were performed by a LabView program using Keithley 2450 and 2460 sourcemeters. Photocurrent measurements were made using a Fianium (now NKT Photonics) super-continuum laser and Photon, Etc. laser line tunable filters (LLTF) for selecting monochromatic wavelengths; this combination is capable of emitting light from 390 nm to beyond 2400 nm in wavelength.

4 LARGE-AREA, MONOLAYER MoS₂-BASED SCHOTTKY-JUNCTION PHOTOVOLTAICS

The strong light-matter interaction in 2D TMDCs such as MoS₂ results in a very high absorptance and photogeneration in these materials, making them suitable materials for flexible and transparent photovoltaics⁷⁵⁻⁷⁷. In this chapter, we present a Schottky-junction photovoltaic device using large-area 2D MoS₂ with lateral (in-plane) current flow and asymmetric contacts.

As Bernardi et al. predicted back in 2013, sub-nm thick 2D TMDC materials can achieve one order of magnitude higher sunlight absorption per unit thickness than GaAs and Si, and thus can achieve 1-3 orders of magnitude higher power densities than the best existing ultrathin solar cells. These properties make the potential for 2D photovoltaics enormous¹³. Jariwala et al. also predicted in 2017 in their perspective article that monolayer TMDC based photovoltaic cells can achieve a maximum of 27% power conversion efficiency using the detailed balance theory⁷⁸. However, to date, the power conversion efficiency in all-2D photovoltaic devices has been under ~5%.

Open-circuit voltage (V_{OC}) is a critical parameter for PV that gives insight into device quality and performance potential. Fontana et al. demonstrated Schottky-junction

photovoltaics with exfoliated ~50 nm thick MoS₂ and Pd and Au contacts and achieved a V_{OC} of 0.1 V⁷⁹. Choi et al. demonstrated a lateral Schottky-junction device with Pd and Cr/Au contacts and exfoliated multilayer MoS₂; their device as-is showed a V_{OC} of 0.08 V; however, with AuCl₃ doping, they were able to improve the V_{OC} to 0.2 V⁸⁰. Wi et al. also utilized multilayer exfoliated MoS₂ to demonstrate a plasma-induced p-doping: a p-n junction photovoltaic device with a V_{OC} of 0.13 V and power conversion efficiency of 0.34% as-is was treated with CHF₃ treatment, resulting in improvement of these values to 0.28 V and 2.8%, respectively⁸¹. Cora et al. demonstrated a vertical Schottky-junction PV device with exfoliated 16 nm WS₂ and asymmetric Au and Ag contacts to achieve 0.256 V of V_{OC} and a power conversion efficiency of 0.46% under AM1.5G solar spectrum⁸². In this work, we demonstrate a lateral Schottky-junction photovoltaic device with CVD-grown monolayer MoS₂ and Au/Ti and Pt contacts. This is one of the first works to report 2D PV device performance using large-area, scalable 2D material synthesis.

4.1 Device Structure and Fabrication

Two different structures of lateral photovoltaic devices have been fabricated and characterized. The first set of photovoltaic devices is very similar in design to the transistors and photodetectors discussed in Chapter 3, except that these photovoltaic devices use asymmetric contacts for carrier (electron and hole) separation instead of having symmetric contacts for both source and drain. Figure 4.1 shows the schematic of a Schottky-junction photovoltaic device with asymmetric contacts on 2D MoS₂. Note the difference in color for source and drain, indicating metals of different work functions. This is useful for forming the Schottky-barrier and achieving carrier separation with no applied

source-drain bias. The main difference between this work and the transistors and photodetectors shown in Figure 3.1 And 3.2 is that these use asymmetric contacts, which requires extra steps in fabrication for alignment lithography and two steps of metal deposition. The details of this fabrication process are described in Appendix A.

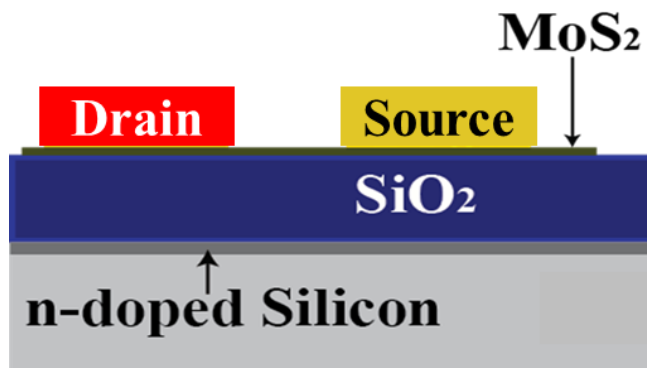


Figure 4.1 Schematic of a Schottky-junction photovoltaic device with asymmetric contacts on 2D MoS₂. Note the difference in color for source and drain, indicating metals of different work functions.

Considering the similarities in the device architectures, these devices have been carefully designed to demonstrate an all-in-one architecture. Figure 4.2 shows the top-view design of such an architecture. The left two contact pads represent symmetric contacts for both source and drain. By contacting the left two symmetric contact pads, the device can be operated as a transistor (with an external gate bias) or as a photodetector; alternatively, the right two asymmetric contact pads can be probed to use this as a photovoltaic device. The asymmetric contact device can also be operated as a photo emitter if the underlying active materials have good radiative efficiency. Depending on which contacts are probed and how the device is biased, the same device thus can be operated as a transistor, photodetector, photovoltaic, or photo emitter. This design is further modified, as shown later in this

chapter, to make multiple devices within a small area using the same all-in-one concept. That all being said, in this chapter, the main focus will be the asymmetric contact photovoltaic devices.

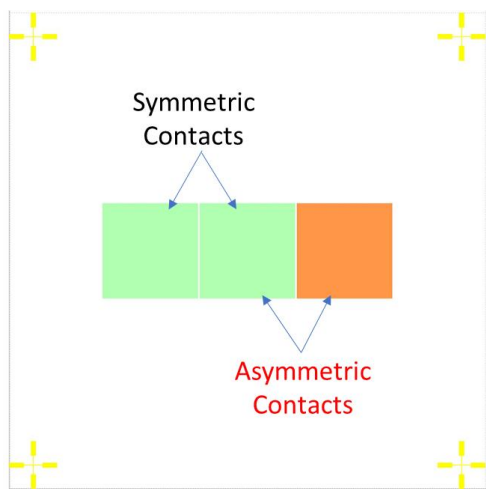


Figure 4.2 An all-in-one optoelectronic device architecture. By contacting the left two symmetric contact pads, the device can be operated as a transistor (with an external gate contact) or photodetector; the right two asymmetric contact pads can be probed to use this as a photovoltaic device.

In the second device design, conventional grid finger and busbar type solar cells are designed with two metal contacts laterally interlocking each other on top or under a sheet of monolayer MoS₂. Details of this device geometry and fabrication process are shown in Appendix A.

Schottky-junction photovoltaics are fundamentally different from traditional solar cells in terms of how their built-in voltage is formed; in a conventional solar cell, a p-type and a n-type semiconductor material are brought together to form what is known as a p-n junction. Due to the offsets in the p-type and n-type materials' Fermi levels, a built-in potential difference is created, which results in electron-hole pair carrier separation. In a Schottky-

junction solar cell, however, the built-in voltage is formed by the offset between the Fermi levels of the semiconductor and the metal contact⁸³. At the interface between the semiconductor and metal, band bending happens due to the said band offsets, and a so-called Schottky barrier drives the carrier separation. Two metal contact materials need to be chosen carefully to design a Schottky-junction photovoltaic device with MoS₂, such that they each align to the conduction or valence band of MoS₂ for electron or hole collection, respectively. For this work, metals with various work functions are studied, as shown in Figure 4.3. Several low work function metals such as Yt, Sc, Mo, and Ti are considered for electron collection, while high work function metals such as Co, Ni, Au, Pd, and Pt are considered for hole collection. In the middle of the plot is shown the band structure of monolayer MoS₂ having a bandgap of 1.85 eV. The criteria for effective carrier separation, i.e., electron and hole collection in two separate contacts, are shown on the right and left.

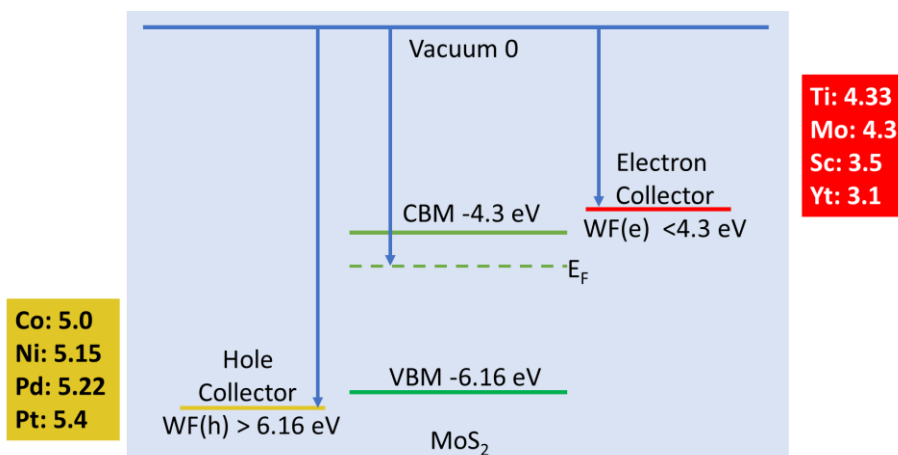


Figure 4.3 Band structure schematic for monolayer MoS₂, showing metal work function requirements for carrier (electron and hole) separation. Possible low and high work function metals are listed on the right and left, respectively.

To create the differing Schottky junctions in our experimental devices, Ti and Pt are initially chosen as the contact metals because of their low (4.33 eV) and high (5.64 eV) work functions and their wide use to-date for contacting 2D MoS₂. These asymmetric contacts create the necessary band offsets at the metal-MoS₂ interface between the Fermi levels of these metals and that of MoS₂, thus driving the electrons toward Ti and holes toward Pt and separating the photo-generated carriers without any applied bias.

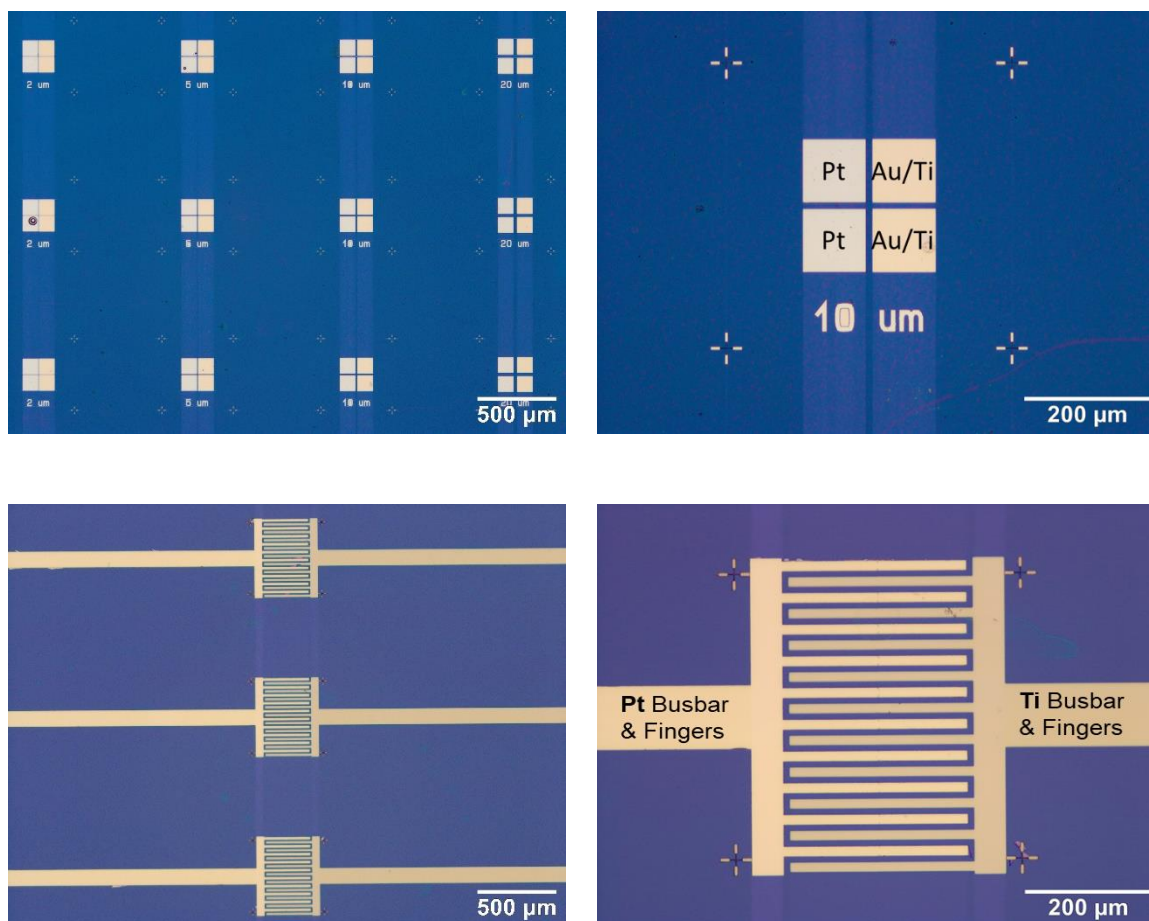


Figure 4.4 fabricated asymmetric contact Schottky-junction solar cells with Ti and Pt contacts. The top row shows the all-in-one symmetric and anti-symmetric device architecture, while the bottom row shows more traditional finger-busbar type solar cells.

Figure 4.4 shows the fabricated asymmetric contact Schottky-junction solar cells with Ti and Pt contacts. The top row shows the all-in-one architecture, while the bottom row shows the traditional finger-busbar type solar cells. In the top row contact-pad devices, the contacts were deposited on top of MoS₂. The channel length and width here are 10 μm and 100 μm , respectively. In the finger-busbar type devices, the contacts were first deposited on SiO₂-on-Si substrates and monolayer MoS₂ was transferred on top. The interlocking fingers are 15 μm wide with 10 μm channels between them. Devices were fabricated in arrays to generate more measurable devices for the same film, enabling measurements with statistical significance.

4.2 Photovoltaic Performance

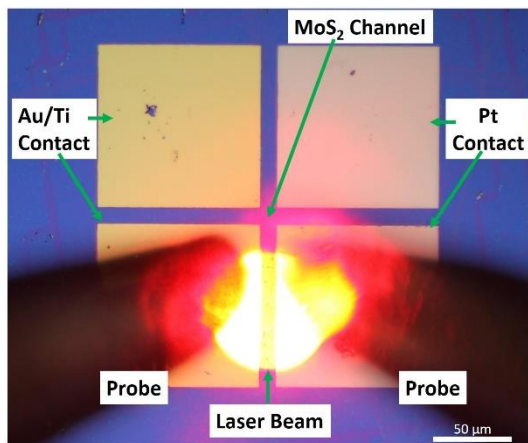


Figure 4.5 An illuminated asymmetric contact Schottky-junction solar cell with 2D MoS₂. The laser excitation wavelength is 660 nm.

Devices were characterized for open-circuit voltage (V_{OC}), short-circuit current (I_{SC}) and short-circuit current density (J_{SC}), power conversion efficiency (η), fill-factor, series resistance (R_S), and shunt resistance (R_{SH}), all at room temperature. The devices were illuminated by monochromatic laser excitation with high concentration and standard one-

sun AM1.5G in a solar simulator. Figure 4.5 shows an illuminated solar cell in the all-in-one architecture with an excitation wavelength of 660 nm. The laser power is swept to study the current-voltage relationships at different intensity of the input irradiance.

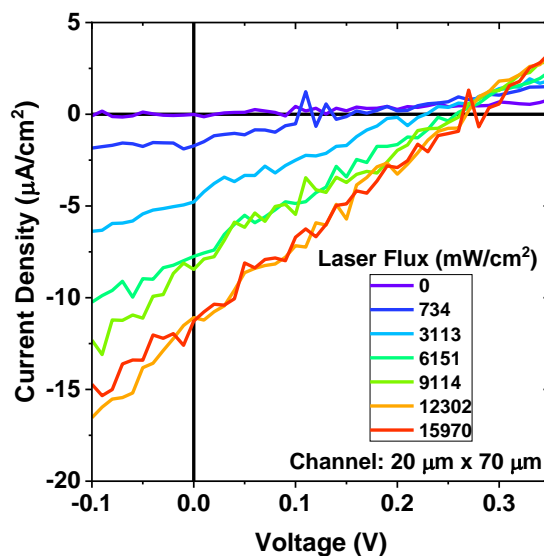


Figure 4.6 J-V plot of a Schottky-junction MoS_2 solar cell with 660 nm laser excitation, as shown in Figure 4.5. The laser flux was varied with a maximum of 15.97 W/cm^2 flux.

Figure 4.6 shows the J-V plot of the solar cell shown in Figure 4.5. The monochromatic 660 nm laser excitation was swept up to 15.97 W/cm^2 photon flux. The solar cell shows a V_{OC} of 160 mV and a J_{SC} of 2 $\mu\text{A}/\text{cm}^2$ at 0.73 W/cm^2 illumination. At 15.97 W/cm^2 flux, the V_{OC} and J_{SC} are recorded as 270 mV and 11.5 $\mu\text{A}/\text{cm}^2$, respectively.

Figure 4.7 shows a finger-busbar type solar cell's photovoltaic performance for monochromatic and standard 1-sun AM1.5D illumination conditions. As shown, the V_{OC} and J_{SC} are recorded as 260 mV and 1.07 $\mu\text{A}/\text{cm}^2$, respectively, at ~8 sun equivalent illumination with 660 nm excitation laser. Under 1-sun AM1.5D illumination in a solar simulator, the V_{OC} and J_{SC} reduces to 110 mV and 0.18 $\mu\text{A}/\text{cm}^2$, respectively,

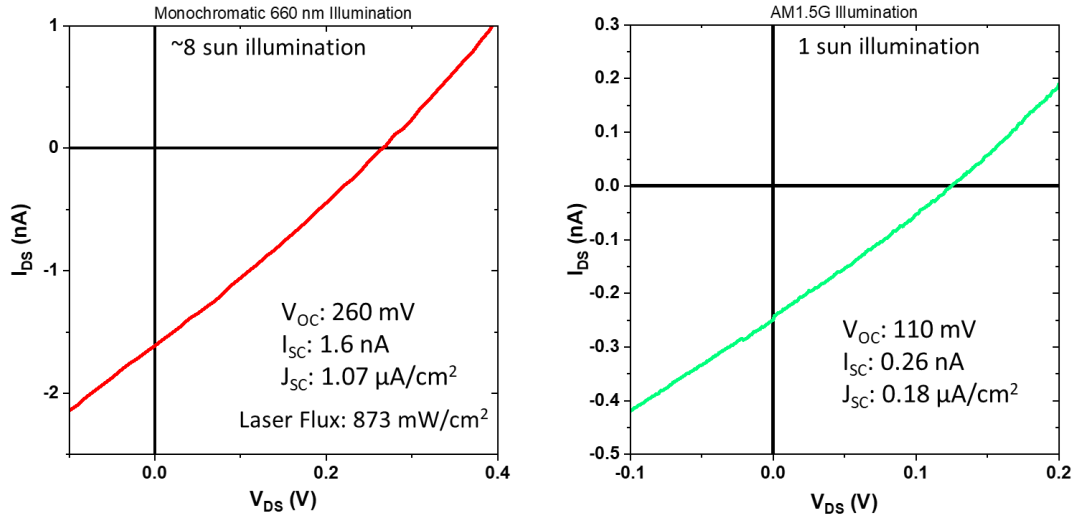


Figure 4.7 J-V plot of a finger-busbar type Schottky-junction MoS₂ solar cell with monochromatic 660 nm laser excitation and 1-sun equivalent AM1.5G illumination.

From the 1-sun I-V plots, the following solar cell figures-of-merit are extracted to understand the overall 1-sun performance better. The efficiency, fill-factor, series and shunt resistances are calculated using previously published methods^{84,85}.

Table 4.1 Figures-of-merit for the finger-busbar type asymmetric contact Schottky-junction MoS₂-based solar cell under 1-sun AM1.5G illumination

V _{MP} (V)	0.05
I _{MP} (mA)	1.32E-07
V _{OC} (V)	0.11
I _{SC} (mA)	2.64E-07
J _{SC} (mA/cm ²)	1.76E-04
Fill-Factor (%)	22.72%
Efficiency, η (%)	0.0000044%
R _S (ohm.cm ²)	147875
R _{SH} (ohm.cm ²)	656610

The figure-of-merit values are not very high, but these are some of the first all-2D solar cells made with CVD-grown monolayer MoS₂ films. However, the V_{OC} value is particularly high for CVD-grown monolayer MoS₂. Cho et al. fabricated a WSe₂/MoS₂ heterojunction with *exfoliated* 5 to 10 layers of WSe₂ and MoS₂ each and achieved a V_{OC} of 0.36 V under 1-sun illumination without any passivation⁸⁶. We have not found any report of CVD-grown monolayer MoS₂-based photovoltaics characterized under 1-sun illumination to compare our results with and believe our result is the first ever large-area 2D PV device. Several analyses are performed to better understand the device performance, including EQE and IQE measurements and resistance measurements.

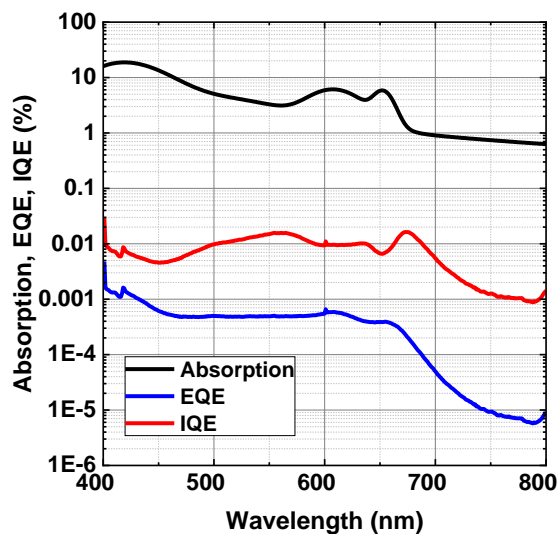


Figure 4.8 Absorption, EQE, and IQE of the finger-busbar type Schottky-junction MoS₂-based solar cell.

Figure 4.8 shows the Absorption, EQE, and IQE vs. wavelength for the finger-busbar type solar cell. The EQE corresponds to the ratio of electrons out to photons in, whereas the IQE is calculated by taking the ratio of electrons out to photons absorbed. Thus, the IQE is a measure of the electronic efficiency of the material/device alone, while the EQE accounts

for both electronic and optical efficiencies. As the monolayer MoS₂ absorbs ~3-20% of the incoming light above its optical bandgap energy of 1.8 eV, the optical performance is quite good as-is given the atomic thicknesses. The electronic performance is where it lacks severely. The low IQE across the spectrum clearly shows that the device has insufficient electronic transport by about 3 to 4 orders of magnitude.

To understand the limitations in electronic transport, the solar cell is divided into a resistance network consisting of the probes, the contacts pads, the fingers and the busbars, the contact resistance at the metal-semiconductor interface, and the sheet resistance. The total resistance from the fingers and busbars came to be 225 Ω , showing that the bulk of the resistance comes from the contact and sheet resistance. To extract these values, the transfer length method (TLM) is used⁸⁷. Figure 4.9 shows a TLM grid on monolayer MoS₂ with variable channel lengths from 1 μm and 150 μm . These measurements are performed with both Ti/Au contacts and Pt contacts.

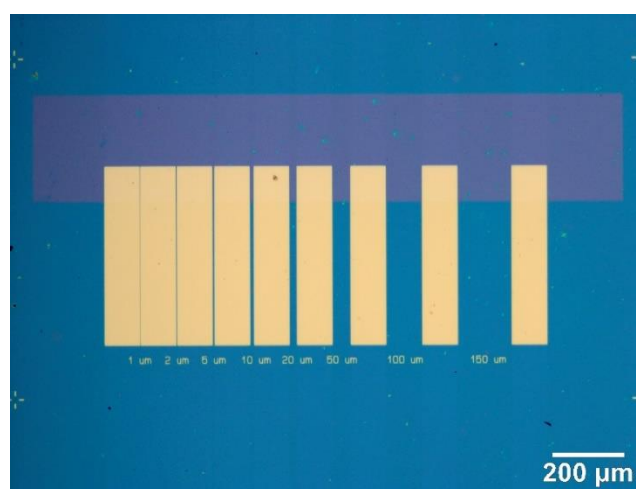


Figure 4.9 A TLM grid pattern on monolayer MoS₂ with variable channel lengths from 1 μm to 150 μm . These structures are used to extract the contact resistivity at the metal-semiconductor interface and the sheet resistivity of the semiconducting material.

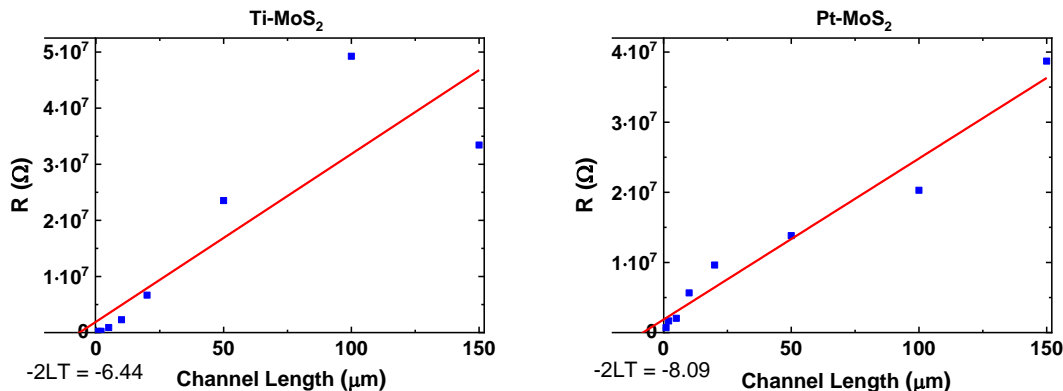


Figure 4.10 TLM plots for Ti-MoS₂ and Pt-MoS₂ devices. The resistances are plotted for various channel lengths. Contact resistance is extracted from the y-axis intercept of the linear fit (divided by 2) and the sheet resistance is calculated by taking the slope of the linear fit line and dividing it by the channel width.

By analyzing the data shown in Figure 4.10, the average contact resistivity of the Pt-MoS₂ and Ti-MoS₂ interface is calculated to be 45.33 Ω.cm² and 17.5 Ω.cm², respectively. The average sheet resistivity is estimated to be 2.34 x 10⁸ Ω/□. The high contact and sheet resistivity in these devices contribute significantly to their poor electronic transport performance. In comparison, contact resistance is typically in the 10⁻⁶ Ω.cm² range for a good solar cell^{88,89}. Also, sheet resistance needs to be sufficiently low for lateral transport, preferable in the 50-100 Ω/□ range⁹⁰.

A spatial photocurrent map is also generated by selectively illuminating part of the device spatially and recording the photogenerated current at each location. Figure 4.11 shows such a photocurrent map. The map shows that the photocurrent is higher only when the illumination is close to the Pt contact. The likely cause for this is that the photogenerated carriers recombine before they can make it to the contacts if they are too far away, indicating low lateral diffusion length of the carriers. Also, the lateral diffusion length for

electrons is much higher compared to that of the holes. Thus an electron generated further away from the Ti contact can make its way to the contact, whereas any holes generated far from the Pt contact recombine before they can be collected. We believe this is why we only see photocurrent near the Pt contact.

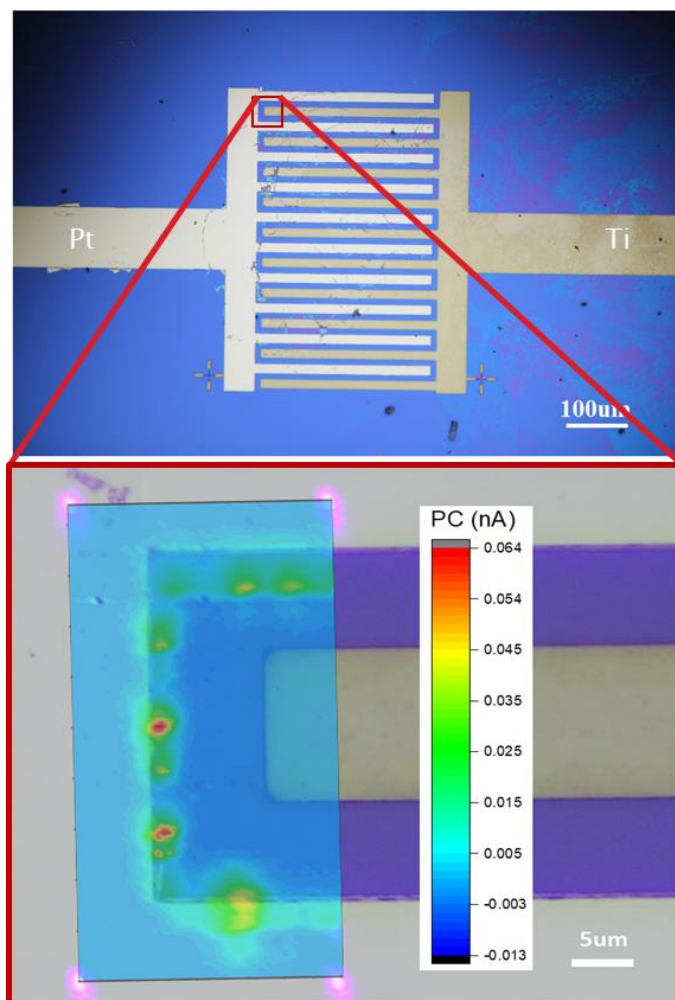


Figure 4.11 Spatial photocurrent map of a Schottky-junction MoS₂-based solar cell, showing photogeneration and collection mostly near the Pt contacts.

A COMSOL multiphysics-based model is generated to further understand the device performance and help guide future device designs.

4.3 Optoelectronic Device Model

A 1D finite element analysis device model is built using the COMSOL Multiphysics simulation tool's Semiconductor Module. This model simulates a MoS₂-based solar cell device with a 10 μm channel in between asymmetric Ti and Pt contacts, as shown in Figure 4.12.

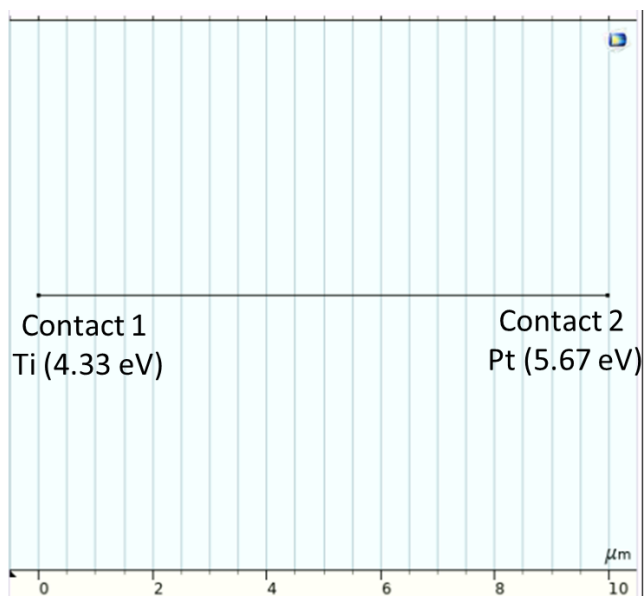


Figure 4.12 Schematic of a MoS₂-based solar cell with 10 μm channel in between asymmetric Ti and Pt contacts, generated in the COMSOL Multiphysics software.

The model uses a homogenous doping in the active MoS₂ material by using the Analytical Doping Model built in to COMSOL. Eq. 4.1 is used to calculate photogeneration that includes the solar irradiance and MoS₂ absorption spectra. The absorption spectra is calculated in Eq. 4.2 by using the extinction coefficient of monolayer MoS₂ (discussed in Chapter 2). The Shockley-Read-Hall recombination model is implemented in a Trap-

Assisted Recombination feature, also built in to the COMSOL tool. Eq. 4.3 shows the photon flux that is used to calculate the photogeneration.

$$G = \int_0^{\infty} \alpha(\lambda) \varphi(\lambda) \exp(-\alpha(\lambda)z) d\lambda \quad 4.1$$

$$\alpha(\lambda) = \frac{4\pi\kappa(\alpha(\lambda))}{\lambda} \quad 4.2$$

$$\varphi(\lambda) = \frac{\lambda}{hc} F(\lambda) \quad 4.3$$

Here, z is the depth into the device, λ is the wavelength in vacuum, $\kappa(\lambda)$ is the wavelength-dependent extinction coefficient, and $F(\lambda)$ denotes the AM1.5G spectral irradiance. With 100% IQE, i.e., all the electron-hole pairs that are generated are collected, a maximum of 1.34 mA/cm^2 J_{SC} is estimated for monolayer MoS_2 -based solar cells.

To account for the lateral junction where the solar cell is illuminated from the top, the photogeneration is assumed to be homogeneous between the contacts with a monolayer MoS_2 thickness of 0.65 nm. Here, the photogeneration occurs in the z -direction while the electronic transport happens in the x -direction in the 1D lateral PV model. The cross-sectional area considered for device simulation is the area encompassing the thickness of the material times the width of the channel, 0.65 nm and 100 μm , respectively. For J_{SC} calculations, a different area is used; the area is given by the length and width of the channel; in this case, 10 μm and 100 μm , respectively. The model uses several user-defined parameters such as mobility ($3.3 \text{ cm}^2\text{V}^{-1}\text{s}^{-1}$, extracted from experimental measurements), a doping concentration of $1 \times 10^{16} \text{ cm}^{-3}$ ⁹¹, bandgap of monolayer MoS_2 as 1.85 eV ⁶, electron affinity of 4.5 eV ⁹², relative permittivity of 4.2 ⁹³, and an electron lifetime of 611 ns⁹⁴.

The model calculates the energy bandstructure diagram of the device, as shown in Figure 4.13. The band bending between MoS₂ and the contact metals is demonstrated here. On the left side is the Ti contact with 4.3 eV work function that aligns well with the conduction band of MoS₂; hence an ~ohmic contact forms at this metal-semiconductor junction. On the right side, Pt forms a large Schottky-barrier, as evident by the large band-bending, which is essential for the carrier separation but also negatively impacts the electronic transport. This large band-bending is one of the reasons for the low measured electronic transport in the device.

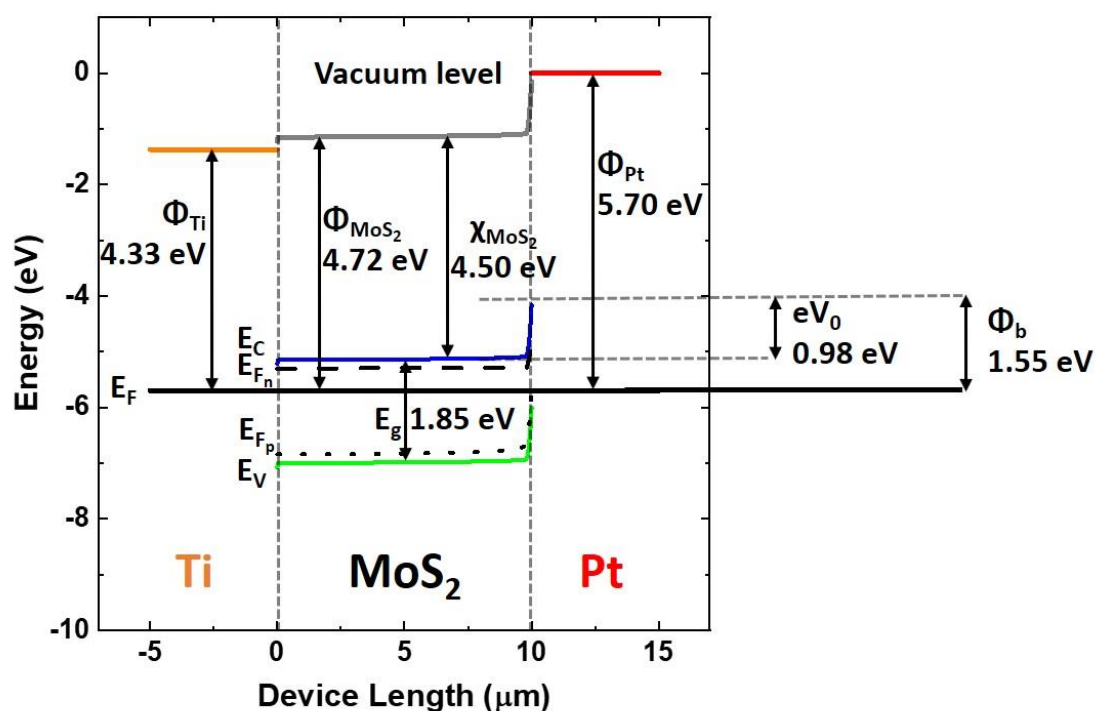


Figure 4.13 Band structure of a Ti-MoS₂-Pt Schottky-junction solar cell showing the asymmetric band bending at the metal-semiconductor interfaces. The larger bend on the right side between MoS₂ and Pt indicates a large Schottky barrier.

Once the model is established, the current-voltage relationship of the device is studied under forward bias. Figure 4.14 shows the simulated I-V plot using the parameters listed above. The model predicts a V_{OC} of 900 mV and a J_{SC} of $4.2 \mu\text{A}/\text{cm}^2$.

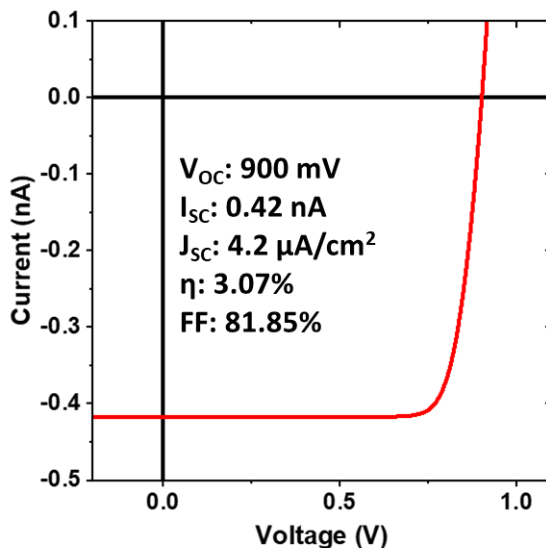


Figure 4.14 Simulated I-V curve of a monolayer MoS₂-based solar cell with asymmetric Ti-Pt contacts under AM1.5G solar irradiance.

The mismatch between the model and experiment V_{OC} comes in part from work function mismatch. While the model assumes literature values for Ti and Pt work functions, each deposition condition is different, and as such, it warrants a direct work function measurement of our deposited metal contacts. Such measurements are currently underway. Also, the low J_{SC} affects the V_{OC} as well and further lowers it.

The modeled J_{SC} can be matched with the experimental J_{SC} by tuning the parameters in the model. For example, changing the mobility and the doping concentration by one order of magnitude each brings down the modeled J_{SC} to within very close proximity to the experimental J_{SC} .

This semiconductor device physics model is critical to understanding 2D PV device performance. More importantly, it should help design future photovoltaic devices with 2D materials with significantly enhanced performance for real-world impact.

4.4 Conclusion

In summary, this chapter presents the design, modeling, fabrication, and characterization of monolayer MoS₂-based Schottky-junction photovoltaic devices with asymmetric Ti and Pt contacts. Two different architectures of devices were fabricated and characterized.

Devices with asymmetric contact pads similar to transistors and photodetectors were characterized under monochromatic laser illumination. V_{OC} of 270 mV was recorded, which is better than previously reported values for monolayer TMDC based Schottky-junction photovoltaics. Finger-busbar type solar cells were also fabricated and characterized under monochromatic laser and 1-sun illumination. The measured V_{OC} of 110 mV under 1-sun illumination is one of the highest recorded V_{OC} 's for 2D TMDC based Schottky-junction solar cells. The devices suffer from low current density as a result of poor electronic transport in the material and into the contacts.

4.5 Future Work

There is a lot room of room for improvement in 2D photovoltaic device design and fabrication. To begin with, the optical absorption can be further enhanced by applying optical coatings to the front as outlined in Chapter 2, or a back reflector can also be used as the back contact for vertical solar cells. Effective light trapping mechanisms need to be integrated into the device structures, including nanostructures that can be utilized for

enhanced photon capture. Passivating surface treatments such as the DCE treatment shown in Chapter 3 can significantly improve the carrier transport and thus the overall performance of a photovoltaic device.

Contact engineering is a big part of the device design, and with optimized contacts, the V_{OC} and J_{SC} of the Schottky-junction solar cells can be improved substantially. Knowing the exact work function of a metal is a key piece in this puzzle, as that would allow us to model the devices accurately. Choosing from a number of metals with varying work functions as shown in Figure 4.3 will enable us to design the devices such that the Schottky-barrier height is just large enough for carrier separation but at the same time does not limit the carrier flow significantly.

Large-area devices with contact patterns also need to be carefully designed. For the finger-busbar type devices, the fingers' pitch and width need to be optimized for minimum shadowing (applicable for the top contact, if any), to prevent leakage, and to maximize the photogenerated carriers' collection.

Another short-term goal could be designing 2D photovoltaics with thicker 2D films. For example, assuming 100% IQE, a photovoltaic device made with tri-layer MoS_2 generates a maximum J_{SC} of 3.23 mA/cm^2 vs. the 1.34 mA/cm^2 from monolayer MoS_2 .

While most discussions thus far have revolved around lateral photovoltaics, vertical Schottky-junction 2D PV should be the penultimate goal before suitable p-n junctions can be fabricated. With vertical Schottky junctions, the devices would not be affected by low lateral transport efficiency. Instead, the carriers will have to diffuse through sub-nm films,

unlocking the 2D films' true potential. The bottom contact can also be used as a reflecting back, which will further increase the photogeneration.

Finally, p-n homojunction/heterojunction photovoltaics also hold a lot of potential. If MoS₂ or any other particular TMDC can be effectively doped to be both n-type and p-type, a homojunction photovoltaic device can be fabricated. Another way is to make heterojunction devices, such as WSe₂/MoS₂ or WSe₂/MoSe₂ heterojunctions. There has been some work on that end but with minimum success^{57,95}.

Lastly, all the approaches mentioned above hold the potential for being transferred on to transparent and flexible substrates. 2D materials that are only angstroms thick and absorb only 5-20% of the incoming light can revolutionize the way photovoltaics are made today. Such semi-transparent and/or flexible devices can have widespread applications where optical throughput or high bend-radius are required. And as mentioned at the outset, 2D PV is an excellent candidate for any weight or space constrained PV applications, especially those in space.

5 TRANSMISSIVE ACTIVE COOLING IN A HYBRID SOLAR CONVERTER

This chapter details the development of a hybrid solar converter that consists of an optically transmissive CPV module and a thermal receiver. In particular, we detail the novel design, fabrication, and characterization of a microchannel-based optically transmissive active cooling system for CPV cells that couples the CPV module optically to a thermal receiver directly behind it.

Hybrid spectrum-splitting transmissive CPV/T (tCPV/T) systems use CPV cells to collect high-energy UV and visible light to generate electricity but transmit IR wavelengths for thermal collection. This IR transmission allows the CPV and thermal systems to be thermally decoupled, significantly reducing the thermal load on the CPV portion while enabling simultaneous high-temperature solar thermal collection⁹⁶. This system makes efficient use of the entire solar spectrum by collecting visible and IR light using spectrum-optimized means. Such a transmissive system is also highly tolerant of light spillage around and between CPV cells, unlike in conventional dense array CPV systems, as the spilled light may be captured very efficiently in the thermal receiver. Importantly, high-temperature thermal collection also opens up industrial applications that require process

temperatures from 100 to 450 °C or higher⁹⁷. However, despite the transmission of the infrared wavelengths through the CPV component, high concentrations of solar flux still require a cooling system to allow the CPV system to operate efficiently and to prevent premature degradation. In order to preserve the transmissive nature of the system, the cooling system must also be transmissive and optically compatible with the tCPV/T system.

Tripanagnostopoulos et al. presented a hybrid system with photovoltaic modules and thermal collectors that uses active cooling for extracting heat from the PV module; the extracted heat improves the PV module performance while the thermal energy may be used in several ways⁹⁸. Zakharchenko et al. studied several PV modules, including that of c-Si, a-Si, and CuInSe₂, and their design for efficient heat extraction in a hybrid system⁹⁹. Otanicar et al. published a parametric comparison of different concentrated hybrid solar PV/T configurations and showed that waste heat recovery from PV cells significantly improves performance, with total exergetic efficiencies exceeding 40%¹⁰⁰; a similar parametric study was shown by Rezania et al.¹⁰¹. Looser et al. designed a hybrid system that uses heat transfer fluids in front of the PV cells as a direct absorption filter¹⁰². Mojiri et al. also presented a decoupled spectral-splitting hybrid CPV/T system¹⁰³. In a recent review, Ju et al. exhaustively reviewed the state-of-the-art of PV-CSP hybrid technologies¹⁰⁴. In all cases, it is evident that the high concentration of sunlight in a CPV/T system typically results in very high cell temperature and requires some form of cooling.

To enable active cooling of a tCPV/T system, we present here the design, fabrication, characterization, and on-sun validation of 100 μm thick transmissive microchannels

capable of maintaining the temperatures of a dense array of CPV cells below 110 °C for fluxes up to 300 suns. This is the first demonstration of an optically transmissive active cooling system, with potential applications beyond CPV/T, including optoelectronics, photocatalysis, and more.

5.1 System Overview

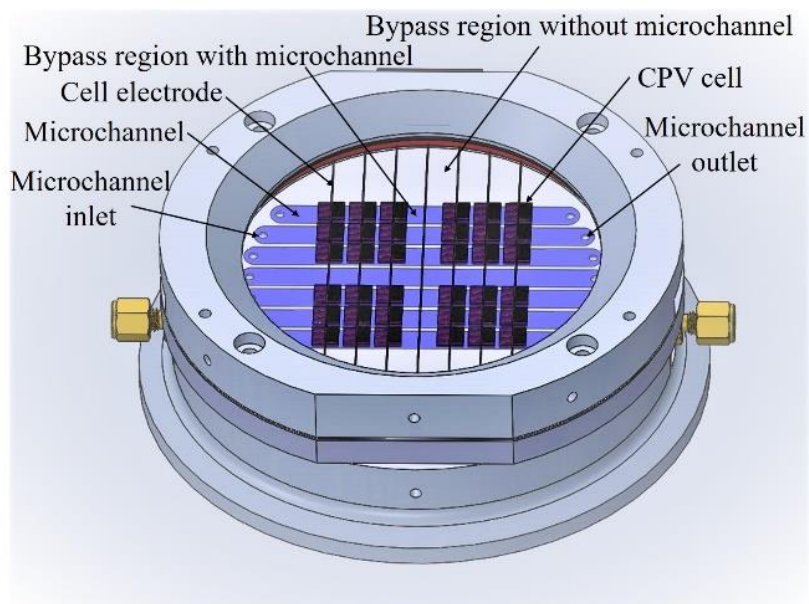


Figure 5.1 CAD drawing of the transmissive CPV module; the transmissive active cooling microchannels are highlighted.

The transmissive CPV module consists of thirty-six 5.5 x 5.5 mm high-efficiency III-V triple-junction solar cells²¹ that are arranged in four quadrants, each having nine cells in a 3x3 array as shown in Figure 5.1. Figure 5.2 shows a schematic cross-section of the CPV module. The cells are encapsulated in Sylgard 184 polydimethylsiloxane (PDMS) between a top quartz and bottom c-axis sapphire window. Sapphire is used as the bottom window for its high thermal conductivity and high transparency. Electrodes for the cells are

embedded within the top and bottom window to minimize the distance between the cells and the sapphire substrate, improving heat transfer to the cooling channels. Below the sapphire layer, seven active cooling microchannels run under each one of the cell rows orthogonal to the cell electrodes. Each microchannel is 5.5 mm wide, 100 μm deep, and runs for the entire length of the module window, as shown in Figure 5.1. The channels are made using PDMS on a transparent bottom quartz window and attached to the underside of the sapphire window. Water is used as the cooling fluid and is pumped into the microchannels using a 12V diaphragm pump in a closed-loop cycle. Heat absorbed in the cells conducts through the sapphire substrate and is carried out to the flowing cooling water. A forced-air radiator is used to reduce the water temperature before it is cycled back in to the microchannels. The high thermal conductivity of sapphire ensures efficient radial heat transfer between cells to minimize hot spots due to varying irradiance distribution and provides a low resistance axial conduction path to the microchannels. A pressure regulator is used to control the inlet manifold pressure to the microchannels, which determines the coolant velocity and flowrate. Thermocouples are embedded in several locations between cells and within the manifold coolant stream for real-time temperature measurements. A top collar and bottom manifold house the CPV cell stack while providing the inlets and outlets for the cooling channels, cell electrodes, and thermocouples.

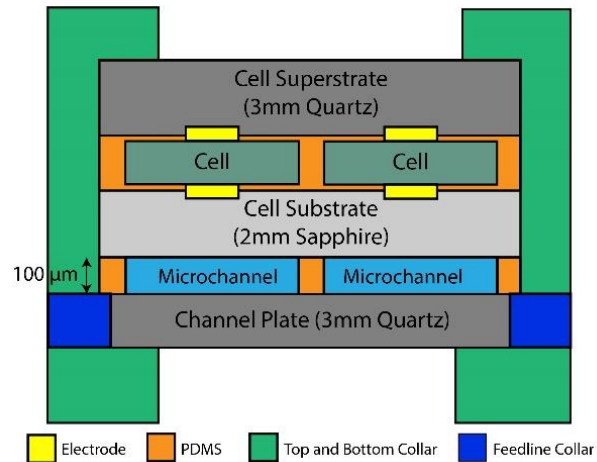


Figure 5.2 Cross-sectional schematic of the CPV module (layers not to scale)

The transmissive microchannels allow low-energy photons that are not absorbed by the solar cells to continue transmitting through the cooling system and ultimately reach a thermal receiver. Depending on working fluids and user needs, the thermal receiver can collect this as process heat at temperatures up to 550 °C⁹⁶.

5.2 Modeling

This section discusses the optical, thermal, and microfluidic models for the transmissive active cooling system.

5.2.1 Optical Model

The transfer-matrix method is used to calculate the reflection, absorption, and transmission in each layer of the spectrum splitting CPV module to determine the overall optical transmission through the module. The thickness of each layer is considerably larger than the range of the wavelength that we are interested in. Assuming a planar plate between

entrance medium and exit medium, the overall transmittance is calculated by summing all components exiting the bottom of the plate, and the cumulative reflectance is obtained from the sum of all parts reflected at the entrance interface¹⁰⁵. The total absorption is then calculated by deducting transmittance and the reflectance from unity. Details on the optical modeling are published by Ji et al.¹⁹.

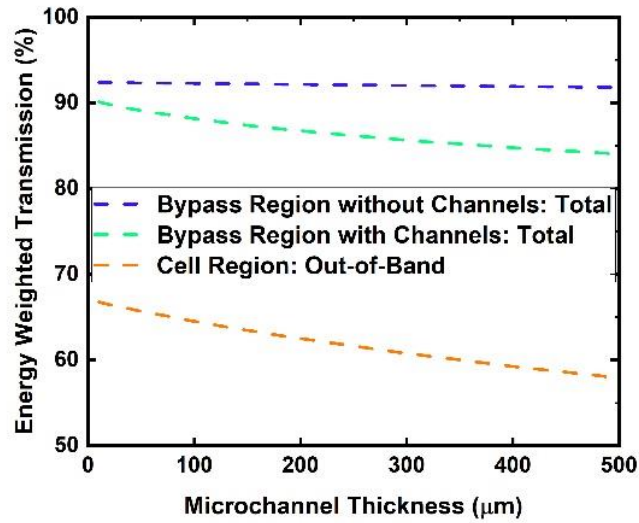


Figure 5.3 Energy weighted module transmission for different microchannels thickness assuming water as the coolant fluid.

Figure 5.3 shows the solar-spectrum-energy-weighted transmission for different microchannel thicknesses. The inband and out-of-band solar-spectrum-energy-weighted transmissions are defined below.

Inband solar-spectrum-energy-weighted transmission:

$$T_{inband} = \frac{\int_{280nm}^{873nm} t(\lambda) D_{AM1.5D}(\lambda) d\lambda}{\int_{280nm}^{873nm} D_{AM1.5D}(\lambda) d\lambda} \quad (5.1)$$

Out-of-band solar-spectrum-energy-weighted transmission:

$$T_{out-of-band} = \frac{\int_{873\text{nm}}^{2500\text{nm}} t(\lambda) D_{AM1.5D}(\lambda) d\lambda}{\int_{873\text{nm}}^{2500\text{nm}} D_{AM1.5D}(\lambda) d\lambda} \quad (5.2)$$

The bypass region is the region of the module aperture window with no cells (see Figure 5.1). Total solar spectrum transmission is plotted for the bypass region with and without microchannels, whereas only the out-of-band transmission is plotted for the cell region, since the cells are designed to absorb light up to 873 nm. The modeled energy weighted transmission for the module with 100 μm thick microchannels is 92.3% (total), 88.2% (total), and 64.5% (out-of-band) for the bypass region without channels, bypass region with channels, and cell region, respectively. The effect of PDMS base layer thickness is also studied as shown in Figure 5.4.

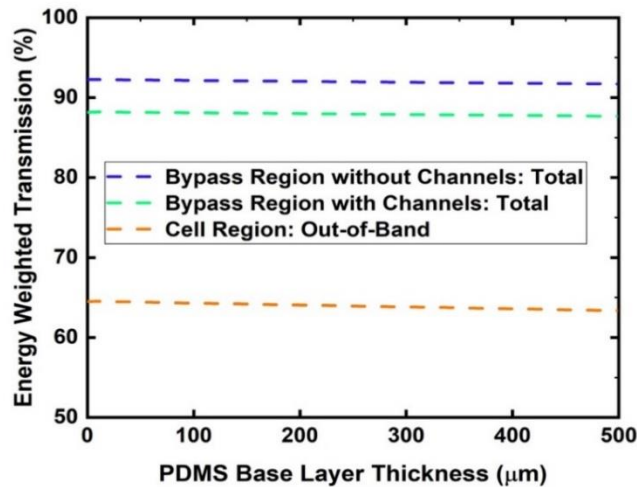


Figure 5.4 Effect of PDMS base layer thickness on the solar-spectrum-energy-weighted transmission of the CPV module.

5.2.2 Thermal Model

Table 5.1 Thermal properties of each component of the CPV⁷⁸. The top, bottom and lateral regions are shown in Figure 5.5.

Top: R = 107 K/W	
PDMS	k = 0.20 W/m-K
Quartz	k = 1.38 W/m-K
Air	h = 1000 W/m ² K
Lateral: R = 1818 K/W	
PDMS	k = 0.20 W/m-K
Cell	Q = 1 to 7 W
Bottom: R = 7 K/W	
PDMS	k = 0.20 W/m-K
Sapphire	k = 27 W/m-K
Water	k = 0.64 W/m-K, Nu = 5.39

Cooling system efficacy was predicted through thermal modeling and optical flux map analysis. Table 5.1 summarizes thermal properties of each component and cumulative thermal resistance¹⁰⁶. Because the heat transfer coefficient through the sapphire to the microchannels is much greater than through the quartz top window or radially to the aluminum collar, the model can be reduced to a 1D heat transfer problem taking the path shown by the arrows in Figure 5.5 (cell-encapsulant-sapphire-cooling channel).

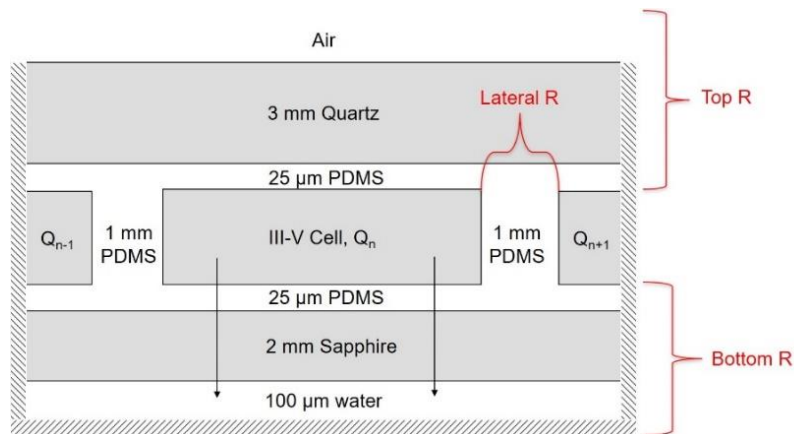


Figure 5.5 Schematic of thermal model geometry with primary heat flow path illustrated.

Figure 5.6 shows the equivalent thermal resistance network for the module. T_{air} , T_{qua} , T_{enc_t} , T_{cell} , T_{enc_b} , T_{sap} , and T_{wat} are the temperatures of the ambient air, top surface of the quartz window, encapsulant on top of the cell, cell, encapsulant at the bottom of the cell, sapphire and the cooling water, respectively. R_{rad} and R_{conv} are thermal resistances for radiation and convection from the top window, while R_{qua} , R_{enc} , R_{sap} , and R_{wat} represents the thermal resistances of the quartz window, encapsulant later, sapphire, and water, respectively.

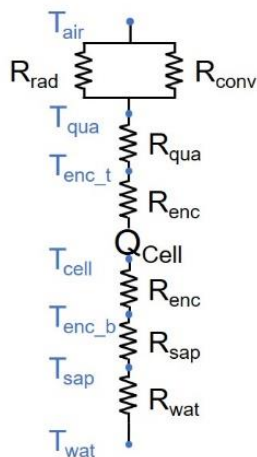


Figure 5.6 Schematic of the equivalent thermal resistance network.

The thickness of the PDMS encapsulant and the sapphire substrate were kept at minimum to ensure maximum heat transfer to the microchannels. Water is chosen as the cooling fluid since it is inexpensive, does not suffer from degradation over time, and has better heat transfer properties compared to silicone and synthetic oils.

$$T_n = T_{w,n-1} + Q_n / (c_p * \dot{m}) + Q_n * R_n \quad (5.3)$$

Eq. 5.3 is used to model the temperature of the cell during operation. To determine the input thermal load (Q_n), a flux map of the incident solar rays is used in conjunction with the heat fraction of incoming light. The heat fraction is a function of the cell electrical efficiency, band gap, and IR transmissivity and expresses the portion of incident light that is converted to heat. Combined with the flux map, the total thermal load, Q_n , can be determined for every cell in the array. $T_{w,n-1}$ is the temperature of the cooling fluid flowing under the cells. This will increase as water moves downstream in the microchannel. To account for this, the thermal model calculates $T_{w,n-1}$ under each cell, moving along a channel. The thermal resistance (R_n) of the microfluidic channels is calculated using the equation shown below in (5.4) and (5.5). This modeling allows for the prediction of a range of cell temperatures for a given design, manufacturing errors, and changes in input power. The high lateral thermal resistance between two adjacent cells validates the 1D approximation of the model.

5.2.2.1 Thermal Resistance of the Microfluidic Channel (R_n)

$$R_n = R_{sapphire} + R_{PDMS} + R_{water} \quad (5.4)$$

Here,

- $R_{sapphire}$ is the thermal resistance of the sapphire substrate
- R_{PDMS} is the thermal resistance of the PDMS under the cell array
- R_{water} is the thermal resistance of the water in the channel

$$R_n = \frac{1}{Area_{cell}} \left(\frac{t_{saph}}{k_{saph}} + \frac{t_{PDMS}}{k_{PDMS}} + \frac{D_H}{Nu \cdot k_{water}} \right) \quad (5.5)$$

Here:

- $Area_{cell} = 30.25 \text{mm}^2$
- $t_{saph} = 2 \text{ mm}$: thickness of sapphire substrate
- $k_{saph} = 27 \text{ W/m-K}$: thermal conductivity of sapphire substrate
- $t_{PDMS} = 25 \text{ }\mu\text{m}$: thickness of PDMS under the cell array
- $k_{PDMS} = 0.20 \text{ W/m-K}$: thermal conductivity of PDMS under the cell array
- $t_{water} = 100 \text{ }\mu\text{m}$: thickness of water in the microchannels
- $k_{water} = 0.64 \text{ W/m-K}$: thermal conductivity of water

5.2.2.2 Modeled Temperature Map with and without Active Cooling

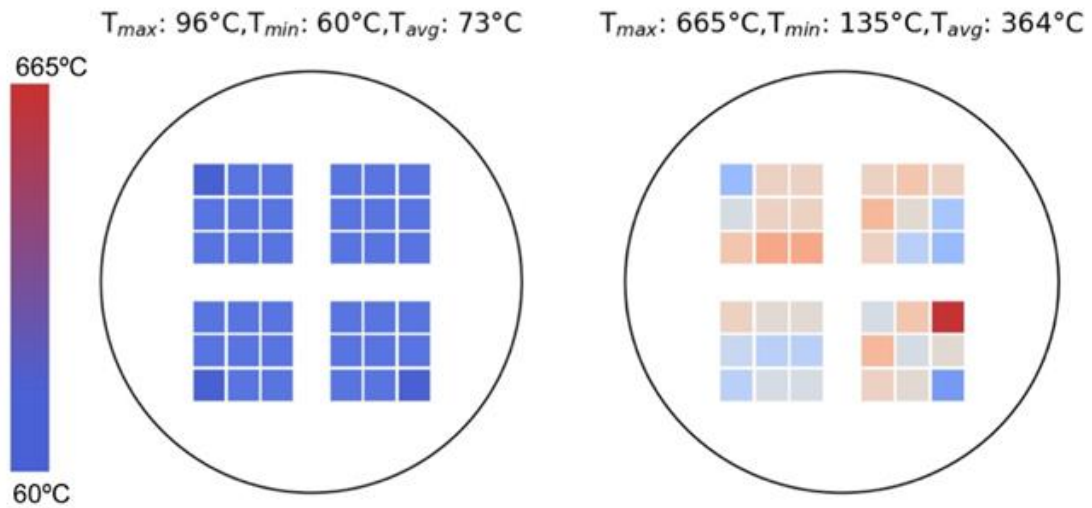


Figure 5.7 Temperature map of CPV module with (left) active microfluidic cooling and (right) passive cooling from top window convection only. The non-uniformity in the cell temperatures is a result of non-uniform flux pattern which was obtained from the concentrating mirror at the outdoor test site. Maps share same color palette.

Figure 5.7 shows the modeled temperature maps for the CPV with and without active cooling at an average concentration of 550 suns. With only natural convection passing over the top window, cell stagnation temperatures can reach upwards of 665 °C. In order to avoid encapsulant degradation and cell failure, the maximum allowed cell temperature in the module is 110 °C¹⁰⁷, demonstrating the necessity for robust thermal management. As the thermal model shows in Figure 5.7, active microchannel cooling allows cells to be maintained well below the 110 °C threshold.

5.2.3 Microfluidic Model

The most critical design parameter of the microchannels is the channel depth. The selection of channel depth affects the maximum cell temperature based on changes in thermal resistance, total energy transmission, and pressure drop across the channels. The thermal resistance of the microfluidic channel (R_{wat}) is driven by the convection coefficient (h_{conv}), given in Eq. (5.6), where the fully-developed Nusselt number is assumed to be 5.36 for isoflux, parallel plates, with one side insulated¹⁰⁸, k is the thermal conductivity of water, and D_h is the hydraulic diameter. The hydraulic diameter is 4 times the ratio between the cross-sectional area of flow path and the wetted perimeter as shown in Eq. (5.7), which for a rectangular cross section reduces to Eq. (5.8) where W and D are the width and depth of the channel, respectively (Figure 5.8). It is evident that increasing the channel depth increases D_h and reduces the h_{conv} which leads to lower cooling power and greater cell temperatures.

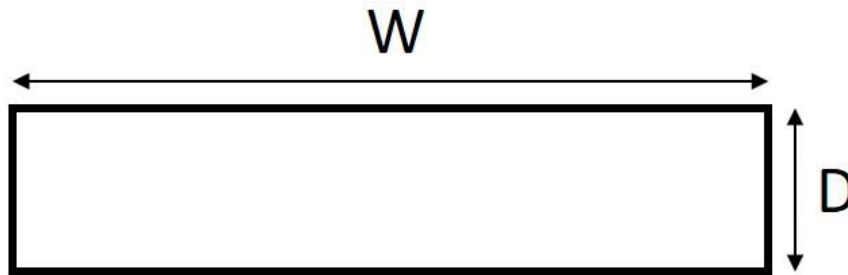


Figure 5.8 A rectangular microchannel to demonstrate the hydraulic diameter.

The pressure drop is directly influenced by the channel depth that regulates the required pumping power and the flowrate in the channels. As such, the microchannels and surrounding module need to be designed to avoid delamination of PDMS channels from

the sapphire substrate and fracturing of the sapphire. The pressure drop across the channels is calculated using the Darcy-Weisbach equation given in Eq. (5.9). Here, ΔP is the pressure drop across the channels, L is the length of a channel, f_D is the Darcy friction factor, ρ is the density of water, $\langle v \rangle$ is mean flow velocity and D_h is the hydraulic diameter. The Reynolds number is calculated using Eq. (5.10), Q is the mass flowrate, D_h is the hydraulic diameter, A is cross-sectional area, and μ is the viscosity of water. For laminar flow ($Re < 2300$) f_D can be calculated by Eq. (5.11), which makes the Darcy-Weisbach equation equivalent to the Hagen-Poiseuille model.

$$h_{conv} = \frac{Nu * k}{D_h} \quad (5.6)$$

$$D_h = \frac{4A}{P} \quad (5.7)$$

$$D_{h,rectangle} = \frac{2WD}{W+D} \quad (5.8)$$

$$\frac{\Delta P}{L} = \frac{f_D \rho \langle v \rangle^2}{2D_h} \quad (5.9)$$

$$Re = \frac{Q D_h}{A \mu} \quad (5.10)$$

$$f_D = \frac{64}{Re} \quad (5.11)$$

Figure 5.9 plots two important metrics, maximum cell temperature and pressure drop in the channels, as a function of channel depth at 550 suns irradiance and a constant flowrate of 10 g/s. There are two critical constraints: the working pressure in the channels must not

exceed ~16 psi (110.3 kPa) to prevent breaking of the sapphire substrate (safety factor of 1.0) and the maximum cell temperature must stay below 110 °C to prevent long term damage to the CPV module. This allows a range of 100 μm to 230 μm for the depth of the microchannels to stay within design constraints. To maximize optical transmission, 100 μm channel depth is chosen.

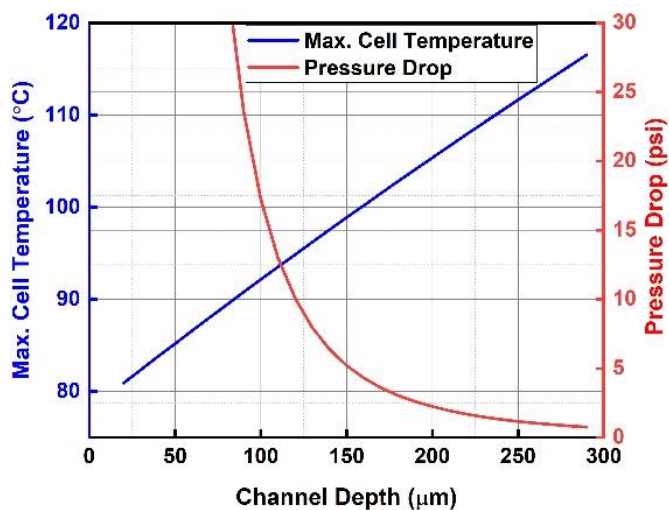


Figure 5.9 Plot of maximum cell temperature and pressure drop across the microchannels as a function of channel depth, with 550 suns irradiance.

5.2.4 Analytical Model for Flowrate vs. Pressure drop

The analytical model is developed using the Darcy-Weisbach equation. The model corresponds to only the microchannels and does not include the manifold with water inlets and outlets. The experimental data matched closely to ~130 μm thick microchannels. The mismatch in the model and experiment arises from the occasional cross-talk between the channels, allowing extra flow path for the water other than the microfluidic channels. It is also possible that PDMS expands under heat allowing for deeper channels.

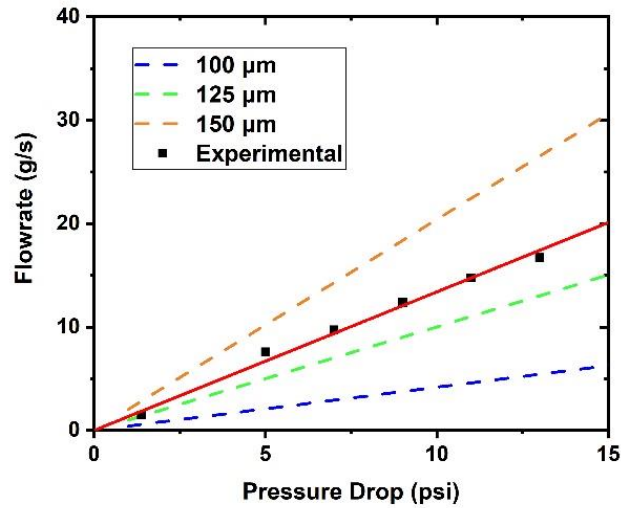


Figure 5.10 Modeled and experimental pressure drop vs. flowrate in the microchannels. Red line represents a linear fit to the experimental data.

To assure that the flow is fully developed before reaching the cells, the hydraulic and thermal entry length were calculated using Eq. (5.12) and (5.13), where Pr is the Prandtl number defined in equation (5.14) and c_p is the specific heat of water. From this it is found that the laminar flow develops before the first cell across all flow rates. The thermal profile is not fully developed within the channels before reaching the cells for flow rates greater than 5 g/s. The effects of this is discussed towards the end of the chapter in the cooling performance section.

$$L_{lam,flow} = 0.05ReD_h \quad (5.12)$$

$$L_{lam,therm} = 0.05RePrD_h \quad (5.13)$$

$$Pr = \frac{c_p\mu}{k} \quad (5.14)$$

5.3 Fabrication of Microchannels

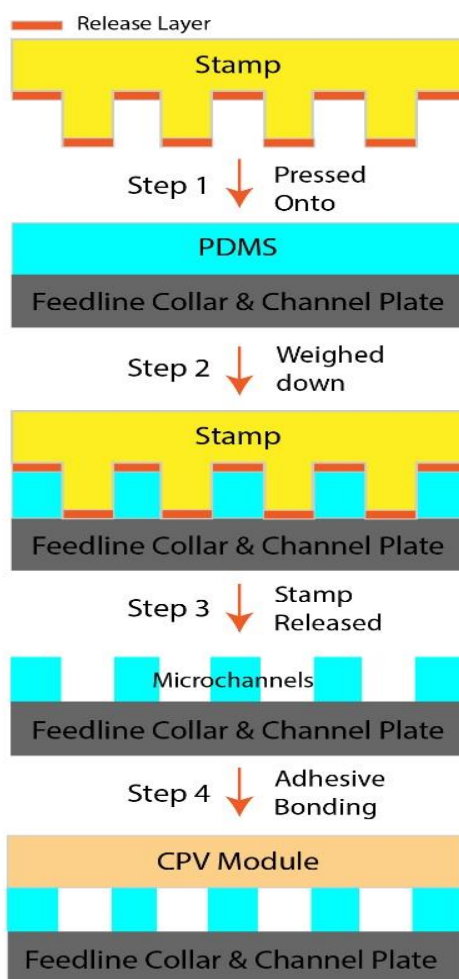


Figure 5.11 Complete process flow of the microchannels fabrication process.

The 100 μm thick microchannels are fabricated out of PDMS using a stamping method¹⁰⁹. Figure 5.11 summarizes the process. Dow Corning Sylgard 184 silicone elastomer is mixed at 10:1 (base:curing agent) and thoroughly degassed using an ultrasonic bath for 15 minutes followed by degassing in a vacuum chamber for 1 hour. The channel plate, consisting of a glass piece centered in an aluminum collar with inlet/outlet and mechanical fixation holes, is submerged into the PDMS bath. The stamp is formed by CNC milling the inverse pattern

of the channels into an aluminum block. It is important to get mirror-smooth finish in the aluminum stamp to prevent texturing of the microchannel surface that could lead to light scattering. The stamp is coated with a fluoroform release layer that facilitates an easy release from PDMS after curing. The fluoroform layer is deposited using CHF_3 gas in a reactive ion etcher (RIE) chamber, details of which can be found in the supplementary materials. The stamp is pressed into the PDMS to be in hard contact with the channel plate and weighted down as shown in Figure 5.11: step 1 and 2. The stack is degassed in a vacuum chamber for three hours to get rid of any air bubbles trapped underneath the stamp. Then the stack is left on a hotplate at $100\text{ }^\circ\text{C}$ for 3 hours to cure the PDMS. Finally, the stamp is removed from the cured PDMS as shown in Figure 5.11: step 3, leaving patterned and cured PDMS microchannels on the channel plate. The stamping process allows for channel fabrication on top of the channel plate without any base layer, resulting in high transmission of infrared light to the thermal receiver.

The patterns on the stamp inversely translate into the PDMS, i.e., any ridge in the stamp becomes a raise in the PDMS and vice versa. Figure 5.12 shows the height profile of the stamp, comparing it to the height profile of the microchannels using an optical profilometer. The stamp was also made using SU-8 3050 negative photoresists, both on silicon wafers and glass windows using photolithography. For alignment purposes, the glass window has certain advantages as the stamp window but SU-8 doesn't adhere very well on glass windows. SU-8 on silicon wafer as a mold is commonly used, but in this case, that poses certain disadvantages for alignment to the channel plate. Finally, aluminum is robust and can be used over and over without any issues as a stamp. With the aid of

alignment pins machined both on the stamp and the channel plate, the stamp and module may be aligned with ease.

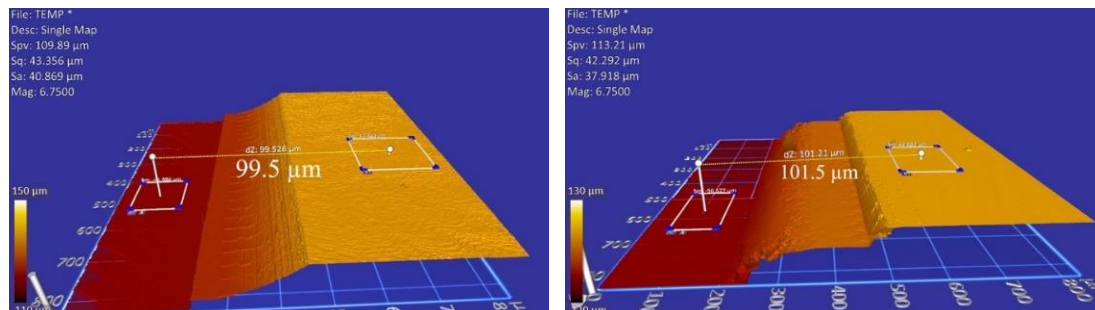


Figure 5.12 Optical profilometer showing step height of the stamp (left) and the microchannels (right).

Ensuring easy and clean release of the stamp from the cured PDMS is critical in the fabrication process. The stamps are coated with fluoroform deposited by a RIE tool using CHF_3 gas. For comparison, they are also coated with trichloro(octadecyl)silane (OTS) solution dissolved in pentane and then their contact angles are measured. Figure 5.13 shows comparative contact angle measurements on glass, silicon, and aluminum with OTS and fluoroform coating. High contact angle represents low surface energy meaning less favorable for bonding, thereby ensuring easy release from the PDMS microchannels. Aluminum with fluoroform, having the highest contact angle, is hence used for fabricating the microchannels.

The recipe used in the RIE for fluoroform deposition is as follows: RIE power 50 W, pressure 250 mTorr, CHF_3 flow 100 sccm, and time 10 min.

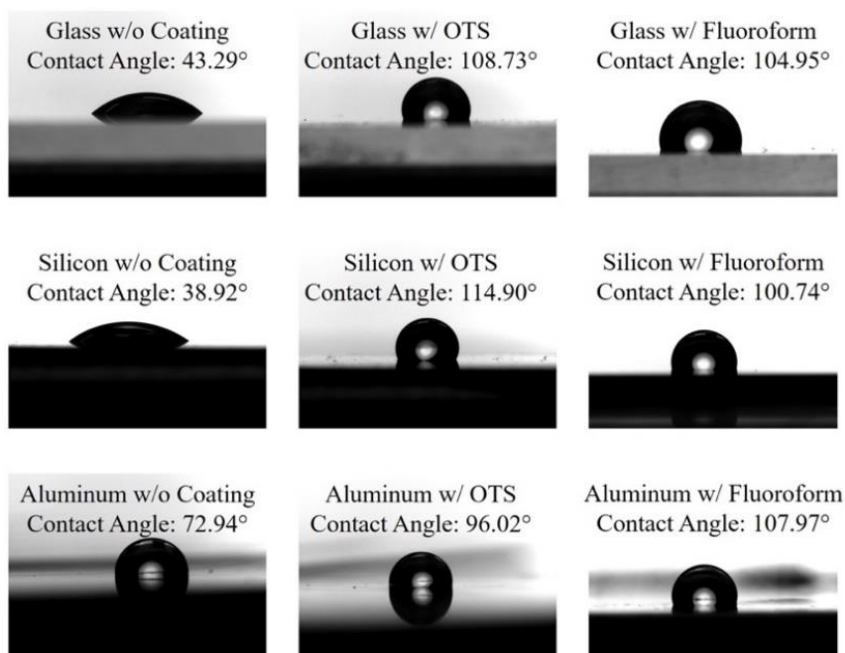


Figure 5.13 Contact angle measurement on glass, aluminum and silicon substrates with a droplet of water, with OTS and Fluoroform release layers and no release layer as reference.

Figure 5.14 top and bottom show a photograph of the stamp and fabricated channels on the channel plate, respectively. The microchannels are finally attached to the sapphire window using a commercial transparent optical adhesive (NOA 86H, Norland Products Inc.) that is selectively applied on the channel walls and on the outside perimeter using a stencil. The bonded sapphire-microchannels assembly is leak-tested using a submerged air test and holds seal at 30 psi, exceeding operational pressure.

Alternatively, the PDMS microchannels can be attached to the sapphire substrate using plasma enhanced bonding in a vacuum plasma chamber with the presence of oxygen gas¹¹⁰; for optimal bonding, the sapphire must be coated with an adhesion promoter (e.g. Dow Corning 1200 OS primer). Bonding between PDMS and bare untreated sapphire was

insufficient despite several attempts at different pressures, plasma source powers, flowrates of oxygen, and durations.

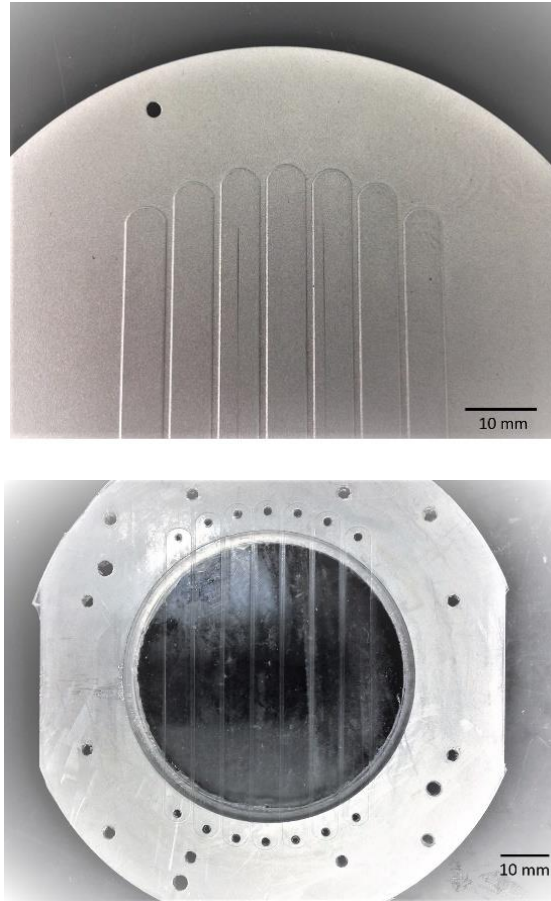


Figure 5.14 Photograph of the stamp (top) and the fabricated channels on the channel plate (bottom).

5.4 Results and Discussion

In the next section we will discuss the results of various characterizations such as flow characteristics, optical transmission, and cooling performance.

5.4.1 Flow Characteristics

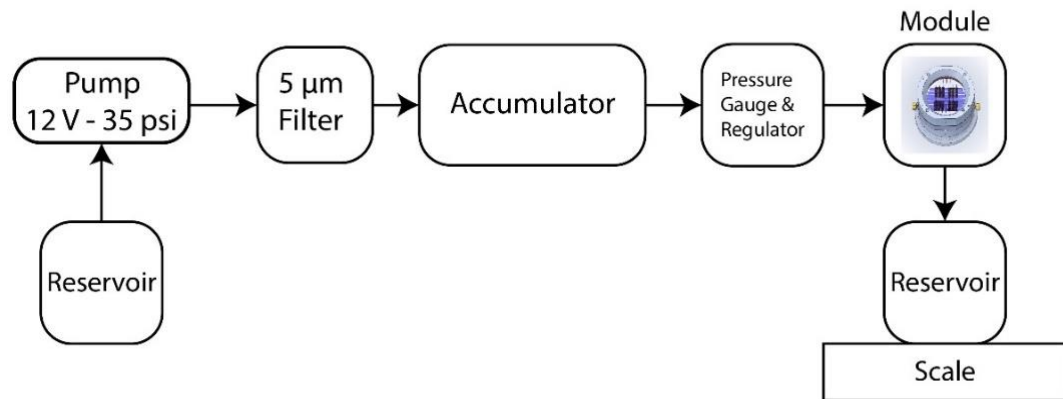


Figure 5.15 Fluid flow loop showing the test setup. The accumulator expansion tank was pre-charged to 40 psi on the air bladder side.

The flowrate of the microchannels as a function of pressure was tested using a fluid flow loop as shown in Figure 5.15. The following is a list of hardware that were used for the fluid-flow test, in order from inlet to outlet:

- 1) Inlet to water reservoir, which stores distilled water
- 2) 12 V diaphragm pump (4.3 L/min) with 35 psi pressure cut-off switch
- 3) 5 μm water filter
- 4) 2-gallon pre-pressurized (40 psi) accumulator tank
- 5) 0-60 psi pressure regulator with gauge
- 6) CPV module
- 7) Outlet to water reservoir resting on a scale for gravimetric flowrate reading

Lastly, 3/8" ID tubing was used for the test loop, except at the CPV module, which was designed for 1/8" ID tubes. A photograph of this fluid flow testbed is shown in Figure 5.16.

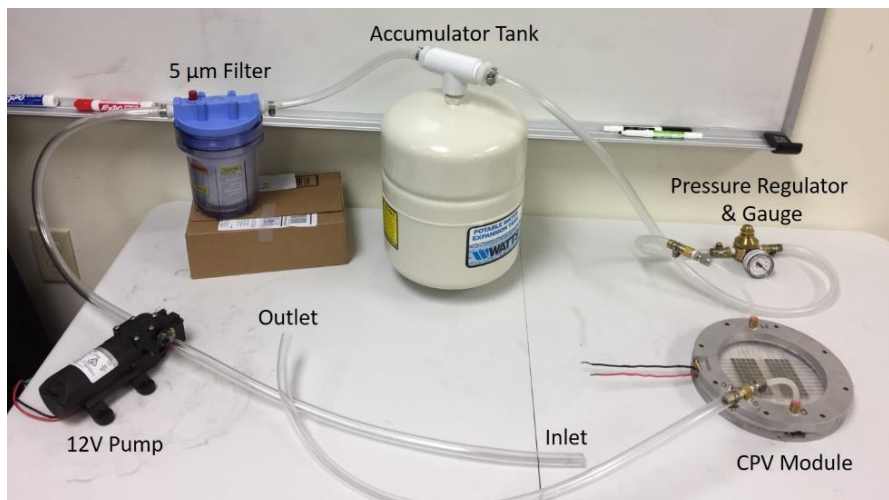


Figure 5.16 Photograph showing different components of the fluid-flow test setup.

Flowrate is calculated gravimetrically by measuring the water mass at the outlet reservoir at regular intervals. The pressure is measured before the module inlets and plotted vs. the flowrate as shown in Figure 5.17. The outlet of the module is at atmospheric pressure without any further drop downstream. Thus, the pressure measured at the inlet of the module represents the pressure drop across the microchannels and the inlet/outlet manifolds. A maximum flowrate of 16.7 g/s was achieved for 13 psi (89.6 kPa) pressure drop. The linear fit to the plot has a slope of $1.3 \pm 0.03 \text{ m}^{-1}\text{s}^{-1}$. An analytical model is developed using the Darcy-Weisbach equation to compare the flowrate vs. pressure characteristics, and the results are in good agreement with experimental findings for channels with 130 μm depth. The Reynolds numbers tested in the channels has a range of 57 to 953 for a fluid flow velocity of 0.3 ms^{-1} to 4.3 ms^{-1} , respectively. The calculated Reynolds numbers along with the linear relationship between the flowrate and pressure

drop is indicative of laminar nature of the flow within the microfluidic channels. The calculated h_{conv} is $1.7 \times 10^4 \text{ W/m}^2\text{K}$ for $\text{Nu} = 5.36$ which meets the minimum requirement of $h_{\text{conv}} > 10^4 \text{ W/m}^2\text{K}$.

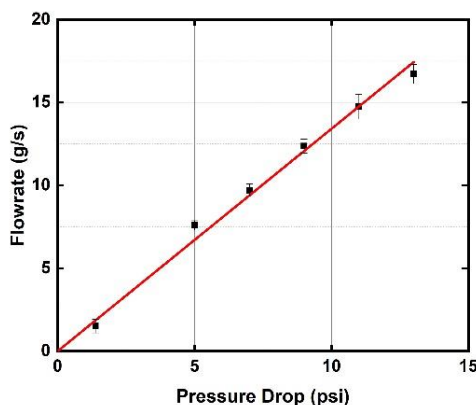


Figure 5.17 Pressure drop vs. flowrate in the microchannels. The red line shows a fit to the expected Darcy-Weisbach linear relationship for laminar flow.

5.4.2 Optical Transmission

Figure 5.18 (a) and (b) show transmission data for the optical stack of the CPV module, which includes a top quartz superstrate, PDMS-encapsulated CPV cells, and a bottom sapphire superstrate. The transmission is experimentally measured using a broadband (185nm to 1700nm) spectrometer (Ocean Optics). The UV-VIS-NIR light is provided by a balanced deuterium-halogen light source. The cell region transmission is plotted in Figure 5.18 (a) where the energy-weighted out-of-band ($\lambda > 873 \text{ nm}$) transmission is modeled as 65.4% and experimentally measured as 57.3%. The mismatch between model and experiment results from air bubbles trapped between the cells and the encapsulant, creating more reflecting interfaces. Microscope images of the air bubbles are added in the

supplementary information. Figure 5.18 (b) plots the transmission of the bypass regions, which are adjacent to the cells and contain only PDMS. For the bypass region, the total modeled energy-weighted transmission is 88%, and experimental is 89.5%. The differences between model and measurement is also attributed to measurement errors and differences in thicknesses of the different layers between model and experiments.

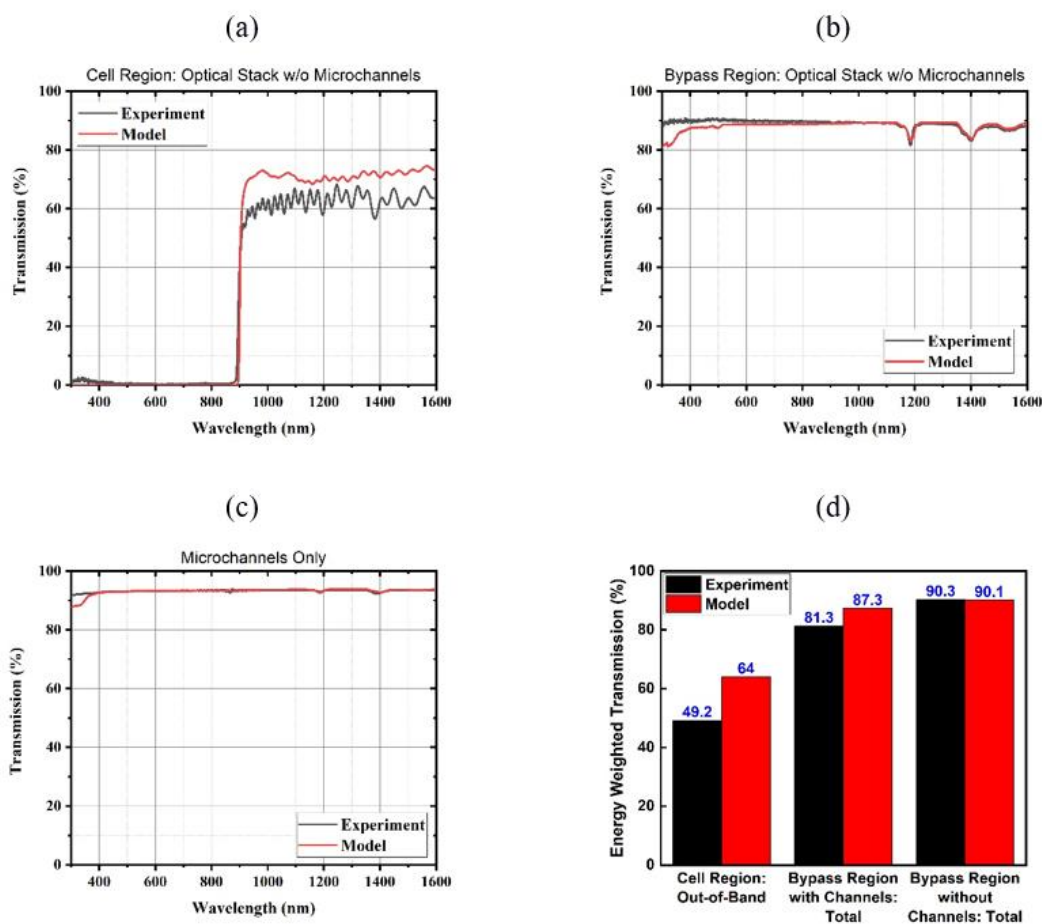


Figure 5.18 Transmission measurements and models for the optical stack without microchannels (a) cell region and (b) bypass region. (c) Transmission measurement and model for the microchannels only. (d) Energy weighted transmission at the three different regions of the CPV module with microchannels attached, i.e., cell region, bypass region with channels with 100 μm water, and bypass region without channels.

Transmission spectra for the microchannel layer, which includes the PDMS channels and the quartz channel plate, is shown in Figure 5.18 (c). The model and the measured data match closely and the energy-weighted transmission is 93% (model) and 93.2% (experiment).

The energy weighted transmission for the three different regions of the CPV module with microchannels attached, i.e., cell regions, bypass region with channels (100 μm water), and bypass region without channels are shown in Figure 5.18 (d). Contrary to intuition, the total transmission increases in part of the module with the inclusion of the microchannels due to refractive-index matching between sapphire and water-PDMS relative to sapphire and air. For the bypass region without channels, the total solar-spectrum-energy-weighted transmission increases by 0.9% relative with the attachment of the microchannels. On the other hand, for the cell region and bypass region with channels, the total solar-spectrum-energy-weighted transmission drop by 14.1% and 9.2% relative, respectively, due to the absorption losses in water. Table 5.2 lists the energy-weighted transmission and power flow in the three different regions of the CPV module. The active cooling microchannels reduce the total experimentally measured energy-weighted transmission of the CPV module by 5.2% relative, whereas the model shows an improvement in transmission by 0.4% relative. The relative improvement predicted by the model is due to the reduction in Fresnel reflections at the sapphire-air interface when the PDMS and quartz layers from the active cooling are added to the back of the module.

Table 5.2 Modeled and experimental energy-weighted transmission in all three regions of the CPV module, with corresponding power flow.

Region	Cell	Bypass with channel	Bypass without channel	Total
Input power (%)	54	18	28	100
Input power (W)	1176.1	392.1	609.8	2178
Total solar energy-weighted transmission of the CPV module without active cooling - Experiment (%)	18.9	89.5		N/A
Transmitted power of the CPV module without active cooling (W)	222.3	350.9	545.8	1119
Total energy-weighted transmission of the CPV module with active cooling microchannels - Experiment (%)	16.2	81.3	90.3	N/A
Transmitted power of the CPV module with active cooling microchannels (W)	191	318.7	550.7	1060.4
Power loss/gain with the addition of active cooling microchannels - Experiment (W)	-31.3	-32.2	+4.9	-58.6
Power loss/gain with the addition of active cooling microchannels - Experiment (%)	-14.1	-9.2	+0.9	-5.2
Total energy-weighted transmission of the CPV module without active cooling - Model (%)	21.6	88		N/A
Transmitted power of the CPV module without active cooling (W)	253.8	345	536.7	1135.5
Total energy-weighted transmission of the CPV module with active cooling microchannels - Model (%)	21.1	87.3	90.1	N/A
Transmitted power of the CPV module with active cooling microchannels (W)	248.4	342.3	549.5	1140.2
Power loss/gain with the addition of active cooling microchannels - Model (W)	-5.4	-2.8	+12.8	+4.6
Power loss/gain with the addition of active cooling microchannels - Model (%)	-2.1	-0.8	+2.4	+0.4

5.4.3 CPV Cooling Performance

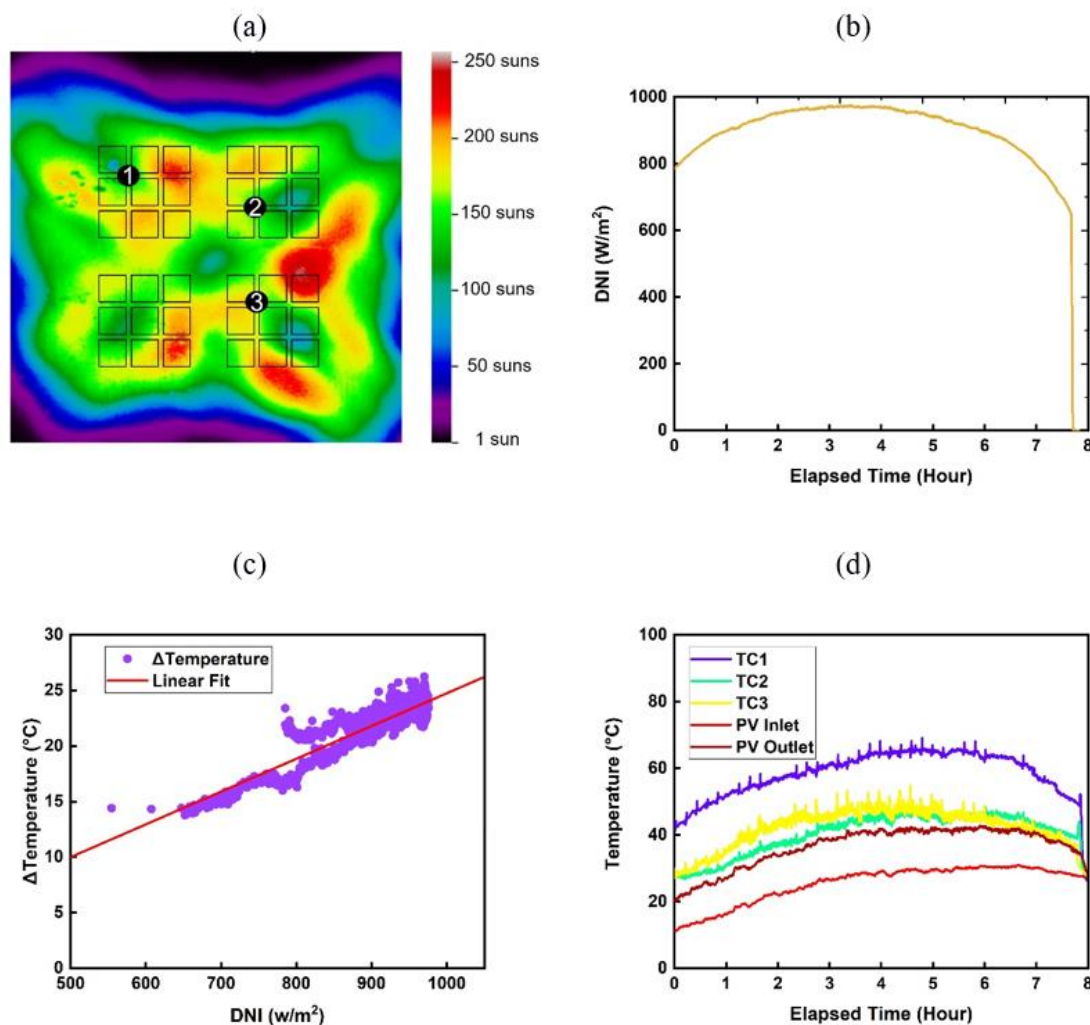


Figure 5.19 (a) Map showing distribution of solar energy flux on the CPV module. Black dots represent three locations where thermocouples were placed to monitor real-time temperatures. The scale bar represents number of suns. (b) Measured DNI for the ~8-hour period of testing shown here, in San Diego, Ca. Only 35% of the mirror area was exposed during CPV operation (c) Typical cell temperature vs DNI plot demonstrating linear relation, plotted only for “on-sun” data. (d) Temperature measurements for the three thermocouple locations shown in (a), water inlet, and water outlet.

The cooling channels were tested in an outdoor CPV testbed in San Diego, CA. All monitored regions were maintained below the threshold temperature of 110 °C throughout the duration of the test with peak solar direct normal irradiance (DNI) of 937 W/m² masked down to 35% exposed mirror area to an average concentration of 163 suns on the module. Figure 5.19 (a) is a flux map showing the concentration distribution across the CPV plane and Figure 5.19 (b) plots the DNI for a ~8-hour testing period. Figure 5.19 (c) plots the change in cell temperature ($T-T_w$) with respect to the measured DNI averaged over all cells once the system has achieved steady state. As temperature is approximately linear with power input at low temperatures according to Fourier's law ($Q \cdot R = dT$), a fit line can be drawn to determine the thermal resistance of the module under each thermocouple. Figure 5.19 (d) shows the cell temperatures in three different locations marked in Figure 5.19 (a) as well as the inlet and outlet temperature of the cooling water. These temperature measurements correspond to the DNI plot shown in Figure 5.19 (b). The pressure drop across the channel was 1.4 psi (9.5 kPa) and average flowrate was 1.5 g/s during the outdoor tests. Additionally, the cooling water extracts ~20% of the input power that reaches the CPV/T assembly (70 W out of 400 W incident power), adding a third output low temperature thermal energy stream to the existing electricity and high temperature thermal energy outputs. More details on the system testbed, power streams, and overall transmissive CPV module electrical performance is published by Robertson et al.¹¹¹.

Table 5.3 includes the modeled and measured maximum temperatures and thermal resistances for the three monitored regions. The calculated thermal resistance varied from 3-9 K/W. TC1 measured relatively higher temperature than TC2 and TC3, even though TC1 was at lower concentration spot compared to TC2 and TC3. The large range of thermal

resistances and this irregular trend of temperatures and thermal resistances is most likely due to heterogeneity in the manufacturing process, including varying thickness of the encapsulant or the presence of air bubbles under individual cells (bubbles size ranging from 0 to 80% of the cell area were observed) increasing thermal resistance. As shown, the measured thermal resistances also vary from the modeled values.

Table 5.3 Modeled and measured maximum temperatures and thermal resistance for the average concentration and at three different thermocouple (TC) locations (as shown in Figure 5.19a) marked as TC1, TC2, and TC3.

Location	Concentration	Maximum Temperature [°C]		Thermal Resistance [K/W]	
		Modeled	Measured	Modeled	Measured
Average	163	43	57	8.34	5.23±0.38
TC1	157	41	69	10.2	9.35±0.08
TC2	170	43	48	7.27	3.21±0.04
TC3	175	44	54	7.27	7.25±0.11

There are several differences between the model and the experimental conditions. First, the model ignored the potential for air bubble formation under the cells due to the stochastic nature of their development and large error in determining the volume fraction and distribution under the cells in the CPV module. Air bubbles increase the thermal resistance compared to the model. Second, the model assumes fully thermally developed flow. However, as noted in the analytical model for flowrate vs. pressure drop section, at the flow rates used in the testing, the thermal profile is not fully developed potentially leading to greater heat transfer. Finally, the model under-predicts the cell temperature but over-

predicts the thermal resistance. It is possible that the thermocouples were heated up themselves and measured higher cell temperatures. Also, the CPV module received spillage power from the mirror that introduced additional heat to the module collar. These extra heat sources may have added to experimentally measured cell temperature, which the model did not take into account.

5.5 Conclusions and Future Work

In conclusion, 100 μm thick microfluidic channels are fabricated and implemented in a hybrid transmissive CPV/T system. Using the maximum experimental thermal resistance, the peak concentration a cell can withstand before reaching the 110 $^{\circ}\text{C}$ threshold is projected as 665 suns. When unmasked to 100% mirror area, the concentration on the CPV module would range from 300 to 665 suns with an average of 450 suns. This would lead to a temperature distribution ranging from 65 $^{\circ}\text{C}$ to 109 $^{\circ}\text{C}$ with a mean of 82 $^{\circ}\text{C}$; the thermal resistance used in this projection is the experimentally obtained one instead of the calculated one and hence the difference from the model in Section 5.2. As seen in Figure 5.19a, there are a number of hot spots within the flux map where mirror defects or loading deflection may cause non-homogeneity within the flux pattern. A more uniform distribution of the flux from the mirror and greater uniformity in the manufacturing process is required to enable increased reliability and predictability in thermal performance.

The data presented here shows great potential for active cooling of CPV modules while selectively splitting the incident spectrum and transmitting the low energy photons through the CPV module. The major advantage of this design is the transmissive nature of the active cooling system, which is otherwise non-existent in prior art. However, one major challenge

of this design is the use of a sapphire window. Sapphire is generally expensive compared to traditional window materials, but it is essential for the aforementioned design due to its high thermal conductivity; the price of synthetic sapphire may come down substantially as large-scale personal electronics markets incorporate its use. Alternate CPV module designs that use direct fluid cooling of the cells may enable transmissive CPV active cooling without the use of sapphire. Another major challenge is the air bubbles that form due to delamination of the encapsulant at the cell-PDMS interface. Better adhesion between the cells and the encapsulant is critical and would improve the performance of the cooling system substantially. Similar to other CPV technologies, this problem is addressable in the manufacturing phase. Keeping the inlet water temperature low enough can also present a challenge during hot summer days, and the cooling system needs to take this into account.

6 CONCLUSION

In conclusion, this dissertation presents two promising approaches for future solar energy conversion technologies - 2D TMDC-based photovoltaic devices and hybrid CPV/thermal solar converters. Scalable and large-area synthesis of 2D MoS₂ is presented along with extensive optical and electronic characterization. Various optoelectronic devices, including transistors, photodetectors, and photovoltaics, have been designed, fabricated, and characterized. On the other hand, a microfluidic active cooling system is designed, fabricated, and characterized for application in a hybrid CPV/thermal solar converter.

6.1 2D Materials-based Optoelectronic Devices

2D materials are very promising materials for future optoelectronic applications. In Chapter 2, an extensive optical characterization of 2D MoS₂ is presented. Chapters 3 and 4 presents the optoelectronic devices made with 2D MoS₂.

In Chapter 2, the optical properties of 2D MoS₂ have been presented using variable angle spectroscopic ellipsometry measurements over a broad spectral range between 190 nm to 1700 nm. The ellipsometry data are sensitive to birefringence effects in the thickest thin-film sample. These birefringence effects are investigated and an analysis method is developed to analyze the ellipsometry data and extract the in-plane and out-of-plane optical

properties. The complex refractive index is then used to calculate reflectance, transmittance, and absorption of the MoS₂ films using the transfer matrix method (TMM) and matched with experimentally measured transmittance of the same samples. The modeled results show that monolayer, few-layer, and thin-film MoS₂ absorbs 7.4%, 12.6%, and 32.4% of the incident light, respectively, between 300 nm to 700 nm. When normalized to per unit-thickness absorption, monolayer MoS₂ absorbs 12.1%/nm. In comparison, few-layer and thin-film MoS₂ absorbs 5.9%/nm and 1.1%/nm, respectively, clearly showing superior light-matter interaction in the monolayer and few-layer films. TMM models are further used to design optical coatings for these films to either confine absorption in a narrow bandwidth for photodetector applications or enhance broadband absorption for photovoltaic applications. A thin film of TiO₂ is shown to be effective in limiting absorption in monolayer and few-layer MoS₂ to only 300 to 550 nm incident light. In comparison, 60 nm of SiN on top of thin-film MoS₂, as an anti-reflection coating, increases the broadband absorption between 300 nm and 800 nm by 44.1%, relatively, from 29.1% absorption without any ARC to 41.9% absorption with the SiN layer. Furthermore, the model calculates absorption in 250 nm thin-film MoS₂ to be 59.4%, and with an additional 60 nm ITO on top, the absorption is enhanced to 77.9% (between 300 nm and 800 nm incident light in both cases). The model also predicts that, assuming a 100% internal quantum efficiency, the J_{sc} of a photovoltaic device made with 250 nm thin-film MoS₂ can be improved from 20.3 mA/cm² to 26.8 mA/cm² with the addition of the 60 nm ITO coating, a 32% relative increase. These experiments and models illustrate the usefulness of this complex refractive index data for designing future optoelectronic devices using 2D MoS₂.

In Chapter 3, bottom-gated transistors and photodetectors are fabricated with monolayer MoS₂ with 10 μm channel length and 100 μm channel width. 5 nm Ti capped by 45 nm of Au are used for symmetric source-drain contacts. The bottom gate is probed at the highly-doped Si layer underneath the native oxide layer by scratching through the oxide layer. A high carrier mobility of 3.3 cm²V⁻¹s⁻¹ is achieved with 300 nm SiO₂ as the gate dielectric. The carrier mobility could be improved by using a high-k dielectric for transistor applications. EQE and photoresponsivity are also presented for the transistor-type photodetectors. It shows a 25% EQE at 420 nm incident wavelength, measured at a source-drain bias of 5V. Photoresponsivity of the same device is calculated to be 0.09 A/W also at 420 nm incidence for an input power of 0.1 mW. Finally, a chemical treatment method is presented that effectively enhances the photocurrent of a photodetector. By soaking the photodetectors in 1,2-Dichloroethane for 4 hours at 60 °C, their photocurrent increases by a factor of ~25x at the 420 nm C-peak and ~2.5x throughout the rest of the visible spectrum. The improvement in the performance is attributed to chlorine atoms from the DCE solution substituting sulfur vacancies, thus reducing defects in the material.

In chapter 4, we presented the design principles, fabrication, characterization, and an optoelectronic model of a large-area Schottky-junction monolayer MoS₂-based photovoltaic device. Au/Ti and Pt are used as asymmetric contacts for electron and hole collection, respectively. Two different kinds of devices are fabricated: one simple square contact-pad type device with asymmetric contacts similar to a transistor or photodetector in architecture, and another finger-busbar type device, much like a typical solar cell with interlocking asymmetric contacts. With monolayer MoS₂ on Ti and Pt contacts, a V_{OC} of 270 mV is achieved with the simple square contact pad type device under monochromatic

high-intensity laser illumination. At the same time, the finger-busbar device shows a V_{oc} of 110 mV under one-sun AM1.5D illumination. The devices are limited by hole transport, resulting in low current density and low overall power conversion efficiency. Various approaches have been proposed at the end of the chapter to improve the device performance.

6.2 2D Materials Outlook

In the short term, a vertical Schottky-junction photovoltaic device made with asymmetric Ti and Pt contacts is the lowest hanging fruit⁸². For easier fabrication, 2D MoS₂ can be directly transferred onto the bottom Pt contact. Finger patterns can be drawn on the top for Ti contacts, thus avoiding alignment steps in the lithography. Particular attention must be given to material uniformity, device geometry, and passivation of contacts.

For future devices, further improvement of the CVD-grown 2D materials' carrier mobility and effective doping are vital. With effective p-type and n-type doping, p-n junction based device structures can be fabricated for better carrier separation. As mentioned earlier, MoS₂ has a native n-type doping. Since most optoelectronic applications require controlled bipolar doping for charge separation, it is crucial to increase the n-dopant concentration in the n-type MoS₂ as well as to be able to dope them to become p-type. Improvement in the n-doping can be achieved by replacing sulfur vacancies with chlorine or other atoms, as shown in Chapter 3. P-type MoS₂ can be achieved by partially substituting Mo with Nb host atoms in¹¹², for example, the seed layer of TVS-grown TMDCs. Other elements like V and Ta that are in the same group as Nb in the periodic table could also be effective p-type dopant for MoS₂.

Furthermore, it is essential to clearly identify device architectures for carrier modulation and charge separation with effective contact schemes¹¹³. Various metals, including Sc, In, Al, Cr, Mo, Ni, Au, and Pd, as well as conductive oxides such as ITO and NiO, are proposed for 2D photovoltaics to obtain higher V_{OC} ; extensive work needs to be carried out in this regard⁷⁸.

Heterojunction devices of n-type MoS₂ with p-type WSe₂ have been fabricated as an alternative to homojunction, but they usually suffer from their type-II band offset¹¹⁴. In summary, it is important to carefully identify the best device architecture for homojunction vs. heterojunction devices, lateral vs. vertical devices, and to employ contact engineering with not only metals but also conductive oxides.

In the short term, lateral heterojunction devices using MoS₂-WSe₂ are also promising. Still, only a vertical stack of a p-type and n-type 2D TMDCs can unleash the true potential of these materials. Also, because of their enormous potential for use in space photovoltaics technology due to their very high specific power density and radiation hardness¹¹⁵, multijunction 2D photovoltaics can be a gamechanger in the future.

6.3 Transmissive Active Cooling in a Hybrid Solar Converter

In Chapter 5, transmissive microchannels were designed, fabricated, characterized, and field-tested for the cooling of a hybrid CPV/T system. This is the first demonstration of an optically transparent cooling system for CPV modules. An optimum design was found utilizing a sapphire substrate and 100 μm thick microchannels running underneath the cells. The microchannels were fabricated using polydimethylsiloxane by a highly repeatable

stamping method. The cooling channels keep CPV cell temperatures below 69 °C under concentrated testing up to 175 suns, and an experimentally-validated model predicts that the cell temperatures stay below the designated maximum of 110 °C for up to 665 suns. The microchannels are transparent to the solar spectrum and were found to decrease the solar-spectrum-energy-weighted transmission of the module by only 5.2% relative to a module without any cooling channels. The CPV module achieves a transmission of 58% (out-of-band), 85.6% and 91.8% of concentrated sunlight, respectively for the cell region, the bypass region with channels and the bypass region without channels. Maximum flowrate through the cooling channels was measured to be 16.7 g/s with a 13 psi (89.6 kPa) pressure drop in the channels.

6.4 Transmissive Microchannels Outlook

The microfluidic channels presented here enable the active cooling of transmissive CPV modules coupled to high temperature thermal receivers for hybrid solar energy conversion applications. They can be utilized for coupling photovoltaic electricity cogeneration to other applications such as thermal energy storage for dispatchable electricity production, industrial process heating in a wide range of settings, desalination, ammonia generation, water heating, photocatalysis, and more. Beyond solar energy conversion, optically transmissive microchannel cooling can open new doors for other types of optoelectronic device applications that have yet to be explored.

6.5 Final Thoughts

I can see that the application of 2D MoS₂ will soon be extended beyond the optoelectronic devices presented here to metasurfaces and other interesting photonic devices. Figure 6.1 is an experimental nanoantenna array patterned from monolayer MoS₂ that is only 0.65 nm thick. The patterns were fabricated by electron-beam lithography followed by MoS₂ etching. These could likely be used to create gate tunable dynamic metasurfaces to modulate optical properties in the visible spectrum¹¹⁶. We have to wait to see what the future holds for these exciting materials, but it is safe to say that MoS₂ and other 2D TMDCs are here to stay.

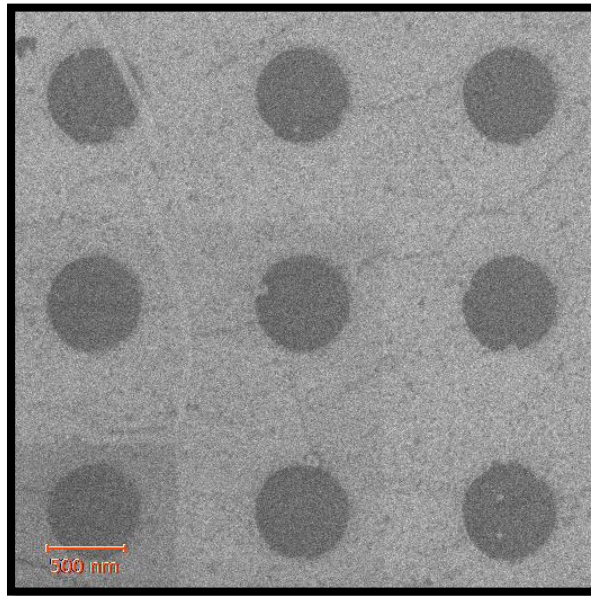


Figure 6.1 SEM image of nanoantenna array patterned from monolayer MoS₂ by electron-beam lithography followed by MoS₂ etching. The exciting applications of such photonic structures are yet to be fully explored.

APPENDIX A: OPTOELECTRONIC DEVICE

FABRICATION

This appendix contains step-by-step recipes for fabricating 2D MoS₂-based optoelectronic devices.

1. Start with a SiO₂-on-Si substrate. Cleave it roughly into a 1 cm x 1 cm piece. Clean the sample with solvents: acetone and IPA, and dry with blowing N₂. Descum the sample with the following recipe: 10 sccm O₂, 500 mTorr, 45 W, 60 seconds
2. Either synthesize MoS₂ directly on top or transfer sapphire-grown MoS₂ on top. The synthesis and transfer methods are described in detail in Chapter 2. For the finger-busbar type photovoltaic devices, MoS₂ is transferred on top of the contacts as the last step. For all other devices, MoS₂ is grown or transferred on to the SiO₂-on-Si substrate at this step.
3. Clean the sample with solvents: acetone and IPA, and dry with blowing N₂.
4. Spin coat the sample with 600 nm PMMA 950 A7. The spin coating is a two-step process:
 - a. Step 1: 15 seconds, 500 rpm speed, 100 rpm acceleration
 - b. Step 2: 45 seconds, 4000 rpm speed, 500 rpm acceleration
5. Bake at 180 °C for 90 seconds.

6. Do electron beam lithography (EBL) to write the device patterns using the following process parameters:
 - a. High current (HC) mode (typically 28000 pA current), 50 kV beam, 60 μm aperture
 - b. Dose: 650 $\mu\text{C}/\text{cm}^2$, area step size and line spacing: 5-20 nm, Dwell time is calculated by the software using the measured current, set dose, and set area step size/line spacing.
 - c. 500 μm write fields are used
7. Draw patterns using the GDS drawing tool and set the starting coordinate of the total write field in the position list such that the patterns are at the center of the sample.
8. Once the exposure is complete, remove the sample from the EBL tool and develop using the MIBK:IPA 1:3 developer for 30 seconds. Rinse IPA on the sample to clean off the residual MIBK.
9. Scratch off on the side on SiO_2 to expose the underlying highly doped Si layer for gate contacts- only needed for transistors
10. Descum the sample before loading inside the electron beam evaporator with the following process recipe: 10 sccm O_2 , 500 mTorr, 45 W, 5 seconds
11. Deposit 5 nm Ti followed by 45 nm Au- the source-drain metals for the symmetric contact devices and gate for transistors. Ti is in direct contact with MoS_2 ; the Au layer is a capping layer to prevent Ti oxidation. Ti and Au are both deposited at 1 A/s deposition rate. Note- this step will only deposit the contact metal for either source or drain for the asymmetric contact devices.

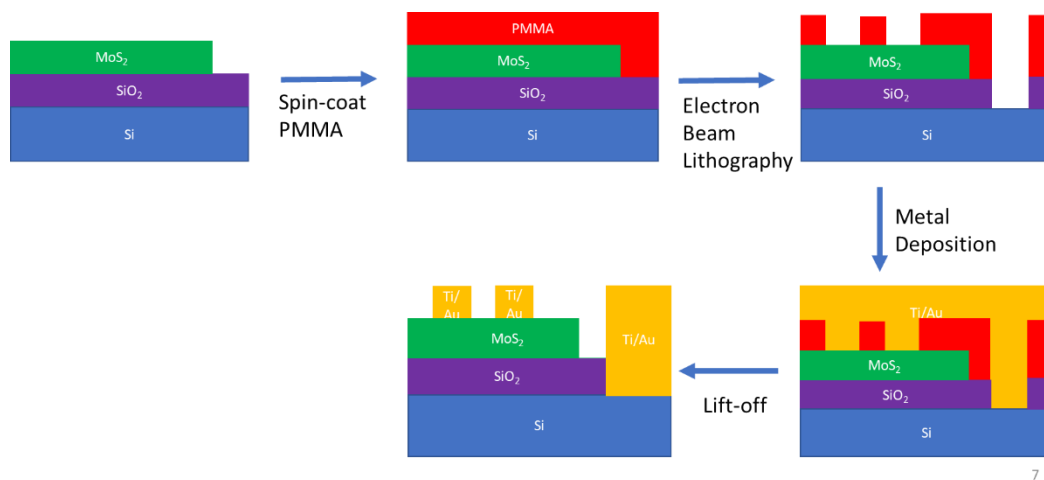
12. Lift-off metals and PMMA in a petri dish with acetone. Use pipette for agitation.
Occasionally this step will require an ultra sonicator lift off the metals.

Step 12 would be the last step for symmetric-contact transistors and photodetectors fabrication. The following steps are only required for asymmetric-contact photovoltaics fabrication.

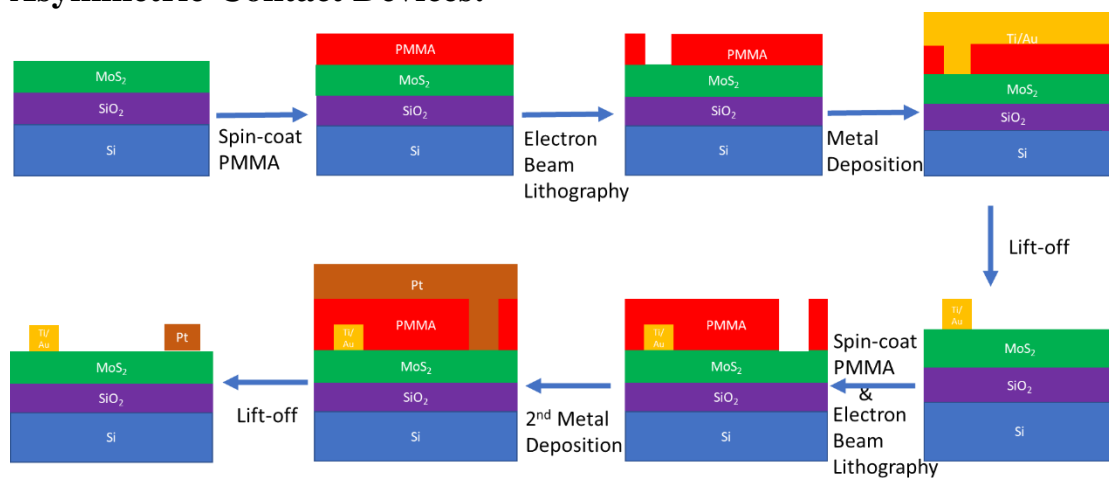
13. Repeat steps 3 through 8. In step 6, do a 3 point alignment lithography for the asymmetric contacts; they must align with the 1st metal contacts for designed channel width and length.
14. Descum the sample before loading inside the electron beam evaporator for the 2nd metal deposition with the following process recipe: 10 sccm O₂, 500 mTorr, 45 W, 5 seconds
15. Deposit 50 nm Pt as the 2nd metal contact with a deposition rate of 1 Å/s. Lift-off metals and PMMA in a petri dish with acetone. Use pipette for agitation.
16. Check under an optical microscope and confirm channel length and width before proceeding to further characterizations.

The following two schematics show the important steps of the fabrication process.

Symmetric-Contact Devices:

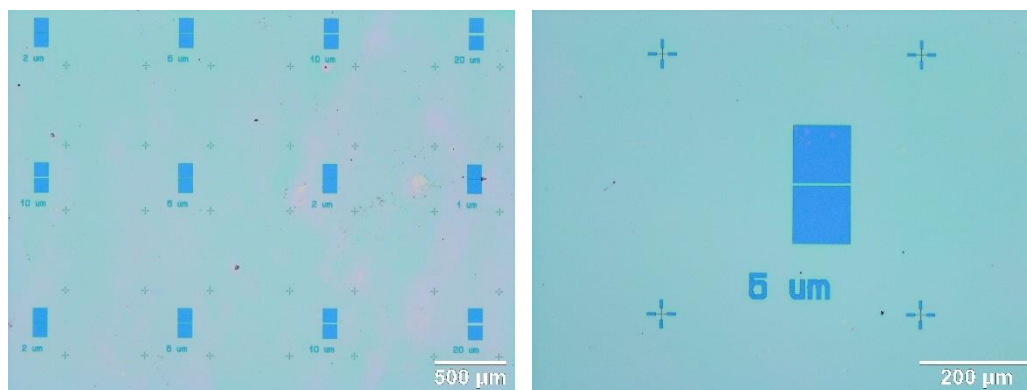


Asymmetric-Contact Devices:

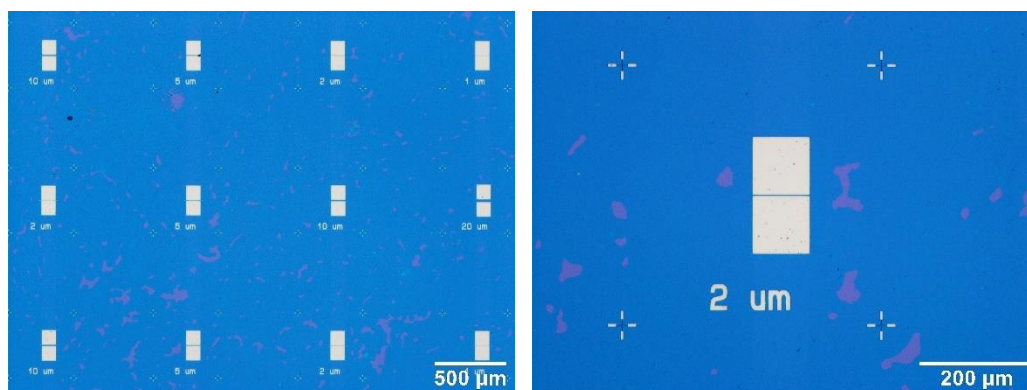


Optical micrographs of various stages of the fabrication process for the asymmetric-contact-pad devices

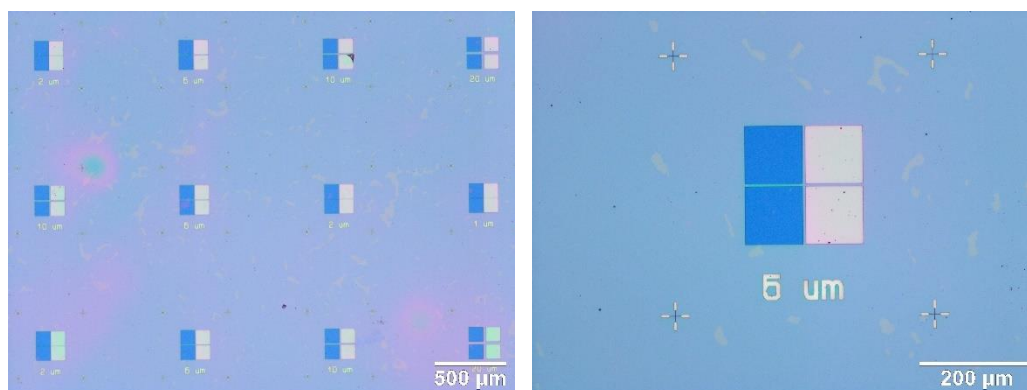
1st EBL step (post-development)



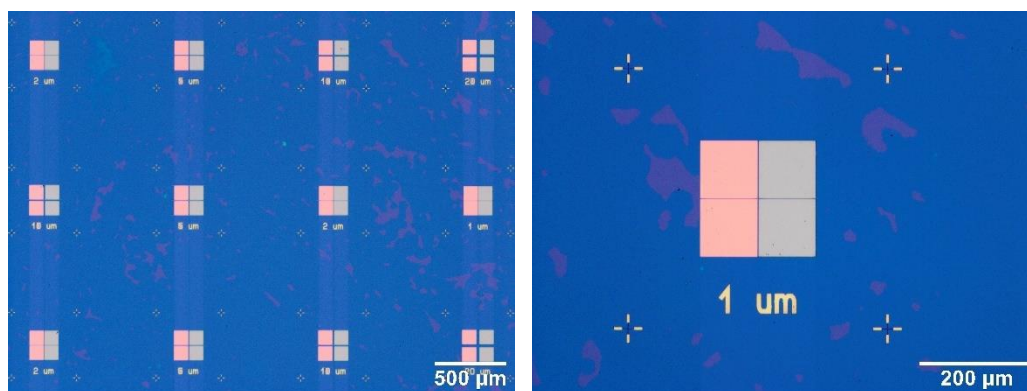
1st metal deposition (post liftoff)



2nd EBL step with 3 point alignment (post-development)

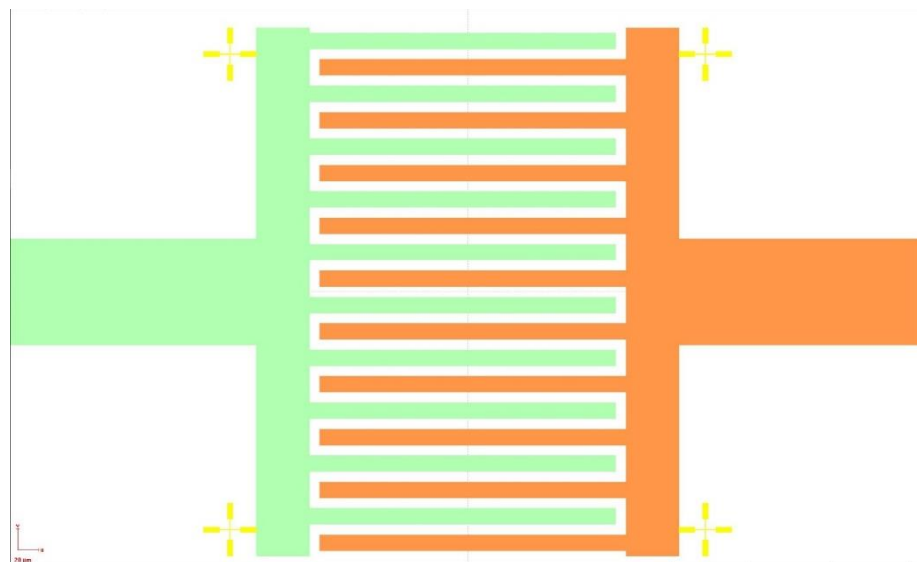
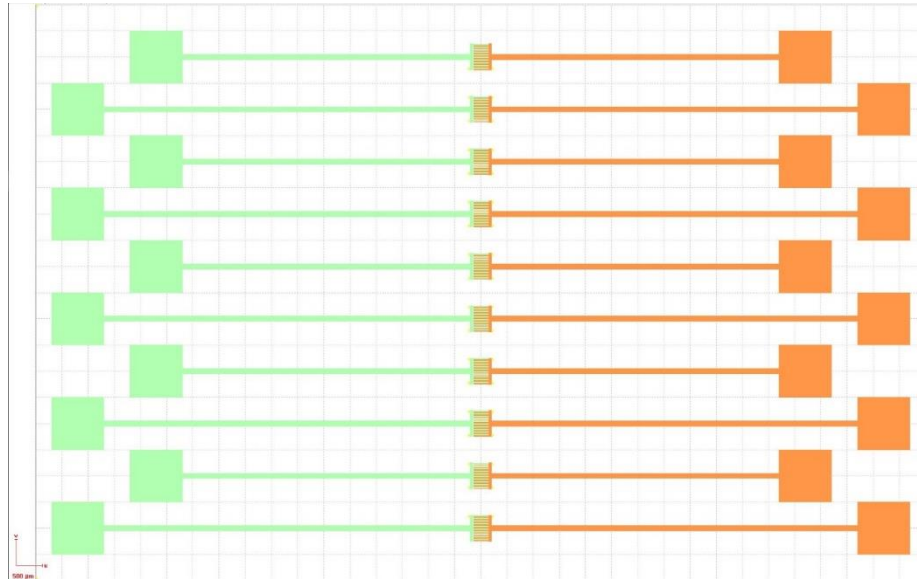


2nd metal deposition (post liftoff)



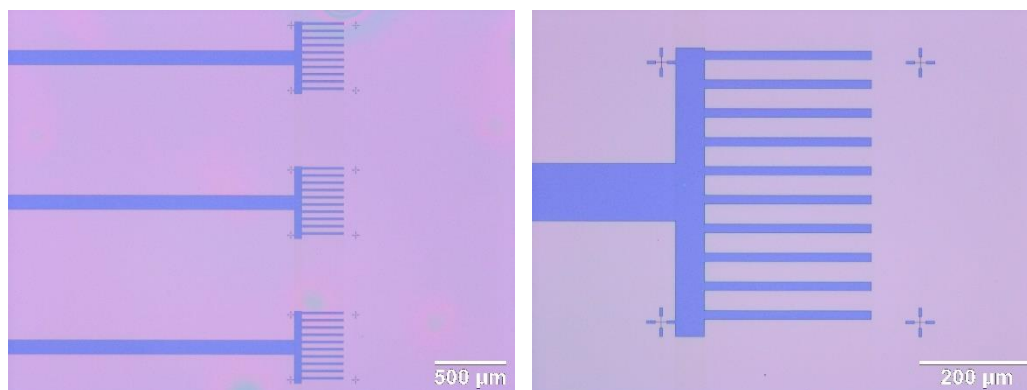
GDS design of the finger-busbar type devices

The top image shows an array of ten devices with extended contact pads. The bottom image shows a zoom-in of one individual finger-busbar type device. The scale bar is 500 μm in the top image and 20 μm in the bottom image.

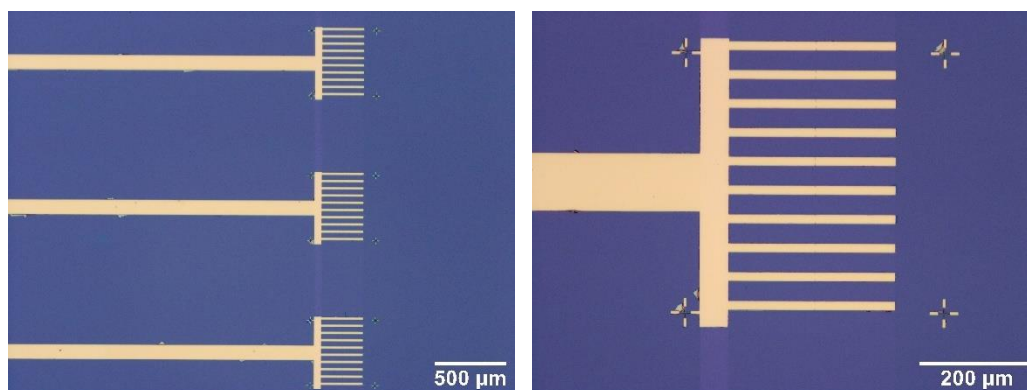


Optical micrographs of various stages of the fabrication process for the asymmetric-contact-pad devices

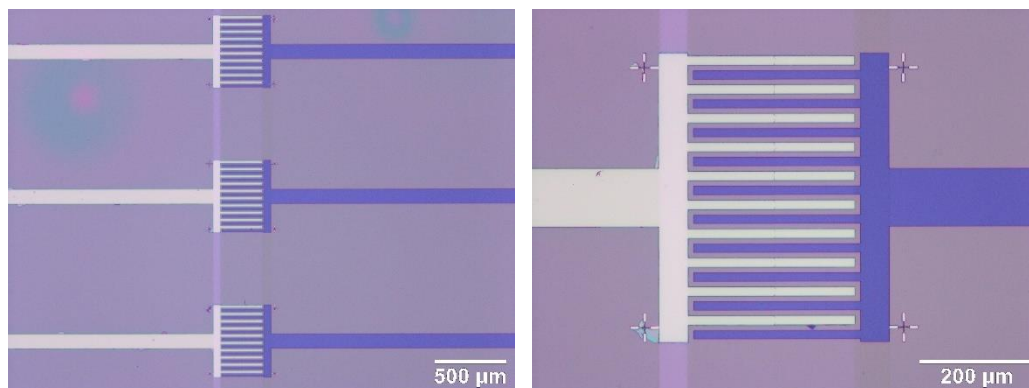
1st EBL step (post-development)



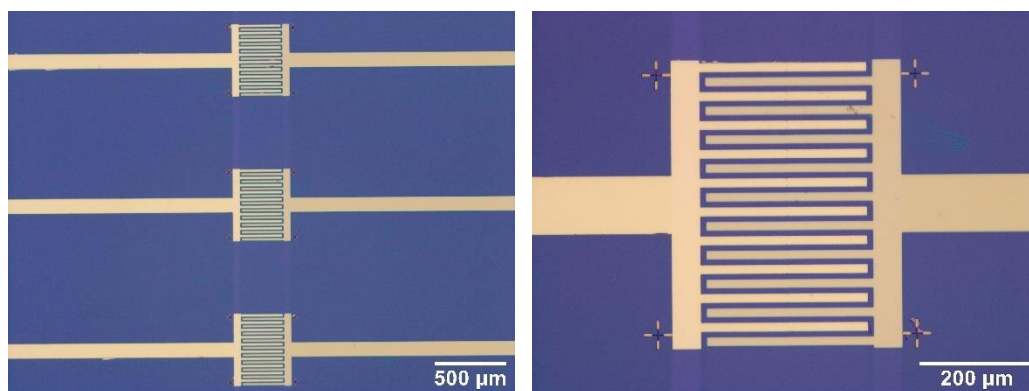
1st metal deposition (post liftoff)



2nd EBL step with 3 point alignment (post-development)

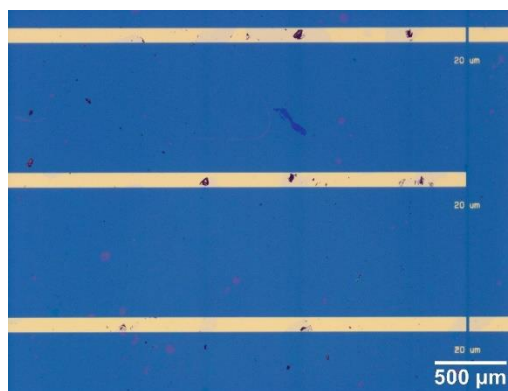
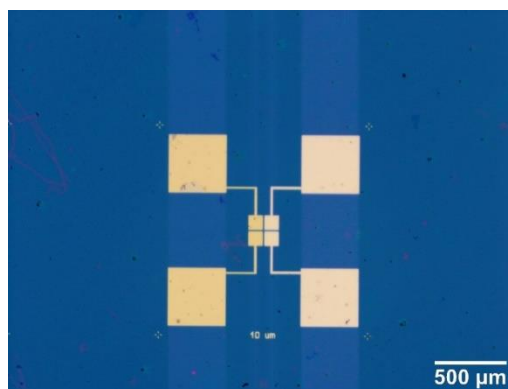
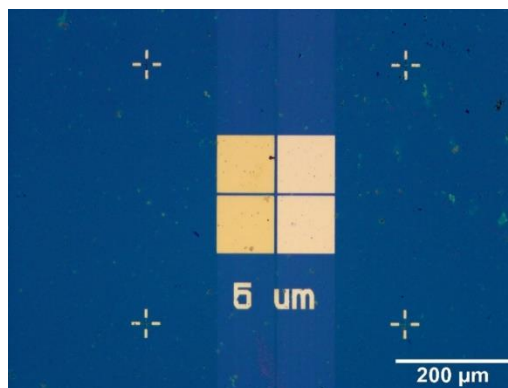


2nd metal deposition (post liftoff)

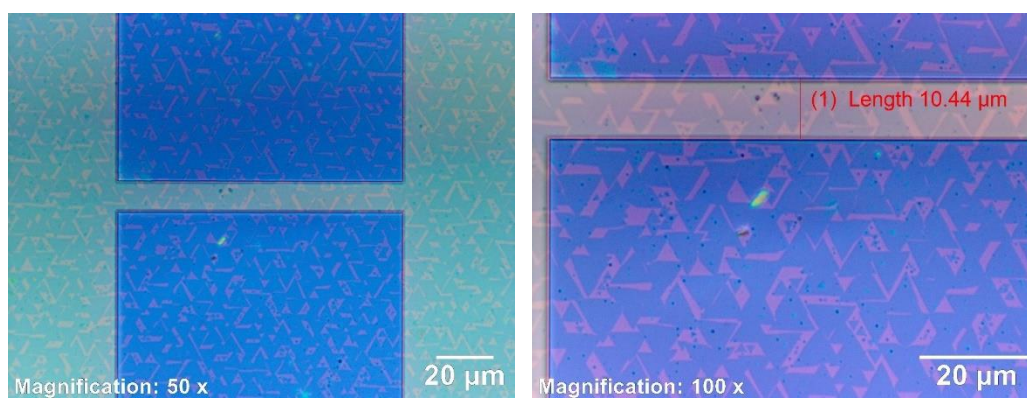
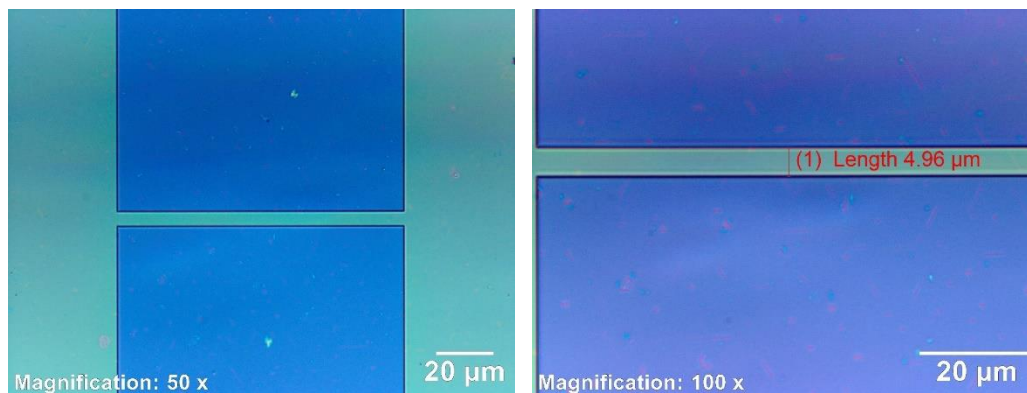


Optical micrographs of various asymmetric-contact devices

In all three of the following micrographs, the left contact pads are Au/Ti and the right contact pads are Pt.

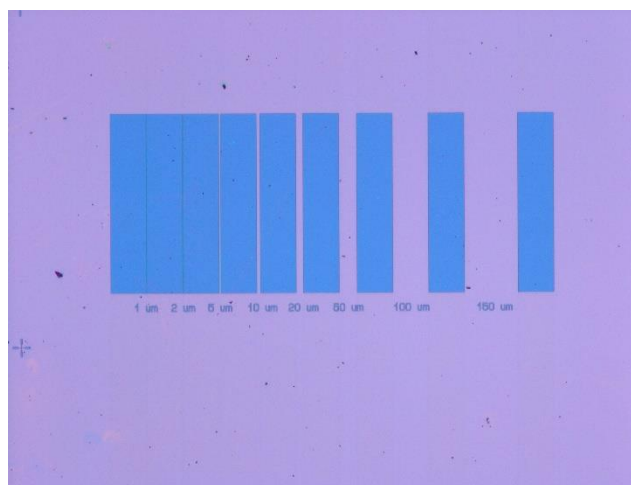


Patterns post-exposure-development showing MoS₂ films (top) vs. MoS₂ flakes (bottom)

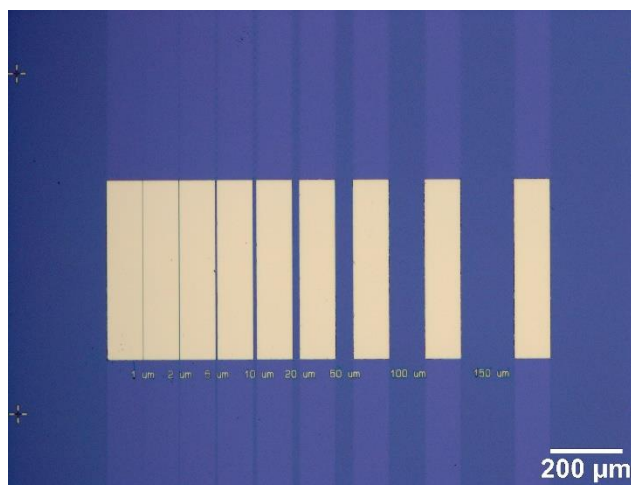


TLM grid fabrication process

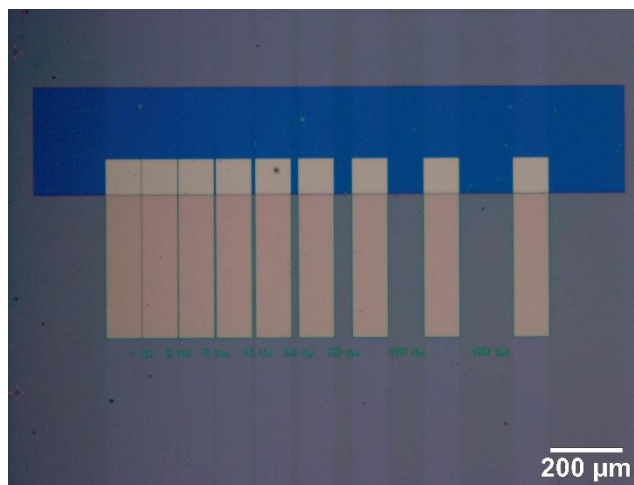
Step 1: Draw patterns using EBL



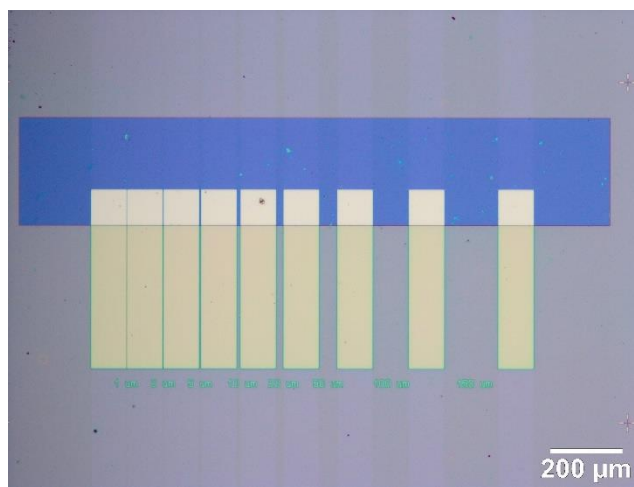
Step 2: Deposit contact metal and transfer MoS₂ on top



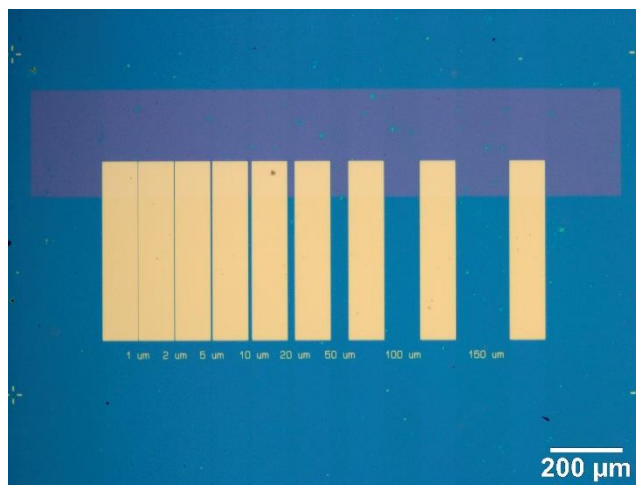
Step 3: 3 point alignment EBL to draw area for MoS₂ etching.



Step 4: Etch MoS₂ from the exposed area using O₂ plasma etching (10 sccm O₂, 500 mTorr, 45 W, 120 seconds)



Step 5: Remove PMMA using acetone and toluene.



APPENDIX B: PUBLICATIONS, PATENTS, AND PRESENTATIONS RELATED TO THIS THESIS

B.1 Publications

K. Islam, T. Ismael, C. Luthy, M. Bush, and M.D. Escarra, “Large-Area Schottky-Barrier Photovoltaics from Two-Dimensional MoS₂,” (in preparation)

K. Islam, R. Synowicki, T. Ismael, I. Oguntoye, N. Grinalds, and M.D. Escarra, “In-Plane and Out-of-Plane Optical Properties of Monolayer, Few-Layer and Thin-Film MoS₂ from 190 to 1700 nm and Their Application in Photonic Device Design,” (in review)

Y. Ji, L. Artzt, W. Adams, C. Spitler, **K. Islam**, D. Codd, and M.D. Escarra, “A Transmissive Solar Module with Cells Directly Cooled by Silicone Oil for Hybrid CPV/T Systems,” (in submission)

D. Codd, M.D. Escarra, B. Riggs, **K. Islam**, Y. Ji, J. Robertson, C. Spitler, J. Platz, N. Gupta, and F. Miller, “Solar Cogeneration of Electricity with High Temperature Process Heat,” *Cell Reports Physical Science*, Vol. 1 (8), (2020). <https://doi.org/10.1016/j.xcrp.2020.100135>

A. Ollanik, G.Z. Hartfield, Y. Ji, J.T. Robertson, **K. Islam**, and M.D. Escarra, “Characterization of Dynamic and Nanoscale Materials and Metamaterials with Continuously-Referenced Interferometry,” *Advanced Optical Materials*, Vol. 7 (24), 1901128 (2019). <https://doi.org/10.1002/adom.201901128>

J. Robertson, D. Blomdahl, **K. Islam**, T. Ismael, M. Woody, J. Failla, M. Johnson, X. Zhang, and M. Escarra. “Rapid-throughput solution-based production of wafer-scale 2D MoS₂,” *Applied Physics Letters*, Vol. 114, 163102 (2019). <https://dx.doi.org/10.1063/1.5093039>

K. Islam, B. Riggs, Y. Ji, J. Robertson, C. Spitler, V. Romanin, D. Codd, and M.D. Escarra, “Transmissive microfluidic active cooling for concentrator photovoltaics,” *Applied Energy*, Vol. 236, 906-915 (2019). <https://doi.org/10.1016/j.apenergy.2018.12.027>

J. Robertson, B. Riggs, **K. Islam**, Y. Ji, C. Spitler, N. Gupta, D. Krut, J. Ermer, F. Miller, D. Codd, and M.D. Escarra. “Field Testing of a Spectrum-Splitting Transmissive

Concentrator Photovoltaic Module.” *Renewable Energy*, **139**, 806-814 (2019). <https://dx.doi.org/10.1016/j.renene.2019.02.117>

Y. Ji, Q. Xu, B. Riggs, **K. Islam**, A. Ollanik, J.H. Ermer, D.D. Krut, V. Romanin, D. Codd, and M.D. Escarra, “Optical Design and Validation of an Infrared Transmissive Spectrum Splitting Concentrator Photovoltaic Module,” *IEEE Journal of Photovoltaics*, Vol. **7** (5), 1469-1478 (2017). <http://dx.doi.org/10.1109/JPHOTOV.2017.2716960>

B.2 Patents

“Direct fluid cooling for a transmissive, concentrated, hybrid, photothermal/ photovoltaic solar system,” M.D. Escarra, D. Codd, **K.M. Islam**, Y. Ji, D.M. Bar-Or, J. Failla, C. Davis, M. Woody, US provisional patent application No. 62/861,769, filed June 14, 2019.

“Transmissive concentrated photovoltaic module with cooling system,” M.D. Escarra, Q. Xu, A. Ollanik, N. Farrar-Foley, Y. Ji, **K. Islam**, B. Riggs, D. Codd, and V. Romanin, US provisional patent application No. 62/314,230, filed March 28, 2016; International patent application No. PCT/US17/24635, filed March 28, 2017.

B.3 Conference Presentations

K. Islam, T. Ismael, R. Synowicki, and M.D. Escarra, “2D Materials-based Optoelectronic Devices,” presented in the virtual *OSA Advanced Photonics Congress* in July 2020.

K. Islam, T. Ismael, N. Grinalds, M. Bush, and M.D. Escarra, “Schottky-Junction Photovoltaics using Asymmetric Contacts on CVD-Grown 2D Materials,” accepted for presentation in *MRS Spring Meeting*, Phoenix, AZ, April 2020 (canceled due to COVID-19).

T. Ismael, **K. Islam**, N. Grinalds, and M.D. Escarra, “Correlative Mapping of Photonic Properties in 2D Semiconductor-Based Optoelectronics,” accepted for presentation in *MRS Spring Meeting*, Phoenix, AZ, April 2020. (canceled due to COVID-19, presented in *MRS Fall Meeting*, Boston, MA in November 2020)

Y. Ji, **K. Islam**, B.C. Riggs, L.E. Artzt, W.L. Adams, J. Failla, D. Bar-Or, N. Gupta, D. Codd, and M.D. Escarra, “A Sunflower Receiver for Hybrid Photovoltaic-Solar Thermal Energy Conversion,” *46th IEEE Photovoltaic Specialists Conference (PVSC)*, Chicago, IL, June 2019.

Y. Ji, **K. Islam**, B.C. Riggs, J. Failla, D. Bar-Or, L.E. Artzt, W.L. Adams, C. Davis, D. Codd, and M.D. Escarra, "Direct Fluid Cooling of Concentrator Photovoltaics for Hybrid Photovoltaic-Solar Thermal Energy Conversion," *46th IEEE Photovoltaic Specialists Conference (PVSC)*, Chicago, IL, June 2019.

K. Islam, J. Robertson, T. Ismael, D. Blomdahl, M. Kothakonda, A. Ollanik, J. Sun, and M.D. Escarra, "2-D MoS₂: Rapid Growth and Advanced Opto-Electronic Devices," *MRS Spring Meeting*, Phoenix, AZ, April 2019.

M.D. Escarra, D. Codd, F. Miller, J. Ermer, V. Romanin, B.C. Riggs, J. Robertson, Y. Ji, **K. Islam**, C. Davis, M. Woody, C.M. Spitler, J.K. Platz, N. Gupta, J. Tubbs, D. Krut, "A Hybrid CPV/T System Featuring Transmissive, Spectrum-Splitting Concentrator Photovoltaics," *7th World Conference on Photovoltaic Energy Conversion (WCPEC) (A Joint Conference of 45th IEEE PVSC, 28th PVSEC & 34th EU PVSEC)*, Waikoloa, HI, June 2018.

J. Robertson, **K. Islam**, M. Woody, J. Failla, J. Wei, M.D. Escarra, "Vertical MoS₂ Optoelectronic Devices Grown on Flexible Molybdenum Foil Bottom-Contacts," *MRS Spring Meeting*, Phoenix, AZ, April 2018.

K. Islam, J. Robertson, M. Woody, J. Failla, J. Wei, and M.D. Escarra, "Dichloroethane Treatment for 50X Enhanced Photocurrent in CVD-Grown Two-Dimensional MoS₂," *MRS Spring Meeting*, Phoenix, AZ, April 2018.

Y. Ji, Q. Xu, B. Riggs, J. Robertson, **K. Islam**, D.D. Krut, J.H. Ermer, and M.D. Escarra, "Transmissive Spectrum-Splitting Concentrator Photovoltaic Cells and Modules," *44th IEEE Photovoltaic Specialists Conference (PVSC)*, Washington, DC, June 2017.

B.C. Riggs, Q. Xu, R. Biedenharn, Y. Ji, **K. Islam**, J. Ermer, D. Krut, V. Romanin, D.S. Codd, F. Miller, and M.D. Escarra, "A Spectrum-Splitting Concentrator Photovoltaic/Thermal System Generating Heat Up to 550°C," *13th International Conference on Concentrator Photovoltaic Systems*, Ottawa, Canada, May 2017.

S.C. Sklare, **K. Islam**, B. Riggs, M.D. Escarra, and D.B. Chrisey, "Excimer Laser Micromachining of Sapphire for Solar Cell Applications," *European MRS Spring Meeting*, Strasbourg, France, May 2017.

J. Robertson, X. Liu, M. Woody, C. Yue, **K. Islam**, J. Wei, and M.D. Escarra, "Precise, Layer-By-Layer Control of MoS₂ Thickness and Properties via Thermal Vapor Sulfurization (TVS)," *MRS Spring Meeting*, Phoenix, AZ, April 2017.

M.D. Escarra, Q. Xu, V. Ji, B. Riggs, A. Ollanik, **K. Islam**, J. Robertson, N. Farrar-Foley, S. Deckhoff-Jones, J. Ermer, D. Krut, V. Romanin, P. Lynn, and D. Codd, "A Hybrid Photovoltaic-Photothermal System Featuring a Spectrum Splitting Concentrated Photovoltaic Module," *12th International Conference on Concentrator Photovoltaic Systems*, Freiburg, Germany, April 2016.

BIBLIOGRAPHY

- (1) K. S. Novoselov, A. K. Geim, S. V. Morozov, D. Jiang, Y. Zhang, S. V. Dubonos, I. V. G. and A. A. F. Electric Field Effect in Atomically Thin Carbon Films. *Science* (80-.). **2004**, 306 (5696), 666–669.
- (2) Frindt, R. F. Single Crystals of MoS₂ Several Molecular Layers Thick. *J. Appl. Phys.* **1966**. <https://doi.org/10.1063/1.1708627>.
- (3) Miró, P.; Audiffred, M.; Heine, T. An Atlas of Two-Dimensional Materials. *Chemical Society Reviews*. 2014. <https://doi.org/10.1039/c4cs00102h>.
- (4) Geim, A. K.; Grigorieva, I. V. Van Der Waals Heterostructures. *Nature* **2014**, 499 (7459), 419–425. <https://doi.org/10.1038/nature12385>.
- (5) Mak, K. F.; Lee, C.; Hone, J.; Shan, J.; Heinz, T. F. Atomically Thin MoS₂: A New Direct-Gap Semiconductor. *Phys. Rev. Lett.* **2010**, 105 (13), 2–5. <https://doi.org/10.1103/PhysRevLett.105.136805>.
- (6) Splendiani, A.; Sun, L.; Zhang, Y.; Li, T.; Kim, J.; Chim, C. Y.; Galli, G.; Wang, F. Emerging Photoluminescence in Monolayer MoS₂. *Nano Lett.* **2010**, 10 (4), 1271–1275.
- (7) Gusakova, J.; Wang, X.; Shiao, L. L.; Krivosheeva, A.; Shaposhnikov, V.; Borisenko, V.; Gusakov, V.; Tay, B. K. Electronic Properties of Bulk and Monolayer TMDs: Theoretical Study Within DFT Framework (GVJ-2e Method). *Phys. Status Solidi Appl. Mater. Sci.* **2017**. <https://doi.org/10.1002/pssa.201700218>.

- (8) Huang, H. H.; Fan, X.; Singh, D. J.; Zheng, W. T. Recent Progress of TMD Nanomaterials: Phase Transitions and Applications. *Nanoscale*. 2020. <https://doi.org/10.1039/c9nr08313h>.
- (9) Mueller, T.; Malic, E. Exciton Physics and Device Application of Two-Dimensional Transition Metal Dichalcogenide Semiconductors. *npj 2D Materials and Applications*. 2018. <https://doi.org/10.1038/s41699-018-0074-2>.
- (10) RadisavljevicB; RadenovicA; BrivioJ; GiacomettiV; KisA; Radisavljevic, B.; Radenovic, A.; Brivio, J.; Giacometti, V.; Kis, A. Single-Layer MoS₂ Transistors. *Nat Nano* **2011**, *6* (3), 147–150. <https://doi.org/http://www.nature.com/nnano/journal/v6/n3/abs/nnano.2010.279.html#supplementary-information>.
- (11) Cui, X.; Lee, G. H.; Kim, Y. D.; Arefe, G.; Huang, P. Y.; Lee, C. H.; Chenet, D. A.; Zhang, X.; Wang, L.; Ye, F.; Pizzocchero, F.; Jessen, B. S.; Watanabe, K.; Taniguchi, T.; Muller, D. A.; Low, T.; Kim, P.; Hone, J. Multi-Terminal Transport Measurements of MoS₂ Using a van Der Waals Heterostructure Device Platform. *Nat. Nanotechnol.* **2015**. <https://doi.org/10.1038/nnano.2015.70>.
- (12) Lopez-Sanchez, O.; Lembke, D.; Kayci, M.; Radenovic, A.; Kis, A. Ultrasensitive Photodetectors Based on Monolayer MoS₂. *Nat. Nanotechnol.* **2013**. <https://doi.org/10.1038/nnano.2013.100>.
- (13) Bernardi, M.; Palummo, M.; Grossman, J. C. Photovoltaics Using Two-Dimensional Monolayer Materials Extraordinary Sunlight Absorption and 1 Nm-Thick

- Photovoltaics Using Two-Dimensional Monolayer Materials. *Nano Lett.* **2013**, 1–10. <https://doi.org/10.1021/nl401544y>.
- (14) Luque, A.; Hegedus, S. *Handbook of Photovoltaic Science and Engineering*; 2011. <https://doi.org/10.1002/9780470974704>.
- (15) Green, M. A.; Hishikawa, Y.; Warta, W.; Dunlop, E. D.; Levi, D. H.; Hohl-Ebinger, J.; Ho-Baillie, A. W. H. Solar Cell Efficiency Tables (Version 50). *Prog. Photovoltaics Res. Appl.* **2017**. <https://doi.org/10.1002/pip.2909>.
- (16) Barlev, D.; Vidu, R.; Stroeve, P. Innovation in Concentrated Solar Power. *Solar Energy Materials and Solar Cells.* 2011. <https://doi.org/10.1016/j.solmat.2011.05.020>.
- (17) Tian, Y.; Zhao, C. Y. A Review of Solar Collectors and Thermal Energy Storage in Solar Thermal Applications. *Appl. Energy* **2013**. <https://doi.org/10.1016/j.apenergy.2012.11.051>.
- (18) Chow, T. T. A Review on Photovoltaic/Thermal Hybrid Solar Technology. *Applied Energy.* 2010. <https://doi.org/10.1016/j.apenergy.2009.06.037>.
- (19) Ji, Y.; Xu, Q.; Riggs, B.; Islam, K.; Ollanik, A.; Ermer, J. H.; Krut, D. D.; Romanin, V.; Codd, D.; Escarra, M. D. Optical Design and Validation of an Infrared Transmissive Spectrum Splitting Concentrator Photovoltaic Module. *IEEE J. Photovoltaics* **2017**. <https://doi.org/10.1109/JPHOTOV.2017.2716960>.
- (20) Escarra, M. D.; Codd, D.; Miller, F.; Ermer, J.; Romanin, V.; Riggs, B. C.;

- Robertson, J.; Ji, Y.; Islam, K.; Davis, C.; Woody, M.; Spitler, C. M.; Platz, J. K.; Gupta, N.; Tubbs, J.; Krut, D. A Hybrid CPV/T System Featuring Transmissive, Spectrum-Splitting Concentrator Photovoltaics. In *2018 IEEE 7th World Conference on Photovoltaic Energy Conversion, WCPEC 2018 - A Joint Conference of 45th IEEE PVSC, 28th PVSEC and 34th EU PVSEC*; 2018. <https://doi.org/10.1109/PVSC.2018.8547930>.
- (21) Xu, Q.; Ji, Y.; Krut, D. D.; Ermer, J. H.; Escarra, M. D. Transmissive Concentrator Multijunction Solar Cells with over 47% In-Band Power Conversion Efficiency. *Appl. Phys. Lett.* **2016**. <https://doi.org/10.1063/1.4967376>.
- (22) Helmers, H.; Schachtner, M.; Bett, A. W. Influence of Temperature and Irradiance on Triple-Junction Solar Subcells. *Sol. Energy Mater. Sol. Cells* **2013**. <https://doi.org/10.1016/j.solmat.2013.03.039>.
- (23) Do, K. H.; Kim, T. H.; Han, Y. S.; Choi, B. Il; Kim, M. B. General Correlation of a Natural Convective Heat Sink with Plate-Fins for High Concentrating Photovoltaic Module Cooling. *Sol. Energy* **2012**. <https://doi.org/10.1016/j.solener.2012.06.010>.
- (24) Wang, Y. N.; Lin, T. T.; Leong, J. C.; Hsu, Y. T.; Yeh, C. P.; Lee, P. H.; Tsai, C. H. Numerical Investigation of High-Concentration Photovoltaic Module Heat Dissipation. *Renew. Energy* **2013**. <https://doi.org/10.1016/j.renene.2012.06.016>.
- (25) Chenlo, F.; Cid, M. A Linear Concentrator Photovoltaic Module: Analysis of Non-Uniform Illumination and Temperature Effects on Efficiency. *Sol. Cells* **1987**. [https://doi.org/10.1016/0379-6787\(87\)90018-4](https://doi.org/10.1016/0379-6787(87)90018-4).

- (26) Shukla, A.; Kant, K.; Sharma, A.; Biwole, P. H. Cooling Methodologies of Photovoltaic Module for Enhancing Electrical Efficiency: A Review. *Sol. Energy Mater. Sol. Cells* **2017**. <https://doi.org/10.1016/j.solmat.2016.10.047>.
- (27) Gilmore, N.; Timchenko, V.; Menictas, C. Microchannel Cooling of Concentrator Photovoltaics: A Review. *Renewable and Sustainable Energy Reviews*. 2018. <https://doi.org/10.1016/j.rser.2018.04.010>.
- (28) Royne, A.; Dey, C. J.; Mills, D. R. Cooling of Photovoltaic Cells under Concentrated Illumination: A Critical Review. *Sol. Energy Mater. Sol. Cells* **2005**. <https://doi.org/10.1016/j.solmat.2004.09.003>.
- (29) Radwan, A.; Ahmed, M. The Influence of Microchannel Heat Sink Configurations on the Performance of Low Concentrator Photovoltaic Systems. *Appl. Energy* **2017**. <https://doi.org/10.1016/j.apenergy.2017.08.202>.
- (30) Micheli, L.; Fernández, E. F.; Almonacid, F.; Mallick, T. K.; Smestad, G. P. Performance, Limits and Economic Perspectives for Passive Cooling of High Concentrator Photovoltaics. *Sol. Energy Mater. Sol. Cells* **2016**. <https://doi.org/10.1016/j.solmat.2016.04.016>.
- (31) Di Capua H, M.; Escobar, R.; Diaz, A. J.; Guzmán, A. M. Enhancement of the Cooling Capability of a High Concentration Photovoltaic System Using Microchannels with Forward Triangular Ribs on Sidewalls. *Appl. Energy* **2018**. <https://doi.org/10.1016/j.apenergy.2018.05.052>.
- (32) Plechinger, G.; Mann, J.; Preciado, E.; Barroso, D.; Nguyen, A.; Eroms, J.; Schüller,

- C.; Bartels, L.; Korn, T. A Direct Comparison of CVD-Grown and Exfoliated MoS₂ Using Optical Spectroscopy. *Semicond. Sci. Technol.* **2014**, *29* (6). <https://doi.org/10.1088/0268-1242/29/6/064008>.
- (33) Li, H.; Li, Y.; Aljarb, A.; Shi, Y.; Li, L. J. Epitaxial Growth of Two-Dimensional Layered Transition-Metal Dichalcogenides: Growth Mechanism, Controllability, and Scalability. *Chem. Rev.* **2018**, *118* (13), 6134–6150. <https://doi.org/10.1021/acs.chemrev.7b00212>.
- (34) Wang, S.; Rong, Y.; Fan, Y.; Pacios, M.; Bhaskaran, H.; He, K.; Warner, J. H. Shape Evolution of Monolayer MoS₂ Crystals Grown by Chemical Vapor Deposition. *Chem. Mater.* **2014**, *26* (22), 6371–6379. <https://doi.org/10.1021/cm5025662>.
- (35) Robertson, J.; Liu, X.; Yue, C.; Escarra, M.; Wei, J. Wafer-Scale Synthesis of Monolayer and Few-Layer MoS₂ via Thermal Vapor Sulfurization. *2D Mater.* **2017**, *4* (4). <https://doi.org/10.1088/2053-1583/aa8678>.
- (36) Li, Y.; Chernikov, A.; Zhang, X.; Rigosi, A.; Hill, H. M.; Van Der Zande, A. M.; Chenet, D. A.; Shih, E. M.; Hone, J.; Heinz, T. F. Measurement of the Optical Dielectric Function of Monolayer Transition-Metal Dichalcogenides: MoS₂, MoS₂, WS₂, and WS₂. *Phys. Rev. B - Condens. Matter Mater. Phys.* **2014**, *90* (20), 1–6. <https://doi.org/10.1103/PhysRevB.90.205422>.
- (37) Li, H.; Zhang, Q.; Yap, C. C. R.; Tay, B. K.; Edwin, T. H. T.; Olivier, A.; Baillargeat, D. From Bulk to Monolayer MoS₂: Evolution of Raman Scattering. *Adv. Funct. Mater.* **2012**, *22* (7), 1385–1390.

<https://doi.org/10.1002/adfm.201102111>.

- (38) Song, B.; Gu, H.; Fang, M.; Chen, X.; Jiang, H.; Wang, R.; Zhai, T.; Ho, Y. T.; Liu, S. Layer-Dependent Dielectric Function of Wafer-Scale 2D MoS₂. *Adv. Opt. Mater.* **2019**. <https://doi.org/10.1002/adom.201801250>.
- (39) Shen, C. C.; Hsu, Y. Te; Li, L. J.; Liu, H. L. Charge Dynamics and Electronic Structures of Monolayer MoS₂ Films Grown by Chemical Vapor Deposition. *Appl. Phys. Express* **2013**, *6* (12), 8–12. <https://doi.org/10.7567/APEX.6.125801>.
- (40) Liu, H. L.; Shen, C. C.; Su, S. H.; Hsu, C. L.; Li, M. Y.; Li, L. J. Optical Properties of Monolayer Transition Metal Dichalcogenides Probed by Spectroscopic Ellipsometry. *Appl. Phys. Lett.* **2014**, *105* (20). <https://doi.org/10.1063/1.4901836>.
- (41) Yim, C.; O'Brien, M.; McEvoy, N.; Winters, S.; Mirza, I.; Lunney, J. G.; Duesberg, G. S. Investigation of the Optical Properties of MoS₂ Thin Films Using Spectroscopic Ellipsometry. *Appl. Phys. Lett.* **2014**, *104* (10). <https://doi.org/10.1063/1.4868108>.
- (42) Li, D.; Song, X.; Xu, J.; Wang, Z.; Zhang, R.; Zhou, P.; Zhang, H.; Huang, R.; Wang, S.; Zheng, Y.; Zhang, D. W.; Chen, L. Optical Properties of Thickness-Controlled MoS₂ Thin Films Studied by Spectroscopic Ellipsometry. *Appl. Surf. Sci.* **2017**, *421*, 884–890. <https://doi.org/10.1016/j.apsusc.2016.09.069>.
- (43) Park, J. W.; So, H. S.; Kim, S.; Choi, S. H.; Lee, H.; Lee, J.; Lee, C.; Kim, Y. Optical Properties of Large-Area Ultrathin MoS₂ Films: Evolution from a Single Layer to Multilayers. *J. Appl. Phys.* **2014**, *116* (18). <https://doi.org/10.1063/1.4901464>.

- (44) Ermolaev, G. A.; Stebunov, Y. V.; Vyshnevyy, A. A.; Tatarkin, D. E.; Yakubovsky, D. I.; Novikov, S. M.; Baranov, D. G.; Shegai, T.; Nikitin, A. Y.; Arsenin, A. V.; Volkov, V. S. Broadband Optical Properties of Monolayer and Bulk MoS₂. *npj 2D Mater. Appl.* **2020**, *4* (1). <https://doi.org/10.1038/s41699-020-0155-x>.
- (45) Tompkins, H. G.; McGahan, W. A. *Spectroscopic Ellipsometry and Reflectometry*; John Wiley and Sons, Ltd.: New York, 1999.
- (46) Tompkins, H. G.; Irene, E. A. *Handbook of Ellipsometry*; William Andrew Publishing, 2005. <https://doi.org/10.1515/arh-2005-0022>.
- (47) Fujiwara, H. *Spectroscopic Ellipsometry: Principles and Applications*; 2007. <https://doi.org/10.1002/9780470060193>.
- (48) Gurarlan, A.; Yu, Y.; Su, L.; Yu, Y.; Suarez, F.; Yao, S.; Zhu, Y.; Ozturk, M.; Zhang, Y.; Cao, L. Surface-Energy-Assisted Perfect Transfer of Centimeter-Scale Monolayer and Few-Layer MoS₂ Films onto Arbitrary Substrates. *ACS Nano* **2014**, *8* (11), 11522–11528. <https://doi.org/10.1021/nn5057673>.
- (49) Robertson, J.; Blomdahl, D.; Islam, K.; Ismael, T.; Woody, M.; Failla, J.; Johnson, M.; Zhang, X.; Escarra, M. Rapid-Throughput Solution-Based Production of Wafer-Scale 2D MoS₂. *Appl. Phys. Lett.* **2019**. <https://doi.org/10.1063/1.5093039>.
- (50) Herzinger, C. M.; Johs, B.; McGahan, W. A.; Woollam, J. A.; Paulson, W. Ellipsometric Determination of Optical Constants for Silicon and Thermally Grown Silicon Dioxide via a Multi-Sample, Multi-Wavelength, Multi-Angle Investigation. *J. Appl. Phys.* **1998**, *83* (6), 3323–3336. <https://doi.org/10.1063/1.367101>.

- (51) McGahan, W. A.; Johs, B.; Woollam, J. A. Techniques for Ellipsometric Measurement of the Thickness and Optical Constants of Thin Absorbing Films. *Thin Solid Films* **1993**, *234* (1–2), 443–446. [https://doi.org/10.1016/0040-6090\(93\)90303-7](https://doi.org/10.1016/0040-6090(93)90303-7).
- (52) Johs, B. D.; McGahan, W. A.; Woollam, J. A. Optical Analysis of Complex Multilayer Structures Using Multiple Data Types. *Thin Solid Films* **1994**, *253* (1–2), 25–27. [https://doi.org/10.1016/0040-6090\(94\)90288-7](https://doi.org/10.1016/0040-6090(94)90288-7).
- (53) Hilfiker, J. N.; Singh, N.; Tiwald, T.; Convey, D.; Smith, S. M.; Baker, J. H.; Tompkins, H. G. Survey of Methods to Characterize Thin Absorbing Films with Spectroscopic Ellipsometry. *Thin Solid Films* **2008**, *516* (22), 7979–7989. <https://doi.org/10.1016/j.tsf.2008.04.060>.
- (54) Fujiwara, H.; Collins, R. W. *Spectroscopic Ellipsometry for Photovoltaics Volume 2: Fundamental Principles and Solar Cell Characterization*; 2018.
- (55) Hong, N.; Synowicki, R. A.; Hilfiker, J. N. Mueller Matrix Characterization of Flexible Plastic Substrates. *Appl. Surf. Sci.* **2017**. <https://doi.org/10.1016/j.apsusc.2017.01.276>.
- (56) Li, G.; Suja, M.; Chen, M.; Bekyarova, E.; Haddon, R. C.; Liu, J.; Itkis, M. E. Visible-Blind UV Photodetector Based on Single-Walled Carbon Nanotube Thin Film/ZnO Vertical Heterostructures. *ACS Appl. Mater. Interfaces* **2017**, *9* (42), 37094–37104. <https://doi.org/10.1021/acsami.7b07765>.
- (57) Cho, A. J.; Song, M. K.; Kang, D. W.; Kwon, J. Y. Two-Dimensional WSe₂/MoS₂

- p-n Heterojunction-Based Transparent Photovoltaic Cell and Its Performance Enhancement by Fluoropolymer Passivation. *ACS Appl. Mater. Interfaces* **2018**, *10* (42), 35972–35977. <https://doi.org/10.1021/acsami.8b12250>.
- (58) Eda, G.; Yamaguchi, H.; Voiry, D.; Fujita, T.; Chen, M.; Chhowalla, M. Photoluminescence from Chemically Exfoliated MoS₂. *Nano Lett.* **2011**. <https://doi.org/10.1021/nl201874w>.
- (59) Troparevsky, M. C.; Sabau, A. S.; Lupini, A. R.; Zhang, Z. Transfer-Matrix Formalism for the Calculation of Optical Response in Multilayer Systems: From Coherent to Incoherent Interference. *Opt. Express* **2010**, *18* (24), 24715. <https://doi.org/10.1364/oe.18.024715>.
- (60) Katsidis, C. C.; Siapkas, D. I. Systems With Coherent , Partially Coherent , and Incoherent Interference. *Appl. Opt.* **2002**, *41* (19), 3978–3987.
- (61) Burkhard, G. F.; Hoke, E. T.; McGehee, M. D. Accounting for Interference, Scattering, and Electrode Absorption to Make Accurate Internal Quantum Efficiency Measurements in Organic and Other Thin Solar Cells. *Adv. Mater.* **2010**, *22* (30), 3293–3297. <https://doi.org/10.1002/adma.201000883>.
- (62) Pettersson, L. A. A.; Roman, L. S.; Inganäs, O. Modeling Photocurrent Action Spectra of Photovoltaic Devices Based on Organic Thin Films. *J. Appl. Phys.* **1999**, *86* (1), 487–496. <https://doi.org/10.1063/1.370757>.
- (63) Lu, H.; Gan, X.; Mao, D.; Fan, Y.; Yang, D.; Zhao, J. Nearly Perfect Absorption of Light in Monolayer Molybdenum Disulfide Supported by Multilayer Structures.

Opt. Express **2017**, 25 (18), 21630. <https://doi.org/10.1364/oe.25.021630>.

- (64) Chhowalla, M.; Jena, D.; Zhang, H. Two-Dimensional Semiconductors for Transistors. *Nat. Rev. Mater.* **2016**, 1 (716), 16052. <https://doi.org/10.1038/natrevmats.2016.52>.
- (65) Long, M.; Wang, P.; Fang, H.; Hu, W. Progress, Challenges, and Opportunities for 2D Material Based Photodetectors. *Advanced Functional Materials*. 2019. <https://doi.org/10.1002/adfm.201803807>.
- (66) Yan, F.; Wei, Z.; Wei, X.; Lv, Q.; Zhu, W.; Wang, K. Toward High-Performance Photodetectors Based on 2D Materials: Strategy on Methods. *Small Methods* **2018**. <https://doi.org/10.1002/smt.201700349>.
- (67) Britnell, L.; Ribeiro, R. M.; Eckmann, A.; Jalil, R.; Belle, B. D.; Mishchenko, A.; Kim, Y. J.; Gorbachev, R. V.; Georgiou, T.; Morozov, S. V.; Grigorenko, A. N.; Geim, A. K.; Casiraghi, C.; Castro Neto, A. H.; Novoselov, K. S. Strong Light-Matter Interactions in Heterostructures of Atomically Thin Films. *Science* (80-.). **2013**. <https://doi.org/10.1126/science.1235547>.
- (68) Roy, K.; Padmanabhan, M.; Goswami, S.; Sai, T. P.; Ramalingam, G.; Raghavan, S.; Ghosh, A. Graphene-MoS₂ Hybrid Structures for Multifunctional Photoresponsive Memory Devices. *Nat. Nanotechnol.* **2013**. <https://doi.org/10.1038/nnano.2013.206>.
- (69) Zhang, W.; Chuu, C. P.; Huang, J. K.; Chen, C. H.; Tsai, M. L.; Chang, Y. H.; Liang, C. Te; Chen, Y. Z.; Chueh, Y. L.; He, J. H.; Chou, M. Y.; Li, L. J. Ultrahigh-Gain

- Photodetectors Based on Atomically Thin Graphene-MoS₂ Heterostructures. *Sci. Rep.* **2015**. <https://doi.org/10.1038/srep03826>.
- (70) Tong, X.; Ashalley, E.; Lin, F.; Li, H.; Wang, Z. M. Advances in MoS₂-Based Field Effect Transistors (FETs). *Nano-Micro Lett.* **2015**, *7* (3), 203–218. <https://doi.org/10.1007/s40820-015-0034-8>.
- (71) Leong, W. S.; Li, Y.; Luo, X.; Nai, C. T.; Quek, S. Y.; Thong, J. T. L. Tuning the Threshold Voltage of MoS₂ Field-Effect Transistors via Surface Treatment. *Nanoscale* **2015**. <https://doi.org/10.1039/c5nr00253b>.
- (72) Li, N.; Wang, Q.; Shen, C.; Wei, Z.; Yu, H.; Zhao, J.; Lu, X.; Wang, G.; He, C.; Xie, L.; Zhu, J.; Du, L.; Yang, R.; Shi, D.; Zhang, G. Large-Scale Flexible and Transparent Electronics Based on Monolayer Molybdenum Disulfide Field-Effect Transistors. *Nat. Electron.* **2020**. <https://doi.org/10.1038/s41928-020-00475-8>.
- (73) Kc, S.; Longo, R. C.; Addou, R.; Wallace, R. M.; Cho, K. Impact of Intrinsic Atomic Defects on the Electronic Structure of MoS₂ Monolayers. *Nanotechnology* **2014**. <https://doi.org/10.1088/0957-4484/25/37/375703>.
- (74) Yang, L.; Majumdar, K.; Du, Y.; Liu, H.; Wu, H.; Hatzistergos, M.; Hung, P. Y.; Tieckelmann, R.; Tsai, W.; Hobbs, C.; Ye, P. D. High-Performance MoS₂ Field-Effect Transistors Enabled by Chloride Doping: Record Low Contact Resistance (0.5 K Ω · μ m) and Record High Drain Current (460 Ma/Mm). In *Digest of Technical Papers - Symposium on VLSI Technology*; 2014. <https://doi.org/10.1109/VLSIT.2014.6894432>.

- (75) Singh, E.; Singh, P.; Kim, K. S.; Yeom, G. Y.; Nalwa, H. S. Flexible Molybdenum Disulfide (MoS₂) Atomic Layers for Wearable Electronics and Optoelectronics. *ACS Applied Materials and Interfaces*. 2019. <https://doi.org/10.1021/acsami.8b19859>.
- (76) Wang, L.; Huang, L.; Tan, W. C.; Feng, X.; Chen, L.; Huang, X.; Ang, K.-W. 2D Photovoltaic Devices: Progress and Prospects. *Small Methods* **2018**. <https://doi.org/10.1002/smtd.201700294>.
- (77) Singh, E.; Kim, K. S.; Yeom, G. Y.; Nalwa, H. S. Atomically Thin-Layered Molybdenum Disulfide (MoS₂) for Bulk-Heterojunction Solar Cells. *ACS Appl. Mater. Interfaces* **2017**. <https://doi.org/10.1021/acsami.6b13582>.
- (78) Jariwala, D.; Davoyan, A. R.; Wong, J.; Atwater, H. A. Van Der Waals Materials for Atomically-Thin Photovoltaics: Promise and Outlook. *ACS Photonics*. 2017. <https://doi.org/10.1021/acsp Photonics.7b01103>.
- (79) Fontana, M.; Deppe, T.; Boyd, A. K.; Rinzan, M.; Liu, A. Y.; Paranjape, M.; Barbara, P. Electron-Hole Transport and Photovoltaic Effect in Gated MoS₂ Schottky Junctions. *Sci. Rep.* **2013**, 3, 1634. <https://doi.org/10.1038/srep01634>.
- (80) Choi, M. S.; Qu, D.; Lee, D.; Liu, X.; Watanabe, K.; Taniguchi, T.; Yoo, W. J. Lateral MoS₂ P-n Junction Formed by Chemical Doping for Use in High-Performance Optoelectronics. *ACS Nano* **2014**. <https://doi.org/10.1021/nn503284n>.
- (81) Wi, S.; Kim, H.; Chen, M.; Nam, H.; Guo, L. J.; Meyhofer, E.; Liang, X. Enhancement of Photovoltaic Response in Multilayer MoS₂ Induced by Plasma

- Doping. *ACS Nano* **2014**. <https://doi.org/10.1021/nn5013429>.
- (82) Went, C. M.; Wong, J.; Jahelka, P. R.; Kelzenberg, M.; Biswas, S.; Hunt, M. S.; Carbone, A.; Atwater, H. A. A New Metal Transfer Process for van Der Waals Contacts to Vertical Schottky-Junction Transition Metal Dichalcogenide Photovoltaics. *Sci. Adv.* **2019**. <https://doi.org/10.1126/sciadv.aax6061>.
- (83) Nelson, J. *The Physics of Solar Cells*; 2003. <https://doi.org/10.1142/p276>.
- (84) Bouzidi, K.; Chegaar, M.; Bouhemadou, A. Solar Cells Parameters Evaluation Considering the Series and Shunt Resistance. *Sol. Energy Mater. Sol. Cells* **2007**. <https://doi.org/10.1016/j.solmat.2007.05.019>.
- (85) Jain, A.; Kapoor, A. Exact Analytical Solutions of the Parameters of Real Solar Cells Using Lambert W-Function. *Sol. Energy Mater. Sol. Cells* **2004**. <https://doi.org/10.1016/j.solmat.2003.11.018>.
- (86) Cho, A. J.; Kwon, J. Y. Hexagonal Boron Nitride for Surface Passivation of Two-Dimensional van Der Waals Heterojunction Solar Cells. *ACS Appl. Mater. Interfaces* **2019**. <https://doi.org/10.1021/acsami.9b11219>.
- (87) Schroder, D. K. *Semiconductor Material and Device Characterization: Third Edition*; 2005. <https://doi.org/10.1002/0471749095>.
- (88) Schroder, D. K.; Meier, D. L. Solar Cell Contact Resistance—A Review. *IEEE Trans. Electron Devices* **1984**. <https://doi.org/10.1109/T-ED.1984.21583>.
- (89) Baca, A. G.; Ren, F.; Zolper, J. C.; Briggs, R. D.; Pearton, S. J. A Survey of Ohmic

- Contacts to III-V Compound Semiconductors. *Thin Solid Films* **1997**.
[https://doi.org/10.1016/S0040-6090\(97\)00439-2](https://doi.org/10.1016/S0040-6090(97)00439-2).
- (90) Ballif, C.; De Wolf, S.; Descoeurdes, A.; Holman, Z. C. Amorphous Silicon/Crystalline Silicon Heterojunction Solar Cells. In *Semiconductors and Semimetals*; 2014. <https://doi.org/10.1016/B978-0-12-388417-6.00003-9>.
- (91) Wang, S. Y.; Ko, T. S.; Huang, C. C.; Lin, D. Y.; Huang, Y. S. Optical and Electrical Properties of MoS₂ and Fe-Doped MoS₂. In *Japanese Journal of Applied Physics*; 2014. <https://doi.org/10.7567/JJAP.53.04EH07>.
- (92) Chen, Y.; Huang, S.; Ji, X.; Adepalli, K.; Yin, K.; Ling, X.; Wang, X.; Xue, J.; Dresselhaus, M.; Kong, J.; Yildiz, B. Tuning Electronic Structure of Single Layer MoS₂ through Defect and Interface Engineering. *ACS Nano* **2018**.
<https://doi.org/10.1021/acsnano.7b08418>.
- (93) Laturia, A.; Van de Put, M. L.; Vandenberghe, W. G. Dielectric Properties of Hexagonal Boron Nitride and Transition Metal Dichalcogenides: From Monolayer to Bulk. *npj 2D Mater. Appl.* **2018**. <https://doi.org/10.1038/s41699-018-0050-x>.
- (94) Kc, S.; Longo, R. C.; Wallace, R. M.; Cho, K. Computational Study of MoS₂/HfO₂ Defective Interfaces for Nanometer-Scale Electronics. *ACS Omega* **2017**.
<https://doi.org/10.1021/acsomega.7b00636>.
- (95) Flöry, N.; Jain, A.; Bharadwaj, P.; Parzefall, M.; Taniguchi, T.; Watanabe, K.; Novotny, L. A WSe₂/MoSe₂ Heterostructure Photovoltaic Device. *Appl. Phys. Lett.* **2015**. <https://doi.org/10.1063/1.4931621>.

- (96) Xu, Q.; Ji, Y.; Riggs, B.; Ollanik, A.; Farrar-Foley, N.; Ermer, J. H.; Romanin, V.; Lynn, P.; Codd, D.; Escarra, M. D. A Transmissive, Spectrum-Splitting Concentrating Photovoltaic Module for Hybrid Photovoltaic-Solar Thermal Energy Conversion. *Sol. Energy* **2016**. <https://doi.org/10.1016/j.solener.2016.08.057>.
- (97) Palavras, I.; Bakos, G. C. Development of a Low-Cost Dish Solar Concentrator and Its Application in Zeolite Desorption. *Renew. Energy* **2006**. <https://doi.org/10.1016/j.renene.2005.11.007>.
- (98) Tripanagnostopoulos, Y.; Nousia, T.; Souliotis, M.; Yianoulis, P. Hybrid Photovoltaic/Thermal Solar Systems. *Sol. Energy* **2002**. [https://doi.org/10.1016/S0038-092X\(01\)00096-2](https://doi.org/10.1016/S0038-092X(01)00096-2).
- (99) Zakharchenko, R.; Licea-Jiménez, L.; Pérez-García, S. A.; Vorobiev, P.; Dehesa-Carrasco, U.; Pérez-Robles, J. F.; González-Hernández, J.; Vorobiev, Y. Photovoltaic Solar Panel for a Hybrid PV/Thermal System. In *Solar Energy Materials and Solar Cells*; 2004. <https://doi.org/10.1016/j.solmat.2004.01.022>.
- (100) Otanicar, T. P.; Theisen, S.; Norman, T.; Tyagi, H.; Taylor, R. A. Envisioning Advanced Solar Electricity Generation: Parametric Studies of CPV/T Systems with Spectral Filtering and High Temperature PV. *Appl. Energy* **2015**. <https://doi.org/10.1016/j.apenergy.2014.11.073>.
- (101) Rezania, A.; Rosendahl, L. A. Feasibility and Parametric Evaluation of Hybrid Concentrated Photovoltaic-Thermoelectric System. *Appl. Energy* **2017**. <https://doi.org/10.1016/j.apenergy.2016.11.064>.

- (102) Looser, R.; Vivar, M.; Everett, V. Spectral Characterisation and Long-Term Performance Analysis of Various Commercial Heat Transfer Fluids (HTF) as Direct-Absorption Filters for CPV-T Beam-Splitting Applications. *Appl. Energy* **2014**. <https://doi.org/10.1016/j.apenergy.2013.09.001>.
- (103) Mojiri, A.; Stanley, C.; Taylor, R. A.; Kalantar-Zadeh, K.; Rosengarten, G. A Spectrally Splitting Photovoltaic-Thermal Hybrid Receiver Utilising Direct Absorption and Wave Interference Light Filtering. *Sol. Energy Mater. Sol. Cells* **2015**. <https://doi.org/10.1016/j.solmat.2015.03.011>.
- (104) Ju, X.; Xu, C.; Hu, Y.; Han, X.; Wei, G.; Du, X. A Review on the Development of Photovoltaic/Concentrated Solar Power (PV-CSP) Hybrid Systems. *Sol. Energy Mater. Sol. Cells* **2017**. <https://doi.org/10.1016/j.solmat.2016.12.004>.
- (105) Gross, H.; Blechinger, F.; Aichtner, B. *Handbook of Optical Systems*; 2015. <https://doi.org/10.1002/9783527699247>.
- (106) WM, H. *Handbook of Chemistry and Physics, 95th Edition*; 2014. <https://doi.org/10.1201/b17118>.
- (107) Miller, D. C.; Kempe, M. D.; Muller, M. T.; Gray, M. H.; Araki, K.; Kurtz, S. R. Durability of Polymeric Encapsulation Materials in a PMMA/Glass Concentrator Photovoltaic System. *Prog. Photovoltaics Res. Appl.* **2016**. <https://doi.org/10.1002/pip.2796>.
- (108) Bergman, T. L.; Lavine, A. S.; Incropera, F. P.; DeWitt, D. P. Fundamentals of Heat and Mass Transfer, 2011. *USA John Wiley Sons. ISBN* **2015**.

- (109) Friend, J.; Yeo, L. Fabrication of Microfluidic Devices Using Polydimethylsiloxane. *Biomicrofluidics* **2010**, *4* (2), 1–5. <https://doi.org/10.1063/1.3259624>.
- (110) Lee, H.; Koh, D.; Xu, L.; Row, S.; Andreadis, S. T.; Oh, K. W. A Simple Method for Fabrication of Microstructures Using a PDMS Stamp. *Micromachines* **2016**, *7* (10), 1–9. <https://doi.org/10.3390/mi7100173>.
- (111) Robertson, J.; Riggs, B.; Islam, K.; Ji, Y. V.; Spitler, C. M.; Gupta, N.; Krut, D.; Ermer, J.; Miller, F.; Codd, D.; Escarra, M. Field Testing of a Spectrum-Splitting Transmissive Concentrator Photovoltaic Module. *Renew. Energy* **2019**. <https://doi.org/10.1016/j.renene.2019.02.117>.
- (112) Laskar, M. R.; Nath, D. N.; Ma, L.; Lee, E. W.; Lee, C. H.; Kent, T.; Yang, Z.; Mishra, R.; Roldan, M. A.; Idrobo, J. C.; Pantelides, S. T.; Pennycook, S. J.; Myers, R. C.; Wu, Y.; Rajan, S. P-Type Doping of MoS₂ Thin Films Using Nb. *Appl. Phys. Lett.* **2014**, *104* (9). <https://doi.org/10.1063/1.4867197>.
- (113) Das, S.; Chen, H. Y.; Penumatcha, A. V.; Appenzeller, J. High Performance Multilayer MoS₂ Transistors with Scandium Contacts. *Nano Lett.* **2013**. <https://doi.org/10.1021/nl303583v>.
- (114) Peng, B.; Yu, G.; Liu, X.; Liu, B.; Liang, X.; Bi, L.; Deng, L.; Sum, T. C.; Loh, K. P. Ultrafast Charge Transfer in MoS₂/WSe₂ p-n Heterojunction. *2D Mater.* **2016**. <https://doi.org/10.1088/2053-1583/3/2/025020>.
- (115) Arnold, A. J.; Shi, T.; Jovanovic, I.; Das, S. Extraordinary Radiation Hardness of Atomically Thin MoS₂. *ACS Appl. Mater. Interfaces* **2019**.

<https://doi.org/10.1021/acsami.8b18659>.

- (116) Brar, V. W.; Jang, M. S.; Sherrott, M.; Lopez, J. J.; Atwater, H. A. Highly Confined Tunable Mid-Infrared Plasmonics in Graphene Nanoresonators. *Nano Lett.* **2013**.
<https://doi.org/10.1021/nl400601c>.

Biography

Kazi Islam was born and raised in Khulna, Bangladesh. He went to American International University-Bangladesh (AIUB) in Dhaka, Bangladesh for his undergraduate studies and completed his BSc in Electrical & Electronic Engineering in 2008. He worked as a lecturer in the Faculty of Engineering, American International University-Bangladesh (AIUB) from 2008 til 2011. He then pursued an MSc in Microsystems Engineering from Masdar Institute in Abu Dhabi, UAE, in 2013. Kazi Islam joined Tulane University in 2015 to pursue his doctoral studies in Physics (Materials Track) under the supervision of Prof. Matthew Escarra. His research interests include optoelectronics, nanophotonics, photovoltaics, hybrid solar energy, etc.